Department of Physics and Astronomy
University College London
University of London

LASER INDUCED ULTRAFAST DYNAMICS IN ATOMS AND MOLECULES

Elizabeth M L English

Submitted in partial fulfilment of the requirements
For the degree of Doctor of Philosophy
At the University of London

September 2007

ProQuest LLC
789 East Eisenhower Parkway
P.O. Box 1346
Ann Arbor, MI 48106-1346

I declare that the work contained within this thesis is my own unless stated otherwise

.....

Elizabeth M L English

Abstract

The dynamics of atoms and molecules in an intense femtosecond laser field are studied experimentally using time-of-flight spectroscopy.

10fs laser pulses have been used to resolve ultrafast vibrational and rotational wave packet dynamics in deuterium, using a pump-probe technique. The revival and subsequent dephasing of the wave packet is observed with a view to controlling these processes.

A new non-Gaussian intensity deconvolution technique is presented, which removes beam diffraction effects and defines the ionisation rate as a constant with respect to ellipticity of laser polarisation. As a consequence of this technique, ultrafast shake-up excitation during tunnel ionisation in atoms has been observed for the first time.

The dependence of recollision in an atomic ion on the ellipticity of the laser field has been observed experimentally using laser pulses of 40fs. Through the use of an experimental intensity selective scanning technique, intensity resolved ion yields have been obtained. Following the removal of the laser confocal volume and diffraction effects, the experimental results have been compared with a theoretical model. This quasi-classical model simulates the recollision process in an elliptically polarised laser field.

Acknowledgements

I would like to thank all the people who have made this work possible:

Prof. Roy Newell and Dr Will Bryan, my supervisors, for their invaluable knowledge and patience.

My colleagues past and present, at University College London; Dr Sarah Watson and Joe Wood, and collaborators at Queen's University Belfast; Prof. Ian Williams, Dr B Srigengan, Dr M Suresh, Dr Jarlath McKenna and Chris Calvert. We made a great team, and I wish you all the best for the future.

Everyone at the ASTRA TA1 Laser Facility at the Rutherford Appleton Laboratory; Edmond Turcu for the acquisition of the 10fs system, and Andrew Langley, Edwin Divall, Chris Hooker, Klaus Ertel and Jodie Smith for their technical expertise.

Finally, I would like to thank all my family and friends; especially my mum for being eternally supportive and Jick for always believing in me.

Financial support from the Engineering and Physical Sciences Research Council is gratefully acknowledged.

Contents

List of Figures

List of Tables

Chapter 1

Experimental and Theoretical Review

The dynamics of atoms and molecules in an intense laser field are of considerable interest to numerous branches of physics and chemistry, and have formed the subject of many experimental and theoretical studies. Although the understanding of such quantum systems is of fundamental interest, a future view to controlling ultrafast dynamics in atoms and molecules using a strong laser field also exists. The key aspects of laser-matter interactions relevant to this research are reviewed in this chapter, providing a background for the new experiments which form the body of this thesis.

1.1 Atoms in Intense Laser Fields

Advancements in laser technology from the 1960s to the present day have driven the development of strong field atomic physics. Laser pulses of femtosecond duration can easily produce electric fields of the order of the Coulomb field in a hydrogen atom. which is $5 \times 10^{9}\mathrm{Vcm}^{-1}$, equivalent to the atomic unit of intensity $3.51 \times 10^{16}\mathrm{Wcm}^{-2}$. Such a strong field acts in competition with the Coulomb binding force of an atom to control the atomic electron dynamics through ionisation. Different ionisation regimes, dependent

on the intensity of the laser generated electric field and the photon energy have been established, with their boundaries quantified by Keldysh theory [Keldysh, 1965]. The phenomenon of multiple ionisation where more than one electron is removed, and the subsequent unbound electron dynamics in the laser field, is also of great interest due to applications in high harmonic generation.

1.1.1 Ionisation Mechanisms

At relatively low laser intensities $<10^{13}$ Wcm^{-2} multiple photons can be absorbed simultaneously from the laser field to reach the ionisation potential (I_P) of the atom through multiphoton ionization (MPI) as shown in Figure 1.1a. This theory was first proposed by [Goeppert-Mayer, 1931] as $n\hbar\omega > I_P$, where n is the integer number of photons absorbed. At such intensities, perturbation theory is sufficient to describe the promotion of the bound electron to the continuum by the laser field [Fabre et al., 1982]. Within this theory, the field is described as a small perturbation which does not affect the existing atomic states. The n-photon ionisation rate Γ_n, of MPI can be determined from first order perturbation theory as

$$\Gamma_n = \sigma_n I^n \tag{1.1}$$

where n is the minimum number of photons needed for ionisation, σ_n is the generalised n-photon ionisation cross section, and I is the intensity of the incident light. In principle an n-photon ionisation process can be observed at any order n if a sufficiently high laser intensity is used. This has been experimentally verified up to $n = 22$ for atomic helium in a Nd:YAG laser field [Lompre et al., 1977]. The nature of MPI has been studied mainly through the effects of above threshold ionisation (ATI), which occurs when more photons than the minimum number for ionisation are absorbed [Agostini et al., 1979].

A factor contributing to the breakdown of this I^n dependency is the existence of a saturation intensity I_S [Lompre et al., 1985], above which no further ionisation can occur as all the atoms present have been ionised. Above I_S, there is a change in intensity dependence from the predicted I^n to $I^{3/2}$. This is due to the confocal laser volume, which expands with the increasing laser intensity at a rate of $I^{3/2}$ [Posthumus, 2001] and increases the

amount of ionisation. Although present throughout the entire laser intensity range, this rate becomes the only clear process contributing to ionisation above I_S.

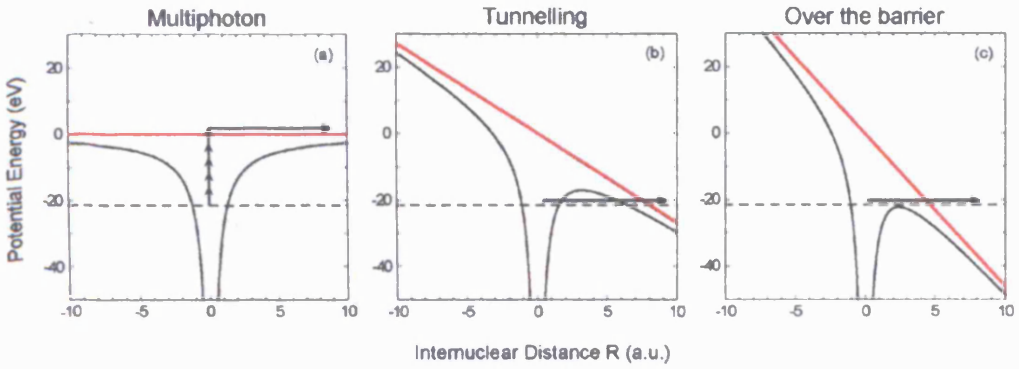

Figure 1.1: Diagrams showing the ionisation mechanisms (arrows) which take place in a strong laser field. The intensity and frequency of the field determines which of these is the dominant mechanism, as described in the text. The dotted line is the field-free binding energy of the electron and the red line shows the action of the laser field on the atomic potential.

At higher intensities, perturbation theory breaks down as the coupling of the field and the atom becomes increasingly important to the system. The atomic potential becomes distorted by the laser induced electric field, so that bound electrons are no longer in a field-free state. This is known as the AC Stark shift, the magnitude of which changes depending on the field oscillation and the temporal pulse envelope. When the electric field is strong, the AC Stark shift can also affect bound electrons causing an upward shift of the energy levels. For strongly bound inner electrons this shift is small due to the small polarisability of these states. However, weakly bound Rydberg levels will experience a large shift in energy of the order of the ponderomotive potential U_P, which is a quiver energy imparted to the electron by the oscillatory motion of the laser field. This can lead to an increase in the ionisation potential of U_P, which can prevent multiphoton ionisation of the low-order channels. Peak suppression of ATI spectra has been observed as a result of this AC Stark shift [Yergeau et al., 1986].

Increasing the laser intensity beyond the multiphoton regime ($\geq 10^{13}$ Wcm^{-2}) leads to an electric field strength comparable to the Coulomb potential of the atom. The laser field distorts the atomic potential sufficiently to create a finite potential barrier through which

the electron can quantum mechanically tunnel out into the continuum (Figure 1.1b). The field distortion follows the oscillatory wave motion of the laser period. Tunnel ionisation occurs within a fraction of an optical cycle of the laser pulse, and so can be treated as a quasi-static process. The probability of an electron tunnelling through the potential barrier increases as the intensity increases, provided that the tunnelling period is less than the laser period i.e. $\tau_{tun} < \tau_{laser}$, which is quantified by the theory of Keldysh [Keldysh, 1965] (Section 1.1.2):

$$\gamma = \frac{\tau_{tun}}{\tau_{laser}} = \frac{\omega(2m_e E_b)^{1/2}}{eE} = \sqrt{\frac{I_P}{2U_P}} \tag{1.2}$$

where ω is the laser frequency, E_b is the electron binding energy, m_e and e are the mass and charge of the electron respectively, and E is the amplitude of the electric field. I_P is the ionisation potential of the atom, and U_P is the ponderomotive potential.

A semi-classical expression for the tunnel ionisation rate (Γ_{ADK}) in an electric field was first proposed by [Perelomov et al., 1966] and generalised by Ammosov, Delone and Krainov, [Ammosov et al., 1986] commonly known as ADK theory:

$$\Gamma_{ADK} = \sqrt{\frac{3E}{\pi(2I_P)^{3/2}}} |C_{n^*l^*}|^2 f(l,m) I_P \left(\frac{2(2I_P^{3/2}}{E}\right)^{((2Z/\sqrt{2I_P})-|m|-1)} \exp\left(-\frac{2(2I_P)^{3/2}}{3E}\right) \tag{1.3}$$

where E is the electric field strength and Z is the residual charge on the ion. Atomic units are used here, where $\hbar = m = e = 1$. The factor $f(l,m)$ where l is the angular momentum and m is the magnetic quantum number can be expanded as:

$$f(l,m) = \frac{(2l+1)(l+|m|)!}{2^{|m|}(|m|)!(l-|m|)!}. \tag{1.4}$$

and the constant $C_{n^*l^*}$ is on the order of 2, but can be calculated by

$$|C_{n^*l^*}|^2 = \frac{2^{2n^*}}{n^*\Gamma(n^*+l^*+1)\Gamma(n^*-l^*)} \tag{1.5}$$

where $n^* = Z(2I_P)^{-1/2}$ is the effective principal quantum number and $l^* = n^* - 1$ is the effective angular momentum quantum number. As debate exists as to the exact origin of

the ADK theory, it will be described as *tunnelling theory* in this thesis.

Various extensions to this tunnelling theory exist, one of which is applied in the studies presented here. The first modification allows for the excitation of remaining bound electrons during tunnel ionisation. While the tunnelling theory above predicts the tunnel ionisation rate of the valence electron with reasonable accuracy, it does not take into account the states of the remaining electrons. It was proposed by Zon that *inelastic tunnelling* can take place, whereby the parent ion is left in an excited state after ionisation. This excitation occurs rapidly through a *shake-up* process first proposed by Carlson [Carlson et al., 1968]. An extension to tunnelling theory has been derived by Kornev and Zon [Kornev et al., 2003] to take into account the process of shake-up during tunnel ionisation and the resulting excitation of the core. This is termed multi-electron tunnel ionisation (METI), the effect of which is to lower the intensity required to ionise subsequent electrons. A comparison between tunnelling theory (dotted lines) which account for single-electron ground state interactions, and the METI results (solid lines) which include multi-electron excitation of all possible states are shown in Figure 1.2. A significant difference between the tunnelling and METI calculations of Ar ion yield is observed, especially for the higher charge states.

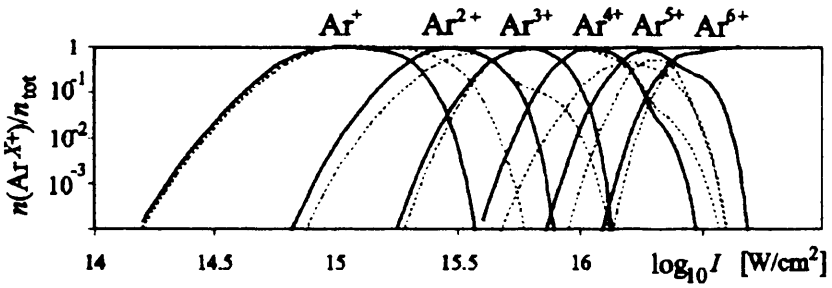

Figure 1.2: Concentration of multiply charged Ar atoms $n(\mathrm{Ar}^{X-})$ up to Ar^{6-} as a function of intensity. n_{tot} is the total number of neutral atoms. Tunnelling theory (dotted lines) is compared with METI calculations (solid lines). A circularly polarised laser field of pulse duration 50fs is used in the calculation. Taken from [Kornev et al., 2003].

The theoretical calculations in Figure 1.2 can be compared to experimental results only after the removal of all laser confocal volume and diffraction effects. Such a non-Gaussian deconvolution technique has been pioneered by our research group [Bryan et al., 2006b]

and used to verify the proposed theory of METI experimentally, presented in Chapter 6. The obtained experimental results confirm that multi-electron tunnel ionisation processes must be considered for an accurate calculation of the tunnel ionisation rate.

As the field strength is increased further, the gradient of the suppressed potential becomes increasingly negative and therefore the barrier becomes narrower and lower. Eventually the potential barrier is equal to the binding energy of the electron, meaning that the ground state can escape directly into the continuum. The field strength exceeds a critical intensity for the atom and the electron is classically free. This is the barrier suppression ionisation (BSI), or field ionisation regime (Figure 1.1c). The electron can now ionise immediately with a probability of unity. The intensity I_{BSI} in Wcm^{-2} at which this regime is entered [Protopapas et al., 1997] is calculated from the ionisation potential I_P in eV, and is given by:

$$I_{BSI} = 4 \times 10^9 \frac{I_P^4}{Z^2}. \tag{1.6}$$

As the laser intensity rises above $\approx 10^{18}\mathrm{Wcm}^{-2}$, relativistic effects must be considered. The electron response becomes highly non-linear as its velocity in the laser field approaches the speed of light [Eberly and Sleeper, 1968]. The effect of the magnetic field generated by the laser becomes important [Keitel and Knight, 1995], as does the relativistic mass shift [Protopapas et al., 1996]. All the laser intensities used for experiments in this thesis are below this limit, so a relativistic treatment is not required.

1.1.2 The Keldysh Parameter

While theories describing multiphoton, tunnel, and barrier suppression ionisation exist, the boundaries between these ionisation regimes are not precisely defined. A universal parameter to quantify these regimes was first proposed by [Keldysh, 1965]. These calculations employ the Volkov wave function [Volkov, 1935], in which the interaction between the electron and the laser field is exactly taken into account while the Coulomb interaction between the ejected electron and the atomic core is neglected. A dimensionless parameter

γ calculated from the ionisation potential I_P and the ponderomotive potential U_P as:

$$\gamma = \sqrt{\frac{I_P}{2U_P}} \tag{1.7}$$

and calculates the ratio of the tunnelling time to the period of an optical cycle as described in the previous section. The ponderomotive potential is the energy of a free electron in the laser field, defined as:

$$U_P = \frac{e^2 E_0^2}{4 m_e \omega^2} \tag{1.8}$$

where e and m_e are the charge and mass of an electron respectively, and E_0 is the amplitude of the laser electric field, oscillating with frequency ω. A more practical form of this equation is used to calculate the ponderomotive potential in eV:

$$U_P = 9.33 \times 10^{-14} I \lambda^2 \tag{1.9}$$

where I is the laser intensity in Wcm^{-2}, and λ is the laser wavelength in μm. For a laser intensity of $3.51 \times 10^{16} \mathrm{Wcm}^{-2}$ (1 a.u.) and wavelength of 0.79μm, $U_P = 2043.8$eV.

As a quantitative guide, Keldysh theory simply defines the dominant ionisation mechanism as quasistatic tunnelling if $\gamma \ll 1$ or MPI if $\gamma \gg 1$. This can be understood from equation 1.7 as follows: The probability of tunnel ionisation depends on the width of the potential barrier, which decreases due to greater barrier suppression as the electric field is increased. This probability is also increased for a low frequency electric field (longer laser wavelength) as the electron has more time to tunnel. Therefore, if the electric field is strong and of a low enough frequency to allow the electron to tunnel free of the atom, tunnelling will be the dominant ionisation mechanism, otherwise MPI will dominate.

As the tunnelling theory described above is only valid in the tunnel ionisation regime, an alternative formula has been proposed [Yudin and Ivanov, 2001] which incorporates γ and can therefore be applied to calculate the ionisation rate across all regimes. Multiphoton and tunnelling regimes can be distinguished from the rates obtained with this theory, which has been successfully demonstrated for atoms [Sheehy et al., 1998].

1.1.3 Multiple Ionisation of Atoms

Double and multiple ionisation of atoms has been the subject of much debate since it was first observed [l'Huillier et al., 1983] to show a strong enhancement of the predicted results at near IR wavelengths. The single ionisation of atoms is well predicted by the single-active-electron (SAE) model [Kulander et al., 1991], where only the outer electron is assumed to interact with the laser field. Extending this model to double ionisation would mean that the electrons are emitted sequentially, i.e. independently. As shown in Figure 1.3(a) this model does not account for the increased double ionisation signal observed in Helium at 780nm at low intensities. The classic knee structure indicates that there is a non-sequential process occurring at this wavelength. In Figure 1.3(b) however, at a shorter wavelength of 248nm there is no indication of such a process. Debate has previously existed as to the precise mechanism producing non-sequential ionisation (NSI). Several processes were proposed, which are discussed below:

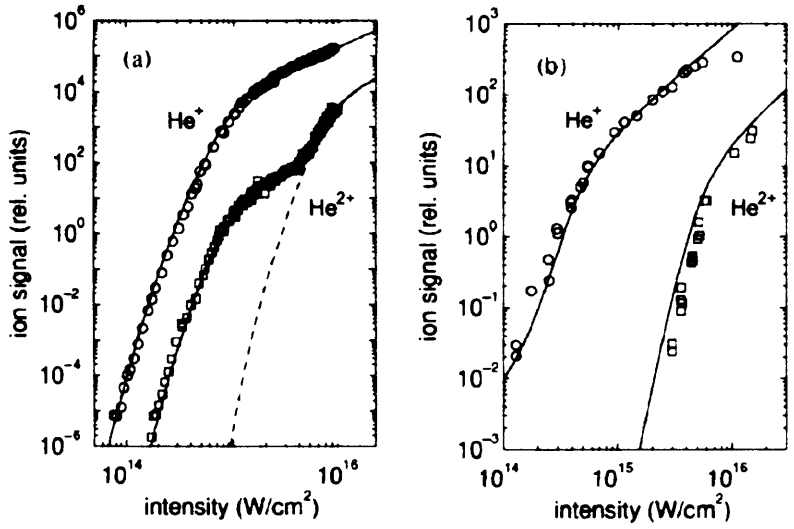

Figure 1.3: Double ionisation yields of helium at 780nm (a) adapted from [Walker et al., 1994] and 248nm (b) adapted from [Charalambidis et al., 1997] using linearly polarised light. An enhancement due to non-sequential ionisation processes is observed in (a) but not in (b).

i) Shake-off One electron is removed so rapidly from an atom or molecule by the electric field that the remaining electrons do not have time to adjust to the non-adiabatic change

in potential. As a result, their wave function projected onto the new eigenstates of the altered potential will have some overlap with the continuum. There is a finite probability of a second electron remaining in this excited state and being ionised immediately by the electric field. The second electron is *shaken off* from the atom due to fast ionisation of the first electron. This process, first proposed by [Fittinghoff et al., 1992], is similar to the mechanism of *shake-up* mentioned previously, where the electrons are excited but not released from the atom.

ii) Recollision The first electron is tunnel ionised, and is then driven back to the atom when the electric field changes sign. On its return, the electron can scatter inelastically causing further ionisation of the atom. The laser field must be linearly polarised for this to occur. Recollision was first proposed by Corkum [Corkum, 1993] and Schafer [Schafer et al., 1993]. This process requires the returning electron to be highly correlated with the core.

iii) Collective Tunnelling Two electrons simultaneously tunnel out from the atom when the potential barrier is suppressed by the electric field, but each interacts independently with the field. First proposed by Eichmann [Eichmann et al., 2000], this is similar to the sequential ionisation of two electrons, but with an extremely short time delay between first and second ionisations.

Recollision has been confirmed as the dominant mechanism producing NSI after experimental investigations into multiple ionisation of atoms using circularly polarised light [Walker et al., 1994]. NSI is commonly observed in experiments using linearly polarised light, but when using a circular polarisation, the NSI contribution was found to be strongly suppressed or entirely absent as can be seen from Figure 1.4. The recollision process is inhibited by circularly polarised light since the rotating electric field vector does not drive the electron back to the parent ion. The effect of polarisation on the recollision process is studied in detail in Chapter 8.

The other mechanisms are considered to be polarisation independent. S-matrix analysis [Becker and Faisal, 2002] has also identified recollision as the dominant mechanism, as its contribution to the total ionisation yield exceeded that from shake-off by many orders of

magnitude. It has also been shown that the rate of collective two-electron tunnelling is far too low to account for the observed NSI yields [Eichmann et al., 2000]. The mechanism of recollision and its consequences are described in the next section.

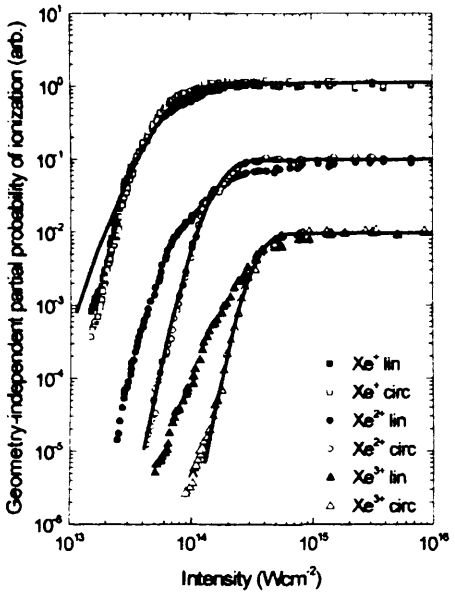

Figure 1.4: Results for the first three charged states of xenon taken using linearly and circularly polarised light are shown. All focal volume effects have been removed, leading to a partial probability of ionisation (explained in detail in Chapter 5) which can be directly compared with theory. Tunnelling theory calculations (thick lines) match the circular data extremely well, as there is no recollision. The classic knee structure is observed in the linear data for charge states Xe^{2+} and Xe^{3+}. Adapted from [Bryan et al., 2006b]

The effects of NSI have been studied using cold target recoil ion momentum spectroscopy (COLTRIMS) [Weber et al., 2000]. This experimental technique (described further in Chapter 3) produces a kinematically complete description of the recollision process, as the momentum of the product ions and electrons can be measured in coincidence. The energy of the recolliding electron can also be determined through measurement of the small ion recoil momentum imparted to the ion upon recollision, again confirming recollision as a dominant mechanism for NSI.

1.1.4 Electron Propagation

Recollision can be described by a quasi-classical model, which occurs in three stages [Corkum, 1993]. The first stage is the quantum mechanical tunnelling of an electron at a particular phase of the electric field, the rate of which can be described by some form of tunnelling theory as discussed in the previous section 1.1.1. The second is the propagation of the liberated electron, driven by the laser electric field. In the third stage, the electron returns to the core to scatter inelastically. It is also possible for the electron to recombine with the atom on recollision, leading to the generation of high harmonics, which will be discussed in the next section.

Initially the electron is tunnel ionised as described previously. The ionised electron is considered to be oscillating freely in the laser induced electric field $E(t) = E_0 cos(\omega t)$, which is linearly polarised. Its velocity $\nu(t)$ can be calculated classically from:

$$\nu(t) = -\frac{eE_0}{m_e\omega}\left[sin(\omega t + \varphi) - sin(\varphi)\right] \tag{1.10}$$

where φ is the phase at which the electron is released. The initial velocity of the electrons directly after tunnel ionisation is called the drift velocity. If only those electrons with a drift velocity of zero are considered as is the case for tunnel ionisation [Corkum et al., 1989], their average kinetic energy defines the ponderomotive energy U_P (equation 1.8). The position of the electrons as a function of time $x(t)$ is determined by integration of equation 1.10:

$$x(t) = \frac{eE_0}{m_e\omega^2}\left[cos(\omega t + \varphi) - cos(\varphi)\right] + sin(\varphi)t. \tag{1.11}$$

This equation is plotted in Figure 1.5, illustrating the time dependent oscillation of the electron in the field for different phases of electron release. Not all electron trajectories return to the origin at $x = 0$, where the electron can cause recollision. The most significant recollision effects are observed from the first return of the electron to the ion, as the electron wave packet spreads as soon as it is free from the atomic potential.

The slope of the trajectory at the $y = 0$ intersection in Figure 1.5 gives the velocity of the electron at its return time, and therefore its kinetic energy. Equation 1.11 can be solved

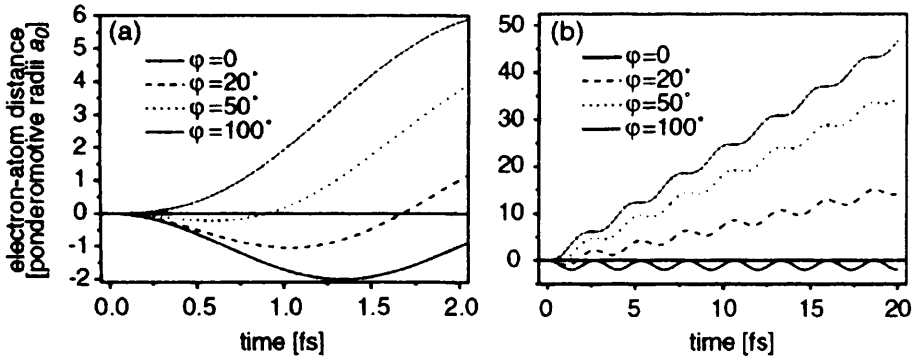

Figure 1.5: Electron trajectories in a laser electric field as a function of phase release. (a) is an enlarged view of (b) for early times. Electrons that ionise at different phases of the AC-field travel different paths. Only some electron trajectories re-encounter the atom, leading to possible recollision. Reproduced from [Pfeifer et al., 2006].

numerically for the return times to calculate the recollision kinetic energy as a function of phase (Figure 1.6). It can be seen from the graph that the maximum recollision energy of $3.17U_P$ occurs when the electron is released at a phase of 18°, close to the peak of the optical pulse cycle.

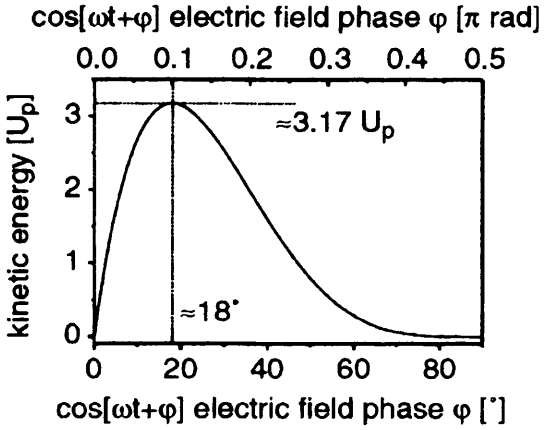

Figure 1.6: Kinetic energy of the electrons at the moment of re-encounter for various phases, φ, of the driving laser field. Maximum recollision energy exists at a phase of 18°. Reproduced from [Pfeifer et al., 2006].

The dependency of the recolliding electron trajectory on the polarisation of the laser field is studied in Chapter 9.

1.1.5 High Harmonic Generation

High harmonic generation (HHG) occurs as the result of a highly nonlinear interaction between the laser field and an atom or molecule, in which the laser light is converted to integer multiples of the fundamental frequency. This effect was first observed experimentally in 1987 [McPherson et al., 1987], but was not fully understood until a quasiclassical theory reproducing these results was put forward by [Corkum, 1993] and [Schafer et al., 1993]. A three-step model is used to describe the process of HHG, similar to the recollision mechanism described previously. *i)* An electron is ionised by the laser electric field close to the peak of an optical cycle, and is driven away from the ion. *ii)* When the electric field changes sign approximately a quarter of a cycle later, the electron is driven back to the ion, having gained a significant amount of energy during its propagation in the field. *iii)* On its return the electron recombines with the ion, transferring this energy plus the ionisation potential into photon energy, giving rise to high harmonics. This process usually occurs every half-cycle of the laser field, leading to peaks at odd integer multiples of the laser frequency.

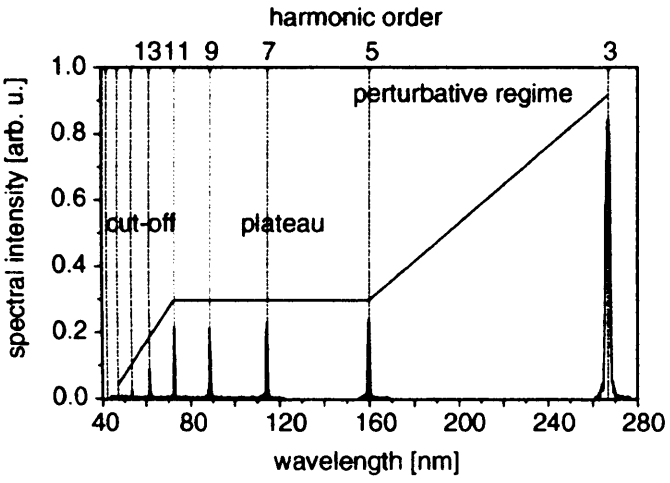

Figure 1.7: A typical spectra of high harmonics, generated in xenon gas showing the characteristic features. For low orders, the harmonic intensity rapidly decreases. A plateau is visible for the higher orders, terminated at the cut-off. The spectral position of the plateau depends on the gas species used and the intensity of the driving laser field. The perturbative regime is described by n-photon excitation, where the excitation probability decreases exponentially with n. Reproduced from [Pfeifer et al., 2006].

It can be seen from Figure 1.6 that there is a maximum kinetic energy that the electron can obtain during its propagation in the electric field, which corresponds to the maximum photon energy that can be generated in the high harmonics. Electrons ionised at a phase of 18° will produce harmonic photons with a maximum energy. The HHG spectrum vanishes or is *cut off* for photon energies above

$$\hbar\omega = 3.17U_P + I_P \tag{1.12}$$

which is observed in experiments. This cut-off law was found empirically [Krause et al., 1992], even before the introduction of the quasiclassical theory. A quantum mechanical description of the three step model has also been developed [Lewenstein et al., 1994].

HHG has been instrumental in the development of the new and exciting field of attosecond science (1as = 10^{-18}s). Each photon emitted during recombination is an ultrashort pulse of x-ray radiation typically hundreds of attoseconds long, with the shortest observed duration being approximately 100as [Mairesse et al., 2003]. The HHG photons have high energies of the order of 10eV to >100eV, a range which extends from the XUV to the soft X-ray region of the electromagnetic spectrum. These short wavelengths have always provided access to the spatial resolution of molecular structure and electron orbitals, but now the temporal resolution of these photons can also be used to observe electron dynamics on their natural timescale.

1.2 Molecules in Laser Fields

Molecules in an intense laser field provide a more complex system to study, due to the additional degrees of vibrational and rotational freedom. By using femtosecond pulses, which are on the time scale of the molecular vibration and rotation, such dynamics can be resolved. This allows the dynamics to be imaged and studied in detail. In the strong field limit at intensities $\geq 10^{11}$Wcm^{-2}, the molecule is described using the *field-dressed states* model.

1.2.1 Dissociation of H_2^+

As the simplest one electron molecule, H_2^+ has been the subject of extensive research. Theoretically, it is the simplest molecule to study and can be modelled accurately by quantum mechanical calculations, although it is difficult to produce experimentally. In the most common experiments, a H_2 target is rapidly photoionised to produce H_2^+:

$$H_2 + n\hbar\omega \rightarrow H_2^+ + e^-. \tag{1.13}$$

After photoionisation, the H_2^+ molecule will either photodissociate (1.14) or ionise further and subsequently undergo Coulomb explosion (1.15):

$$H_2^+ + n\hbar\omega \rightarrow H + H^+ \tag{1.14}$$

$$H_2^+ + n\hbar\omega \rightarrow H^+ + H^+ + e^-. \tag{1.15}$$

It is assumed that fast ionisation of H_2 to H_2^+ occurs on the rising edge of the laser pulse [Tong and Lin, 2004] before the processes of photodissociation or Coulomb explosion take place. Other experiments in our research group create a beam of H_2^+ ions using an ion source (Chapter 4), eliminating the need for the initial ionisation of H_2.

Interactions with H_2^+ (either laser or source generated) are assumed to involve only two states; the ground state $1s\sigma_g$ and the first dissociative state $2p\sigma_u$. Higher lying states can be neglected as they are well separated from the $2p\sigma_u$ state and are assumed not to be populated. Population of the $2p\sigma_u$ state is distributed according to the Franck-Condon principle.

The field free potential energy curves of H_2^+ as a function of internuclear separation are shown in Figure 1.8(a). This shows how the molecule absorbs a number of photons from the laser field, causing excitation to the $2p\sigma_u$ state where it then dissociates. The molecule can absorb more photons than the number required for dissociation (analogous to the ATI process in the atomic case referred to earlier), a process known as above threshold dissociation (ATD) [Bucksbaum et al., 1990]. The extra energy gained from the laser field

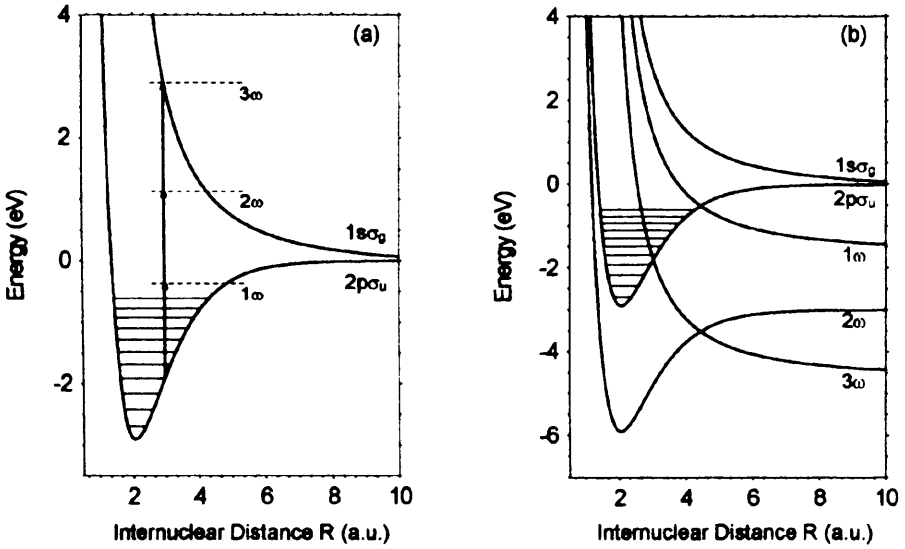

Figure 1.8: (a) Ground state ($1s\sigma_g$) and first dissociative state ($2p\sigma_u$) potential energy curves of H_2^+ showing the absorption of up to 3 photons at 800nm. 1 photon has an energy of 1.6 eV at this wavelength. (b) Ground state ($1s\sigma_g$) and first dissociative state ($2p\sigma_u$) field-dressed diabatic potential energy curves of H_2^+, with dotted lines showing the adiabatic avoided crossings in an intense 10^{16}Wcm^{-2} laser field at 800nm.

by ATD is shared equally between the dissociated fragments of H_2^+.

For weak photon fields. the conventional potential energy diagram shown in Figure 1.8(a) provides a suitable description. However, as the intensity of the field increases the coupling between the $1s\sigma_g$ and $2p\sigma_u$ states becomes very strong due to the induced polarisability of the H_2^+ ion. and a field-dressed potential model [Giusti-Suzor et al., 1990] shown in Figure 1.8(b) provides a more accurate picture of the molecular processes.

The field-dressed potential represents multiphoton absorption by *dressing* the state with a number of photons. As well as shifting the curves by the photon energy, dressing also changes the parity so that the ungerade $2p\sigma_u$ state becomes a gerade state when dressed with the one photon energy. The shift in energy now leads to curve crossings, as shown in Figure 1.8(b). Curve crossing is allowed for states of opposite parity, however if two curves of the same parity cross as in the H_2^+ potential it is forbidden. Theoretical simulation of these avoided crossings is usually achieved using Floquet theory [Chu, 1981].

At intensities $\geq 10^{11}$Wcm^2, the forbidden curve crossings start to adibatically repel one

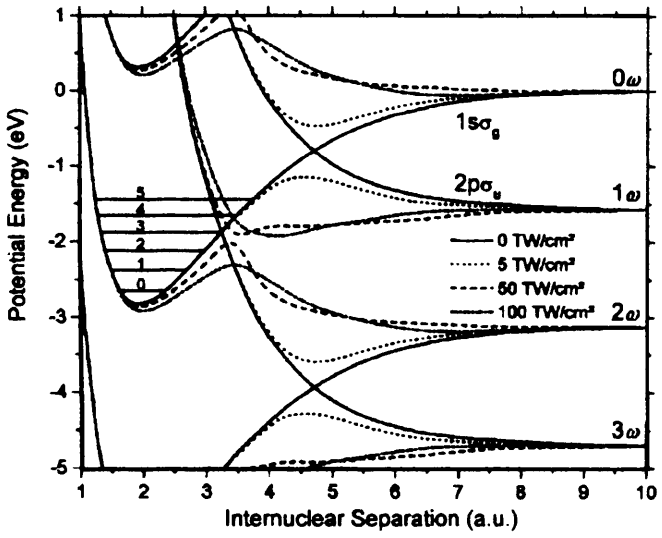

Figure 1.9: Molecular potential energy curves dressed in a photon field of 790nm. As the field is increased, the avoided curve crossings at 4.5 a.u. lead to bond softening. Taken from [Frasinski et al., 1999].

another, as shown in Figure 1.9. A *gap* begins to open, proportional to the laser intensity, leading to complex molecular dynamics which are described below:

i) Bond Softening The opening of a gap at the 1ω avoided crossing allows the nearby vibrational levels (around v=9) to dissociate out onto the $2p\sigma_u$ curve. For higher intensities, the gap is widened and the lower lying vibrational levels may tunnel out through the barrier of the 1ω curve. This effect is called bond softening [Bucksbaum et al., 1990]. As the intensity increases, the opening of the gap increases accessing more of the vibrational levels which can then dissociate via bond softening, as shown in Figure 1.9. The 3ω gap around v=3 also starts to open at intensities $\geq 10^{14}$Wcm^2, providing a 2ω channel. A net 2ω dissociation occurs when initial dissociating wave packet along the 3ω curve adibatically moves onto the 2ω curve (by emission of a photon) at the avoided crossing at 4.5 a.u. (Figure 1.9). The bond softening process is characterised by low energy dissociation fragments from the 1ω and 2ω channels.

ii) Bond Hardening On the rising edge of the laser pulse while the intensity is still low, part of the vibrational wave packet (around v=4) can diabatically move across the avoided crossing gap as shown in Figure 1.10(a). As the wave packet propagates across the 1ω

potential, it decelerates and is reversed. However, the laser pulse has now reached its peak and the field is strong, causing the 3ω gap to widen, which prevents the wave packet from returning to a small R. It becomes trapped in the upper part of the 3ω crossing [Giusti-Suzor and Mies, 1992] as shown in Figure 1.10(b). The lifetime of this light-induced state depends on the laser pulse duration. On the trailing edge of the laser pulse, as the field strength decreases, the adiabatic curve flexes and the wave packet is split. The part of the wave packet at $R \leq 4$a.u. will either fall back into the diabatic $1s\sigma_g$ well, or dissociate along the 2ω channel with a slightly higher energy than the normal 2ω process. The remaining part of the wave packet at higher R will be lifted onto the 1ω curve as the intensity falls, as shown in Figure 1.10(c). The first experimental evidence for bond hardening was obtained [Frasinski et al., 1999] by measuring the kinetic energy of H^+ ions produced from laser interaction with H_2^+. The 1ω dissociation peak was found to shift towards lower energies for increasing pulse durations.

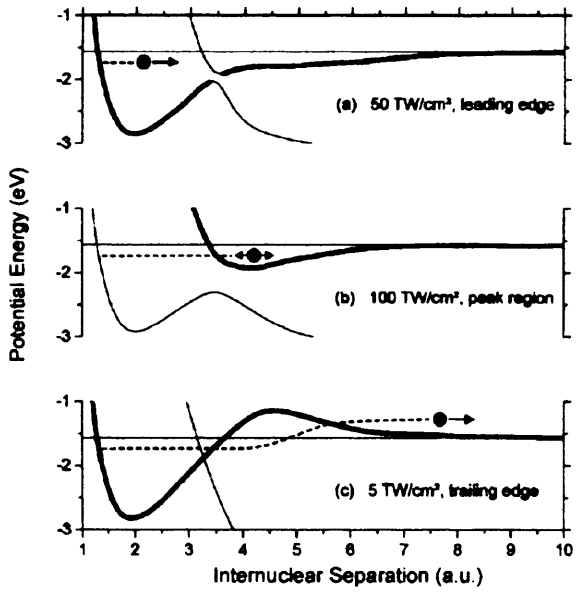

Figure 1.10: The dynamics of bond hardening in H_2^+. (a) The wave packet jumps the gap at the avoided crossing as the laser pulse rises. (b) As the laser intensity increases, the gap is widened and the wave packet is trapped. (c) Laser intensity falls and the well flexes upwards releasing the wave packet. Taken from [Frasinski et al., 1999].

iii) Zero Photon Dissociation The process of trapping described for bond hardening can also occur at the 1ω crossing, where dissociation can occur with no net absorption or emission of photons. This is called zero photon dissociation, and is shown in Figure

1.11. For 800nm light this is unlikely to be observed as it requires population of the higher lying levels - a Franck-Condon distribution places the majority of the population in the lower lying levels with maximum population in the $v = 3, 4$ levels, and a relatively small population in states $v \geq 9$. However, zero photon dissociation has been confirmed at the frequency tripled wavelength of 266nm [Posthumus et al., 2000]. At this smaller wavelength the 1ω crossing can access the levels around $v = 5$, which will have a significant population. In this study, H^+ dissociation fragments with near-zero energy were detected at $\lambda = 266$nm, and to a lesser extent at $\lambda = 400$nm.

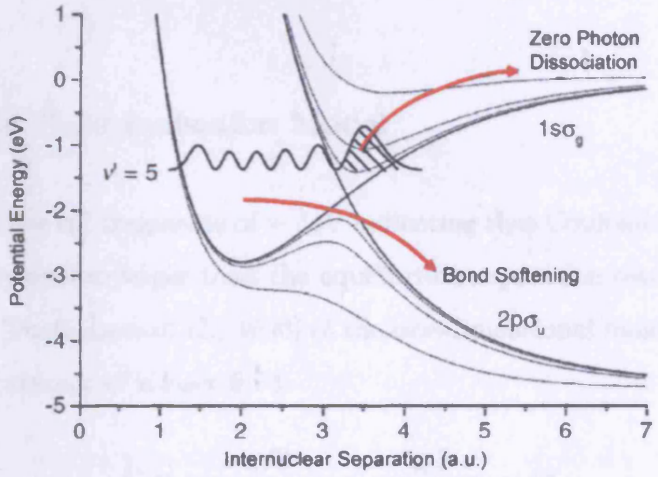

Figure 1.11: The dynamics of zero photon dissociation in H_2^+ at $\lambda = 266$nm. Adapted from [Posthumus et al., 2000].

1.2.2 Coulomb Explosion in Molecules

The removal of electrons from a molecule results in an electrostatic repulsion of the remaining charged fragments, which subsequently Coulomb explode with high kinetic energy. The simplest form of Coulomb explosion occurs in diatomic molecules, and H_2^+ has been the subject of many studies examining this mechanism, along with other diatomics such as N_2 [Frasinski et al., 1987]. The process of Coulomb explosion (CE) for a H_2 molecule can be written as:

$$H_2 + n\hbar\omega \rightarrow H^+ + H^+ + 2e^- \tag{1.16}$$

The kinetic energy release (KER) from this interaction was expected to depend on the equilibrium internuclear separation R which is $\approx$1.4 a.u. for the H_2 molecule, as $KER \propto 1/R$. If assuming no initial kinetic energy, CE would be expected to produce a KER=19eV, so that each ion fragment would be detected with 9.5eV. However, H^+ ions are usually detected with much lower energy than this of around 4eV, which would indicate that CE takes place at the larger R of 6 a.u. [Thompson et al., 1997]. For a 30fs laser pulse, the slow rise time is sufficient to allow for H_2^+ formation [Frasinski et al., 1987], which is then able to dissociate via bond softening to this large R before CE takes place at the peak of the pulse.

1.2.3 Classical Field Ionisation Model

The observed KER of H_2^+ fragments of $\approx$ 4eV indicating that Coulomb explosion occurs at an internuclear separation larger than the equilibrium separation can be explained using a classical model [Posthumus et al., 1996] of the one-dimensional molecular potential (U) distorted by the presence of a laser field:

$$U = -\frac{q/2}{|x + R/2|} - \frac{q/2}{|x - R/2|} - \varepsilon x \tag{1.17}$$

where q is the sum of the atomic charges, R is the internuclear separation, ε is the electric field strength and x is the axial position. The energy level E_L of the corresponding valence electron can be calculated from:

$$E_L = \frac{(-E_1 - q_2/R) + (-E_2 - q_1/R)}{2} \tag{1.18}$$

where E_1 and E_2 are the known ionisation potentials required to produce q_1 and q_2. The molecular potential for I_2^+ is plotted in Figure 1.12.

In this model, Coulomb explosion is assumed to follow a barrier suppression ionisation (BSI) process as described previously for atoms. It can be seen from Figure 1.12 that at 5 a.u. the energy level E_L is well above the central potential barrier, and therefore the valence electron is free to move between the nuclei. An intensity of 5.3×10^{13}Wcm^{-2} is

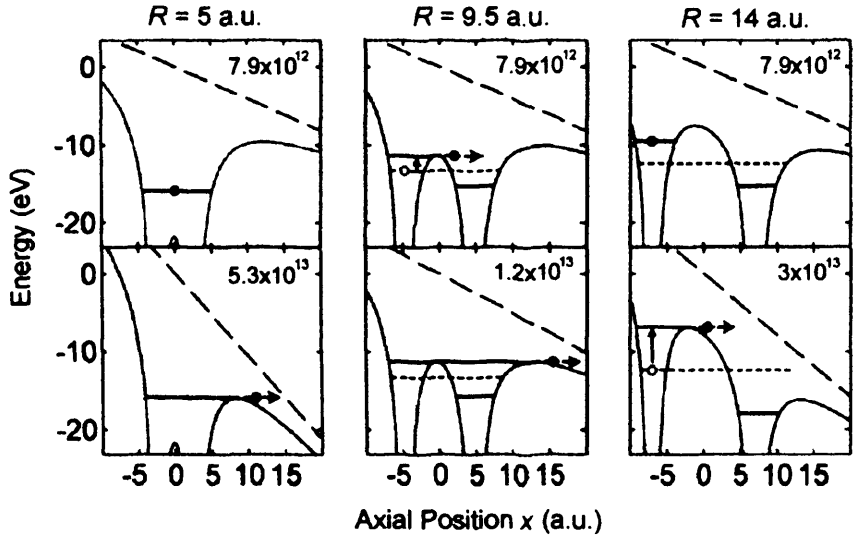

Figure 1.12: Double well potentials for I_2^+ at three different internuclear separations. Numbers in the figure denote laser intensity in Wcm^{-2}. Adapted from [Posthumus et al., 1996]

required to suppress the outer barrier to the electron energy level. As R increases, the electron energy level E_L rises (see equation 1.18), and the electric field becomes more effective at suppressing the outer barrier, lowering the intensity required for ionisation.

At an R of 7.5 a.u. another mechanism becomes apparent, called electron localisation: the central potential barrier rises above E_L and the electron is localised to one of the nuclei. Due to localisation a Stark shift occurs, lifting the energy level on one side of the central barrier and lowering it on the other, which can be seen at $R = 9.5$ a.u. in Figure 1.12. The electron is therefore less bound at intensity $7.9\times10^{12}Wcm^{-2}$ at $R = 9.5$ a.u. than at $R = 5$ a.u., needing only an intensity of $1.2\times10^{13}Wcm^{-2}$ for BSI ionisation.

As R increases further ($R > 10$ a.u.), the central barrier continues to rise above the outer barrier and a higher intensity is required once again for ionisation. It can be seen that there is a critical internuclear distance R_C at which the intensity required for ionisation is at a minimum. This is shown in Figure 1.13, which plots the appearance intensities for all ionisation channels of I_2. It can be seen that R_C is virtually the same for all (q_1, q_2) ionisation channels.

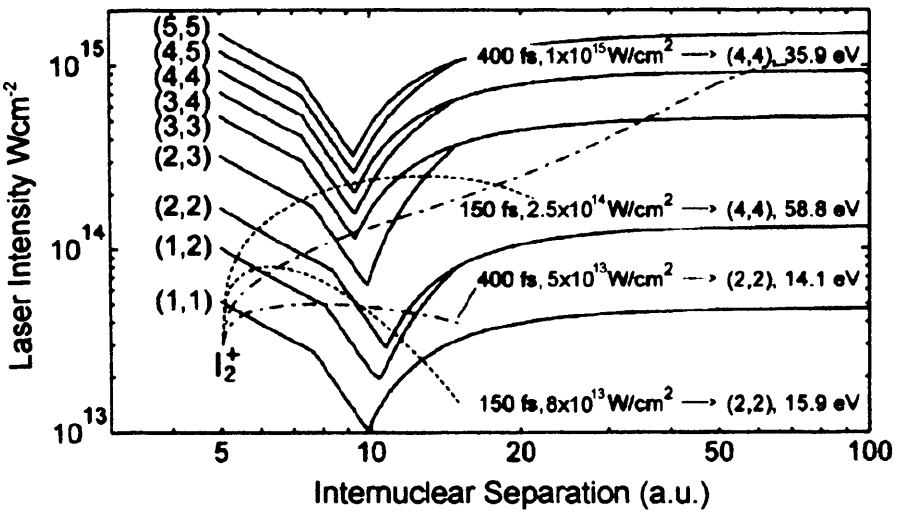

Figure 1.13: Classical appearance intensities of the (q_1, q_2) fragmentation channels if I_2 (full curves) and classical trajectories (dotted curves). All the appearance intensities have a minimum close to 10 a.u. which is the critical internuclear separation. Where the classical trajectory curves cross the appearance intensity curves, the molecular ion becomes ionised to that particular charged state. Adapted from [Posthumus et al., 1996].

1.2.4 Quantum Mechanical Enhanced Ionisation Model

Although the classical model describes the field ionisation processes very successfully, it does not include processes such as quantum mechanical tunneling through the potential barriers. In order to incorporate these effects, a quantum mechanical approach was proposed [Zuo and Bandrauk, 1995], where the 3-dimensional time-dependent Schrödinger equation is solved within the Born-Oppenheimer approximation.

The quantum mechanical model predicts two regions of enhanced ionisation, corresponding to two critical internuclear distances as shown in Figure 1.14. These distances are approximately $R_C = 6$ a.u. and $R_C = 10$ a.u. and are attributed to charge resonance enhanced ionisation (CREI) which results from a process similar to the coupling between the $1s\sigma_g$ and $2p\sigma_u$ states.

At an R of ≈ 4 a.u. the outer barrier is lowered and the electron energy level in one of the molecular potential wells is Stark shifted, so the laser field is sufficient to permit tunnel ionisation. This leads to an increase in the ionisation rate as shown in Figure 1.14.

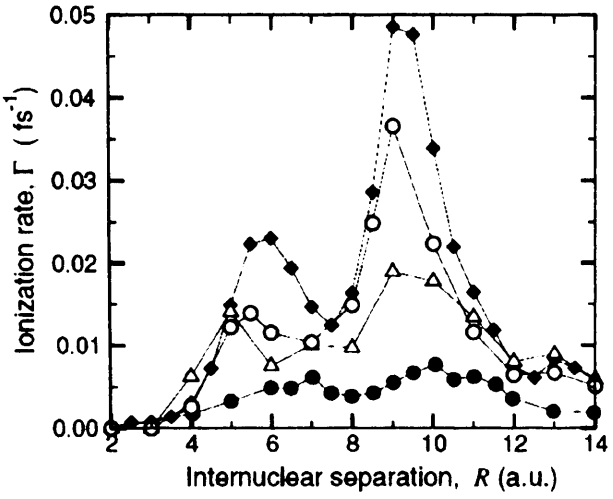

Figure 1.14: Ionisation rate for H_2^+ for dynamic and cycle averaged static fields. The figure shows the wavelength and bond length dependence of the ionisation rate. The maximum field strength has an intensity of $1x10^{14}Wcm^{-2}$. Filled diamonds; time-independent cycle averaged static field rates [Plummer and McCann, 1997]. circles; time-dependent rates for λ = 1064nm from [Peng et al., 2003], time-dependent calculations for λ = 790nm [Peng et al., 2003], filled circles; time-dependent rates for λ = 1064nm from [Zuo and Bandrauk, 1995]. Taken from [Peng et al., 2003].

As R continues to increase, the electron is localised by the rise of the central potential barrier, causing the ionisation rate to fall. The outer barrier is lowered for an R of 8-10 a.u. increasing the ionisation rate again to form the second peak. At $R > 10$ a.u. the central barrier rises again preventing ionisation, so the rate drops.

The second peak in Figure 1.14 is also described by the classical model in section 1.2.3. The first peak occurs as a result of Stark shifting of the energy level prior to electron localisation, which is a quantum mechanical effect and therefore not described by the classical model. CREI peaks have not been conclusively observed experimentally, although ion signal enhancements attributed to CREI have been detected [Ergler et al., 2006c], and CREI has been detected at large R_C [Pavicic et al., 2005] using femtosecond pump-probe experiments.

1.2.5 Molecular Alignment

It has been demonstrated that the ionisation of molecules in an intense laser field is highly dependent on the alignment of the molecular axis with the field polarisation direction. Initial experiments using N_2 [Frasinski et al., 1987] and subsequent investigations using a range of molecules [Thompson et al., 1997],[Schmidt et al., 1994] have all shown a large increase in the ionisation rate when the molecule is aligned with the laser polarisation direction. Two types of molecular alignment have been identified; geometric alignment, which describes the angular dependence of the molecular ionisation rate [Alnaser et al., 2005], and dynamic alignment, which is induced by the laser field polarisation. The latter type of alignment has also been extensively investigated [Rosca-Pruna et al., 2001] and is discussed here in further detail.

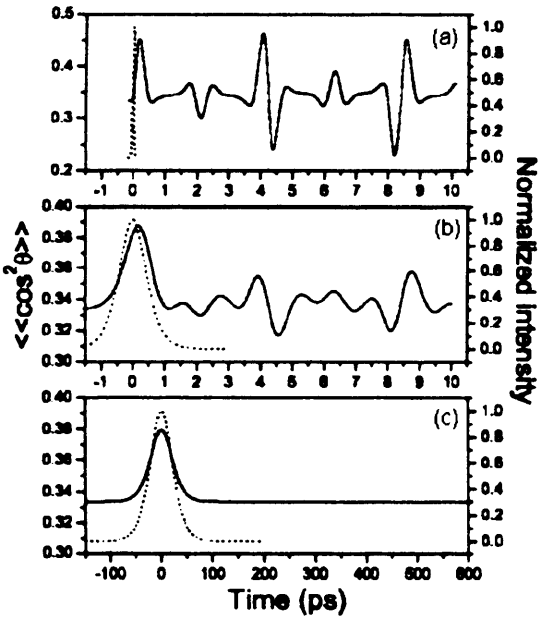

Figure 1.15: Time evolution of the degree of alignment in N_2 (rotation period = 8.3 ps) with different pulse durations (τ) and peak intensities (I_0): (a) Diabatic alignment with τ = 50 fs, I_0 = 2.5x10^{13} Wcm^{-2}; (b) τ = 1 ps, I_0 = 2.5x10^{12} Wcm^{-2}; (c) Adiabatic alignment with τ = 50 ps, I_0 = 2.5x10^{12} Wcm^{-2}. The pulse profiles are represented as dotted curves for reference. Taken from [Torres et al., 2005].

The dynamic spatial alignment of an ensemble of molecules using a linearly polarised laser field can be divided into two different mechanisms, dependent on the laser pulse duration:

i) Adiabatic alignment occurs when a laser pulse much longer than the rotational period of the molecule is used [Friedrich and Herschbach, 1995]. The relatively long laser pulse induces the molecules to adiabatically align their most polarisable axis along the laser polarisation direction. A high degree of laser-molecule alignment can be achieved, but as this is an adiabatic process alignment only exists while the laser field is present (typically picoseconds), after which the molecules return to an isotropic distribution.

ii) Impulsive alignment employs a laser pulse much shorter than the natural rotational period of the molecule to impart angular momentum to the molecules which remain essentially stationary. It is referred to as impulsive alignment as the interaction with the short pulse can be interpreted as an instantaneous kick towards the polarisation direction. This is a nonadiabatic or field-free alignment process, so the molecules will continue to rotate reaching maximum alignment after the laser pulse has gone. Revivals of the maximum alignment are observed periodically at the rotational period of the molecule [Seideman, 1999], as well as $\frac{1}{2}$ and $\frac{1}{4}$ fractional revivals. The impulsive alignment of D_2^+ and its rotational revivals will be studied in Chapter 7.

The transition from the nonadiabatic (impulsive) alignment regime to the adiabatic alignment regime is shown in Figure 1.15. The time-evolution of $\langle \cos^2 \theta \rangle$ was calculated for an ensemble of N_2 molecules at a temperature of 50k, where θ is the angle between the molecular axis and the laser field polarisation direction. Figure 1.15a shows the typical features of impulsive alignment produced using a short laser pulse of 50 fs duration, with a maximum in the alignment immediately after the laser pulse. Half and full revivals of the maximum alignment occur at 4.1 ps and 8.3 ps, along with half height quarter revivals. When a long pulse of 50 ps is used, the alignment is purely adiabatic (Figure 1.15c), so the maximum in alignment is reached at the peak of the laser pulse, returning to an isotropic distribution after the pulse has gone. The intermediate stage is shown in Figure 1.15b using a 1 ps pulse. The maximum alignment occurs during the laser pulse as in the adiabatic regime, but some revival structure is evident after the laser pulse has gone.

Chapter 2

Ultrashort Laser Pulse Techniques

Central to this work is the ability to time and intensity resolve processes on an atomic and molecular timescale. The advancement of short pulse laser technology has lead to the generation of femtosecond (fs) laser pulses, where 1fs = 10^{-15}s. These pulses, of the order of $\approx$ 10fs duration, allow the vibrational and rotational dynamics of a molecule to be observed directly. This chapter will describe the generation and amplification of femtosecond laser pulses, as well as the methods used to measure pulse shape and duration.

The characterisation of femtosecond pulses is challenging as electronic devices are not fast enough to measure pulses on such a rapid timescale. Alternative methods have been devised, most commonly autocorrelation techniques which make use of the pulse itself. A complete characterisation requires knowledge of the spectral phase and amplitude of the pulse.

2.1 Generation of Short Laser Pulses

An important feature of all laser pulses is that the spectral bandwidth $\Delta\nu$ and pulse duration $\Delta\tau$ cannot vary independently of one another. The bandwidth is the range of spectral frequencies that make up the pulse, and depends on the gain medium in the laser cavity. The gain medium Ti:Sapphire has a large gain bandwidth, from 650nm to 1100nm,

and is therefore often used to generate short laser pulses. Maximum gain for this medium occurs around 800nm, which is the typical operating wavelength of a Ti:Sapphire laser, although it is tunable over its entire wavelength range. The minimum full width at half maximum (FWHM) duration-bandwidth product is:

$$\Delta\nu\Delta\tau = c_B \tag{2.1}$$

where c_B is a constant of the order of 1, depending on pulse shape. Values for a Gaussian and a sech^2 pulse shape are 0.441 and 0.351 respectively. This inverse relationship is a consequence of Fourier theory, as the pulse duration is determined from the Fourier transform of all the spectral frequency components. The shortest possible pulse duration obtained from a given frequency spectrum is known as the transform limited pulse duration.

The following sections will discuss pulse generation in the laser oscillator, pulse amplification, and the subsequent compression that takes place to form a 10fs pulse. In order to produce pulses from a laser oscillator, a process such as mode locking must be applied to lock a large number of cavity modes to a particular phase. The pulses produced from the oscillator will be of $\approx$ 10fs duration, but are usually only a few nanojoules (nJ) in energy. They are then amplified using a technique called chirped pulse amplification, which increases the pulse energy to $\approx$ 1 mJ. Further temporal compression of the pulse can only take place if additional bandwidth is created. Several innovative techniques exist to reduce the pulse duration to below 10fs, including hollow fibre compression, a method implemented by the ASTRA laser system used for the experiments in this thesis.

2.1.1 Oscillators

A laser oscillator is made up of the laser medium (Ti:Sapphire crystal), and an arrangement of mirrors to reflect the laser light back and forth through the crystal. This laser medium, consisting of N atoms per unit volume where N_1 and N_2 are the populations of the higher and lower energy states respectively, will amplify the process of stimulated emission essential for lasing. For stimulated emission, atoms occupying a higher energy state can

be forced to return to a lower energy state when stimulated by a pump photon of energy equal to this energy gap. Each of these transitions results in the emission of a photon, all of which will be emitted exactly in phase with each other, producing a coherent light wave.

The population of the lower energy state is normally larger than that of the excited state i.e. $N_2 < N_1$, causing the stimulated emission to die out. However an increase in the stimulated emission, and therefore amplification within the laser medium can be obtained by creating a population inversion so that $N_2 > N_1$. Using the two-level system described here, it is not possible for population inversion to take place. A 3- or 4-level system is required as shown in Figure 2.1. In the 3-level system, the laser transition ends on the ground state. At least half the population of atoms must be excited to the upper laser level to obtain a population inversion, and as a consequence of this the laser medium must be very strongly pumped.

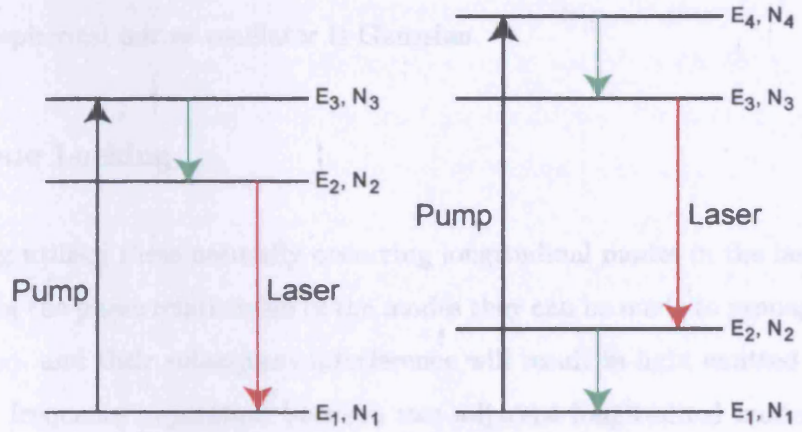

Figure 2.1: A three level laser system (left) where the laser transition (red arrow) ends on the ground state. In the four level system (right), the laser transition ends on a level above the ground state, which is quickly depopulated. Fast non-radiative transitions are indicated by green arrows.

The more efficient type of laser is the 4-level system. As in the 3-level system, the pump transition excites atoms into the upper state, but now there is a fast non-radiative transition to E_3 which has a longer lifetime than the laser transition. This causes the population to accumulate in E_3, creating a population inversion. The laser transition ends on a level above the ground state, which has another fast non-radiative transition to the ground state

so that negligible population exists in E_2. Therefore, only a few atoms must be excited to the upper laser level to form a population inversion. In both cases, the energy of the pump transition is greater than that of the laser transition, requiring optical pumping with light of a higher frequency (shorter wavelength) than the resulting laser light.

Within the laser oscillator the light bounces back and forth, amplified in this way on each pass through the crystal. Constructive and destructive interference of these reflected light waves lead to standing waves in the oscillator, which form a discrete set of frequencies called longitudinal modes. These are the only modes permitted to resonate in the oscillator, given by

$$\frac{m\lambda}{2} = L \tag{2.2}$$

where m is the mode order (a positive integer), L is the optical path length within the oscillator. It can be seen that the distance L must be an integer multiple of the half wavelength of the laser light, $\lambda/2$. The fundamental transverse electromagnetic mode (TEM) of a spherical mirror oscillator is Gaussian.

2.1.2 Mode Locking

Mode locking utilises these naturally occurring longitudinal modes in the laser oscillator. By controlling the phase relationship of the modes they can be made to propagate together (i.e. in phase), and their subsequent interference will result in light emitted as a train of pulses. The frequency separation between two adjacent longitudinal modes Δv can be calculated from

$$\Delta v = \frac{c}{2L} \tag{2.3}$$

and depends on the round trip time T for light in the cavity of length L, as $T = 2L/c$. Each mode oscillates independently, however if the modes can be made to oscillate with a fixed phase between one another they will constructively interfere periodically, producing a pulse of light. This period is equal to the round trip time T, and the frequency is therefore equal to the mode spacing of the laser $\Delta v = 1/T$. The laser can now be described as mode locked.

Methods to produce mode locking can be either active or passive. Active mode locking is achieved by modulation of the light in the laser oscillator through an external signal, usually produced through the use of an acousto-optic modulator. It acts as a fast shutter with a period carefully matched to the round trip time T. Passive mode locking results from an element such as a saturable absorber placed in the laser oscillator to cause self-modulation of the light. Saturable absorbers exhibit intensity dependent transmission and will preferentially transmit high intensity light while absorbing light of low intensity, amplifying the random high intensity spikes which naturally occur in the laser oscillator which produces mode locking after many round trips. These methods can produce pulses of picosecond duration.

Ti:Sapphire lasers make use of intrinsic non-linear optical effects to create self mode locking (SML) [Spence et al., 1991], a passive mode locking technique. A highly successful SML method employs the Kerr optical effect in the Ti:Sapphire crystal, due to the fact that the refractive index of the crystal is intensity dependent. As the laser pulse profile contains an intensity variation, a lensing effect is produced in the crystal whereby the refractive index experienced by the beam is greater in the beam centre than at the beam edge. This is self focusing, which can cause damage to optical elements in extreme cases. The laser oscillator is designed so that the low intensity part of the beam is lossy, but the high intensity part becomes amplified. As a result of the fast response time of SML and the large bandwidth of the Ti:Sapphire crystal, pulses of 10fs duration can be produced, although the energy per pulse is low (a few nJ).

2.1.3 Group Velocity Dispersion

The velocity of light propagating through a material is dependent on the refractive index, n of the material [Agrawal, 2001], and can also be written in terms of frequency ω and wavenumber $k = 2\pi/\lambda$.

$$\nu = \frac{c}{n} = \frac{\omega}{k} \tag{2.4}$$

This equation describes the phase velocity ν at which each spectral component travels through a material. A laser pulse is made up of a number of different frequencies with

each spectral component travelling at a different ν, so a group velocity is required to describe the speed at which the entire pulse propagates.

$$\nu_g = \frac{d\omega}{dk} \tag{2.5}$$

The distortion of the pulse shape as it propagates is given by the variation of the group velocity with frequency.

$$\frac{d^2k}{d\omega^2} = -\frac{1}{\nu_g^2}\frac{d\nu_g}{d\omega} \tag{2.6}$$

The usual definition of group velocity dispersion (GVD) is

$$\frac{d\nu_g}{d\lambda} = \frac{\omega^2\nu_g^2}{2\pi c}\frac{d^2k}{d\omega^2} \tag{2.7}$$

As a result of GVD, the pulse becomes chirped; the different frequencies are rearranged within the pulse leading to broadening of the spectrum. This chirp is usually positive, where the high frequency components (blue) are delayed with respect to the lower frequency components (red). As the pulse propagates, the temporal profile is stretched increasing the pulse duration. Therefore, the spectral structure maps onto the temporal profile but retains its Gaussian shape as a Fourier transform does not alter the shape of a Gaussian pulse. Higher order derivatives can be considered as the refractive index changes nonlinearly with wavelength, which are termed third order dispersion, fourth order dispersion, etc.

Temporal and spectral pulse broadening due to GVD occurs during pulse propagation through air paths, and any dispersive optics in the path will significantly increase GVD. The resulting positive chirp on the pulses can be compensated for by introducing negative chirp via diffraction gratings, dispersive prisms or chirped mirrors. These optics can be used to delay the low frequencies (red) with respect to the high frequencies (blue) so they are overlapped temporally once again, producing a short unchirped pulse. This control of GVD is employed during chirped pulse amplification.

2.1.4 Chirped Pulse Amplification

In order to increase the intensity of the laser pulses from the laser oscillator an amplification stage is introduced. Chirped pulse amplification (CPA) [Strickland and Mourou, 1985] is a technique used to generate high power ultrashort laser pulses. Before the invention of this technique, the maximum obtainable intensity of the pulses was limited by the damage threshold of the optical components within the laser oscillator, usually $\approx 10^9$ Wcm^{-2}. The process of CPA (Figure 2.2) circumvents this limit by first stretching the laser pulse temporally, which proportionally decreases the peak pulse intensity and thus prevents damage caused by non-linear processes such as self-focusing.

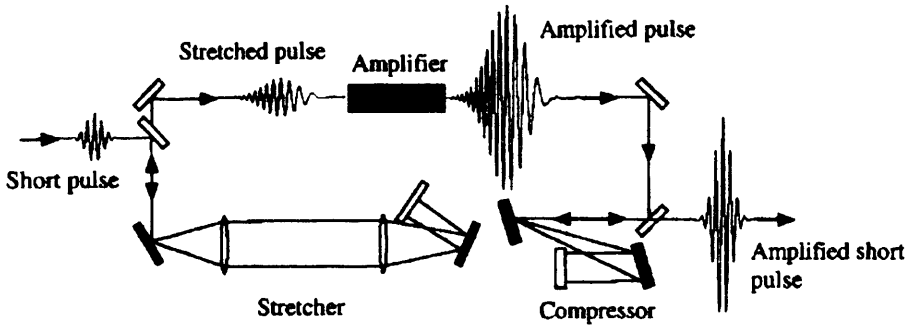

Figure 2.2: Diagram illustrating the process of chirped pulse amplification; A short pulse is stretched by a grating pair, inducing positive chirp. This pulse is then amplified by several orders of magnitude, and recompressed to produce a short pulse of high power. Taken from [Backus et al., 1997].

In the first stage of CPA stretching is performed using dispersive optical elements such as a prism pair or grating pair as in Figure 2.2. A positive chirp is induced whereby the high frequency components (short wavelengths) of the laser pulse are delayed with respect to the low frequency components (long wavelengths) as shown in Figure 2.3 (see Section 2.1.3 for a discussion of dispersion), which increases the duration by a factor of 10^3 to 10^5. The peak intensity of the pulse is therefore reduced proportionally. This pulse can be safely introduced into the amplifier where the pulse is passed through the gain medium a number of times to amplify the pulse by a factor of 10^6 or greater, forming the second stage of CPA.

Two types of amplifier are used for CPA. The regerative amplifier consists of a gain medium

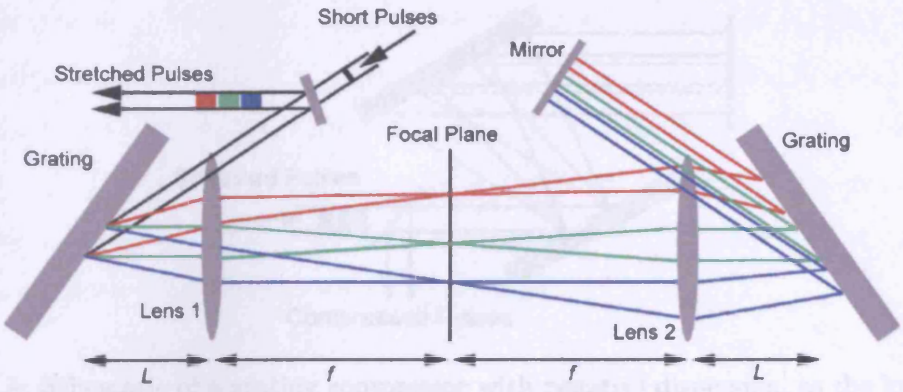

Figure 2.3: Schematic of a grating stretcher configured to produce a positive chirp. As $L < f$ the short wavelengths of the pulse lag behind the long wavelengths.

within an optical cavity together with an acousto-optic modulator (Pockels cell). The number of cavity round trips for the pulse is controlled by the Pockels cell, so this number can be large (≈50) achieving high gain even if the gain per pass is low. The low gain per pass can also be an advantage as it reduces the amount of amplified spontaneous emission generated, which can limit the amount of gain achieved in the laser medium. Regenerative amplifiers output a high quality beam with a good spatial profile. However, it has the disadvantage that the long optical path length may lead to higher order dispersion, which is difficult to compensate for. The other type is a multipass amplifier, where mirrors are arranged so that the input pulse makes several passes through the gain medium before exiting along a new path. Fewer passes means that the gain per pass is high and the dispersion can be easily compensated for.

In the third and final stage, the pulse is recompressed to the shortest possible duration supported by the bandwidth (equation 2.1). This process reverses the initial stretching stage, inducing a negative chirp via a grating compressor as shown in Figure 2.2. In this way, the delayed high frequency components (short wavelengths) of the laser pulse are made to temporally catch up with the low frequency components (long wavelengths) as shown in Figure 2.4, to produce the shortest possible pulse duration from the available bandwidth. Dispersion compensation is also possible at this stage, by altering the spacing of the grating pair.

A disadvantage of using CPA with a gain medium such as Ti:Sapphire is that the gain is

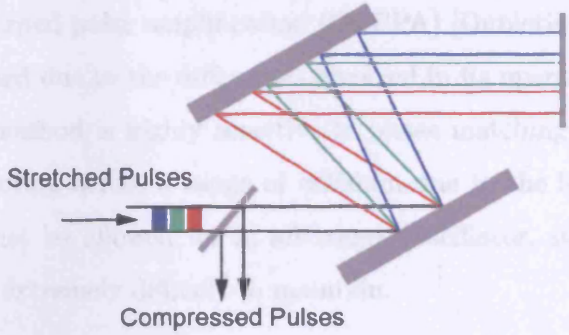

Figure 2.4: Schematic of a grating compressor with negative dispersion, as the long wavelength components of the pulse will travel a greater distance than the short wavelength components. It contains few optical components which can affect high intensity pulses. The amount of dispersion can be tuned by altering the distance between the gratings.

dependent on wavelength. The amplified spectrum will peak around the central wavelength of 800nm, and can become much narrower than the full bandwidth of the gain medium. This is called gain narrowing, which can compress the spectrum leading to an increase in pulse duration. A careful optimisation of the regenerative amplifier is necessary to avoid this effect.

An alternative amplifier which exhibits increased gain bandwidth at high energy is the optical parametric amplifier (OPA) [Galvanauskas et al., 1998]. An intense pump pulse of frequency ω_3 and a weak idler pulse of frequency ω_1 are coincident on a crystal which exhibits a χ^2 non-linearity. If the pulses are phase matched in the crystal, it can produce gain from non-linear sum generation and new signal pulse ω_2 will be created. For energy conservation, $\omega_3 = \omega_1 + \omega_2$.

The main advantage of this technique is that the output can be tuned in wavelength by changing the phase matching conditions. The initial weak signal pulse can be generated by focusing part of the pump beam in a bulk medium to produce a white light continuum, therefore the frequency which is amplified depends on the orientation of the non-linear crystal. By rotating the crystal, the wavelength of the output can be tuned. The OPA crystals also have very large gain bandwidths, so that the full bandwidth of the pulse can be amplified, leading to a shorter compressed pulse duration. OPA can be used with CPA to produce short pulses tunable in wavelength from ultraviolet to infrared. This is called

optical parametric chirped pulse amplification (OPCPA) [Dubietis et al., 1992], although it is not commonly used due to the difficulties involved in its operation at high repetition rates. The OPCPA method is highly sensitive to phase matching conditions within the crystal. Dispersion occurs across a range of ≈250nm due to the large bandwidth of the OPA crystal, and must be allowed for in all stages (oscillator, stretcher, amplifier and compressor) which is extremely difficult to maintain.

2.2 Ultrashort Pulse Compression

The CPA amplified pulses at the ASTRA Laser Facility have a bandwidth of ≈50nm (FWHM), meaning that the transform limited pulse duration is on the order of 20fs (FWHM) from equation 2.1. These pulses can be shortened beyond the initial transform limit by introducing extra bandwidth through spectral broadening, followed by pulse compression. A successful technique employs a noble gas filled hollow-core fibre, the mechanisms behind which are described here.

Transform limited pulses of 25-30fs duration produced from a Ti:Sapphire CPA laser system such as that described in Section 2.1 are coupled into the core of a hollow fused silica fibre filled with noble gas, which acts as a waveguide. As the pulse propagates through the gas, the high intensity creates a non-linear polarisation response so that the index of refraction of the gas changes with intensity. This is the optical Kerr effect, and means that the refractive index experienced by the pulse depends on its intensity profile. A direct result of this effect is self-phase modulation of the laser pulses, broadening the bandwidth of the spectrum. This is described in Section 2.2.1. Propagation of short pulses in any medium including air leads to dispersion (Section 2.1.3), which will increase the pulse duration and must be compensated for. As the pulse spectrum is now much broader (250nm), the pulses can be recompressed to ≈5fs using a series of chirped mirrors, as described in Section 2.2.2.

This technique for ultrashort pulse generation also allows control over the amount of spectral broadening, and therefore pulse duration, by changing the pressure of noble gas inside

the fibre (Chapter 3). This tunability, together with the relatively simple experimental set-up gives the hollow fibre technique an advantage over other methods currently in development such as filamentation.

2.2.1 Self-Phase Modulation

Self-phase modulation (SPM) [Stolen and Lin, 1978] is a nonlinear effect arising from the dependence of the index of refraction on the temporal intensity profile of the laser pulse. This is the mechanism responsible for spectral broadening when using a hollow gas-filled fibre. The lowest order of this dependency is described by the optical Kerr effect [Agrawal, 2001]

$$n = n_0 + n_2 I \tag{2.8}$$

where n_2 is the nonlinear index coefficient of the gas and I is the field intensity. As the intensity of the pulse changes with time, different parts of the pulse experience different magnitudes of refractive index. This affects the temporal phase of the pulse, giving rise to an intensity-dependent phase shift:

$$\Delta\phi(t) = \frac{2\pi n_2 I(t) L}{\lambda} \tag{2.9}$$

where L is the length of the medium, in this case the hollow fibre. This alteration to the temporal phase while the temporal shape remains unchanged results in spectral broadening in the following way; it has the effect of lowering the frequency of the pulse at the leading edge, and increasing the frequency at the trailing edge. Essentially, the medium is becoming optically longer as the pulse intensity rises on the leading edge, so the arrival of optical cycles is delayed. Conversely, the arrival of optical cycles is speeded up on the trailing edge.

If the pulse has a smooth time envelope, it will acquire a linear frequency chirp. $\Delta\omega(t)$, across the central region as shown in Figure 2.5a. The approximate frequency shift at a

time (t) is given by the derivative of the phase perturbation

$$\Delta\omega(t) = -\frac{d(\Delta\phi)}{dt} \tag{2.10}$$

which is proportional to the power. It can be seen from Figure 2.5a that most frequencies occur twice during the laser pulse. This causes interference, either constructive or destructive depending on the relative phase, which gives rise to the distinctive peaked structure of the broadened spectrum seen in Figure 2.5b.

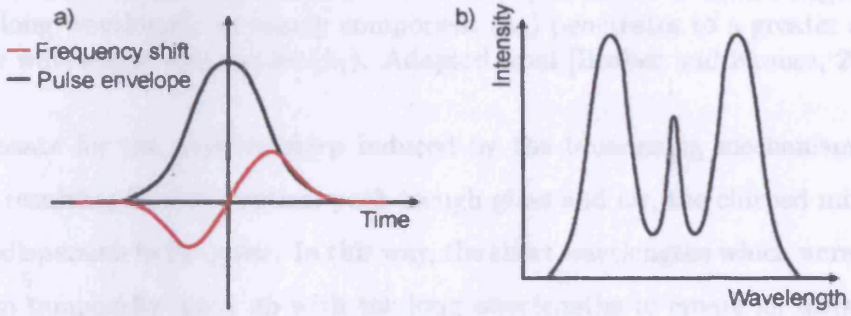

Figure 2.5: a) The laser pulse experiences a frequency shift as a function of time as a result of self-phase modulation, which is approximately linear across the centre of the pulse. b) A typical SPM broadened spectrum.

In this way, the bandwidth of the laser pulses can be increased from a FWHM of approximately 50nm to a FWHM in excess of 250nm. In theory, SPM produces broadening without any change to the temporal profile of the laser pulse. However, dispersion effects will act on the pulse as it propagates, increasing the pulse duration as described in Section 2.1.3.

2.2.2 Pulse Compression using Chirped Mirrors

Now that additional bandwidth has been introduced to the pulses, they can be compressed temporally to their minimum transform limited duration, which can be as short as 5fs. A series of chirped mirrors can be used to perform the compression. These mirrors are coated with a broadband dielectric multilayer coating, the thickness of which varies within the structure so that the Bragg wavelength is not constant. This variation allows the different wavelengths that make up the pulse to penetrate to different depths within the mirror, so

that each wavelength experiences a different group delay as shown in Figure 2.6.

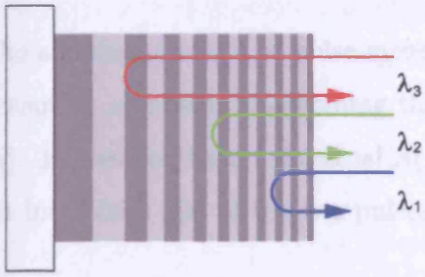

Figure 2.6: Schematic showing the structure of a chirped mirror to induce negative dispersion. The long wavelength frequency component (λ_3) penetrates to a greater depth than the shorter wavelength component (λ_1). Adapted from [Brabec and Krausz, 2000].

To compensate for the positive chirp induced by the broadening mechanism SPM and dispersion resulting from the optical path trough glass and air, the chirped mirrors apply a negative dispersion to the pulse. In this way, the short wavelengths which were previously delayed can temporally catch up with the long wavelengths to create an ultrashort laser pulse. The number of chirped mirrors in the compressor controls the amount of negative dispersion produced; extra mirrors can be added to compensate for additional positive dispersion created from elements such as transmissive optics in the beam or long air paths. The hollow fibre and chirped mirror system used for the present experiments at the ASTRA Laser Facility (Rutherford Appleton Laboratory) is described in detail in Chapter 3.

2.3 Ultrafast Optical Diagnostics

Temporal characterisation of femtosecond laser pulses is an important but difficult requirement in the study of ultrafast phenomena. Innovative methods have been developed for pulse duration measurements, as these pulses are orders of magnitude shorter than the response time of the fastest available optical detectors. This section provides details of the most common optical diagnostics, all of which have been used during ASTRA experiments.

2.3.1 Autocorrelation

Intensity autocorrelation is the simplest method of pulse measurement. It requires splitting the laser pulse to be measured, and then recombining the two identical pulses in a nonlinear crystal (Figure 2.7a). The second harmonic signal $A(\tau)$ generated by the crystal is proportional to the product intensities $I(t)$ of the two pulses,

$$A(\tau) = \int_{-\infty}^{\infty} dt I(t) I(t-\tau) \tag{2.11}$$

where τ is a relative time delay introduced into one beam path. By assuming a sech^2 pulse shape, the autocorrelation function can be deconvoluted to give a full width at half maximum (FWHM) pulse duration measurement.

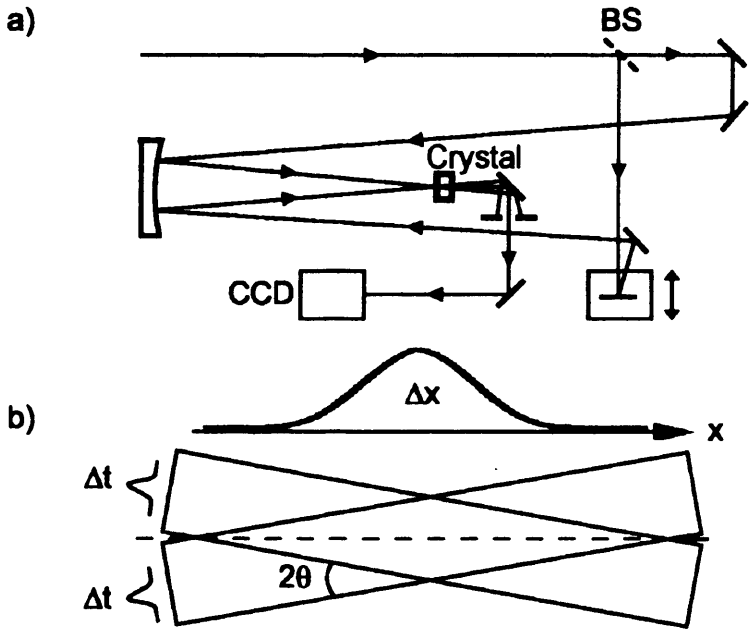

Figure 2.7: a) Schematic of the second order autocorrelator used in Astra TA1; BS, beamsplitter. b) Diagram (showing inside the Crystal) of the second harmonic signal produced along the bisector of the overlap region (dotted line) along the axis of the BBO crystal. The small angle required for second order autocorrelation is shown (2θ).

A second order autocorrelation can be used for ultrashort pulses, as their small spatial extent (30μm for a 100fs pulse) enables single shot measurement. This method is used regularly to measure the pulse duration at ASTRA. The pulses are split as described

above, and then recombined so that they cross at a small angle θ inside the 20μm thick BBO crystal (Figure 2.7b) with respect to the axis of the crystal. A spatial and temporal overlap of the two pulses in the crystal can be achieved provided the beam waist of the overlap region is larger than the spatial pulse length. At every point of overlap, the second harmonic signal is proportional to the product of the local intensity in each beam.

Second harmonic signal is produced along the bisector of the overlap region, and will correspond to the pulse overlap for different time intervals. The central line corresponds to a full temporal overlap of the pulses. The autocorrelation function therefore becomes a spatial intensity distribution of second harmonic signal along the x direction, recorded with a CCD camera. FWHM (Δx) of this distribution is related to the laser pulse duration t_p by

$$t_p = (k\Delta x sin\theta)/c \tag{2.12}$$

where θ is the half angle between the two beams, and k is a constant relating to the pulse shape. For a Gaussian pulse $k = \sqrt{2}$, and for a sech^2 pulse, which is the shape used for the Astra laser pulses $k = 1.3$. An autocorrelation measurement of the 1kHz Astra laser system is shown in Figure 2.8.

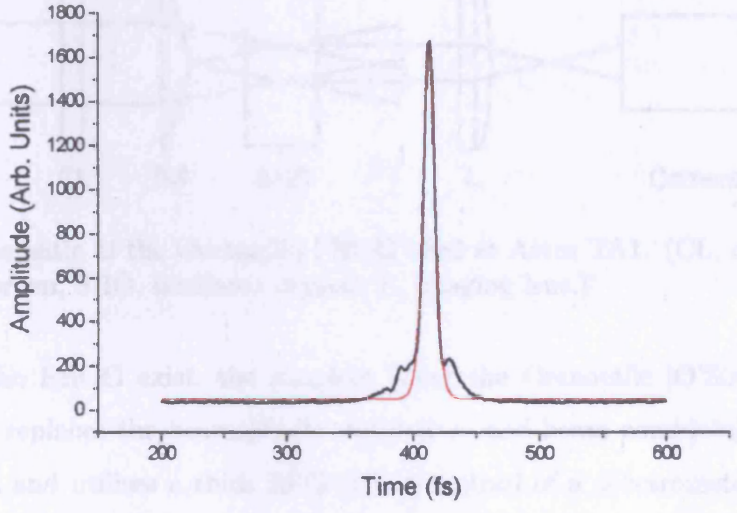

Figure 2.8: An autocorrelation measurement of the Astra 1kHz laser pulses (black curve), showing 11fs FWHM. A sech^2 fit (red curve) is in good agreement with the pulse shape.

Although autocorrelation techniques are widely used, they provide limited information

about the actual shape of the pulse. The intensity distribution is assumed to follow a Gaussian or sech^2 shape, but cannot be directly measured from the autocorrelation. No spectral information is obtained as the result is based purely on intensity measurements.

2.3.2 FROG

Frequency resolved optical gating (FROG) [Trebino and Kane, 1993] is an advancement of autocorrelation measurement, as it combines this technique with a spectrometer to produce a spectrally resolved intensity autocorrelation. The detected signal $S(\omega, \tau)$ is given by:

$$S(\omega, \tau) = \left| \int_{-\infty}^{\infty} E(t) g(t - \tau) \exp(i\omega t) dt \right|^2 \tag{2.13}$$

where $g(t-\tau)$ is a gate pulse, usually a replica of the pulse to be measured, with a variable delay τ. The time delay is scanned across the overlap of the pulses, and the spectrum is measured at each time step. The recorded spectrogram $S(\omega, \tau)$ contains spectral and temporal information, from which full intensity and information about the pulse shape can be retrieved.

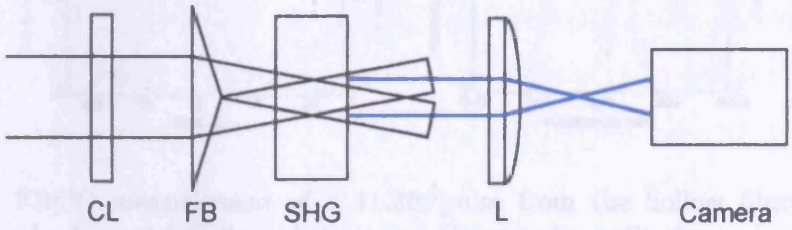

Figure 2.9: Schematic of the Grenouille FROG used at Astra TA1. (CL, cylindrical lens; FB, Fresnel biprism; SHG, nonlinear crystal; L, imaging lens.)

Variations of the FROG exist, the simplest being the Grenouille [O'Shea et al., 2001]. This technique replaces the beamsplitter, delay line, and beam combining optics with a Fresnel biprism and utilises a thick SHG crystal instead of a spectrometer (Figure 2.9). A commercial Grenouille device from Swamp Optics is used at Astra TA1 to measure the pulse duration of the 1kHz laser. Frog traces obtained from the hollow fibre compressor system before its installation in TA1 are shown in Figure 2.10.

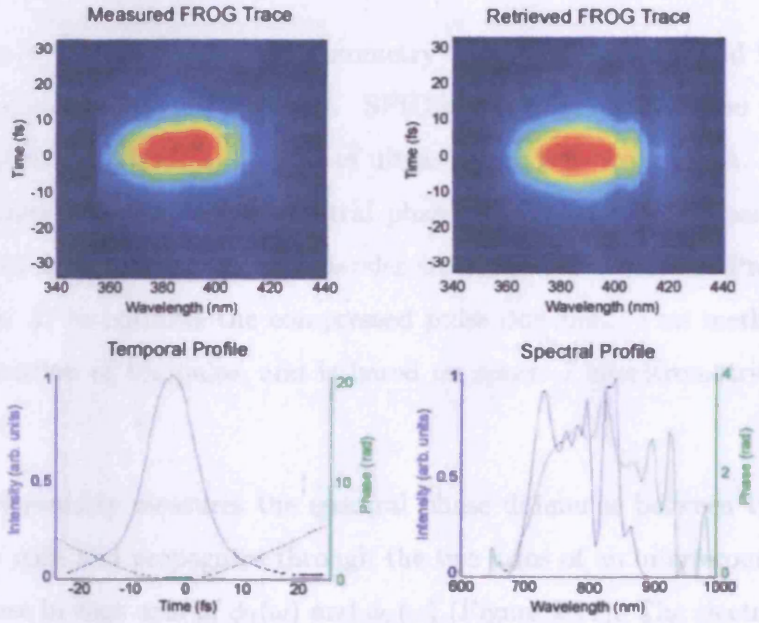

Figure 2.10: FROG measurement of a 11.3fs pulse from the hollow fibre compressor, performed by the Imperial College Attosecond Group who built the system. Argon gas pressure was 0.5 bar. Pulse intensity and phase can be estimated by looking at the measured FROG trace, or the iterative algorithm can be applied to retrieve the precise intensity to produce phase vs. time and wavelength.

A limitation of the FROG technique arises from the large bandwidth associated with pulses in the sub-10fs regime: the nonlinear crystal may not convert all spectral components of the pulse with the same efficiency if it is phase matched to the central frequency. This results in distortions of the signal spectrum, with increased noise in the spectral wings for pulses below 10fs.

2.3.3 SPIDER

An alternative is Spectral Phase Interferometry for Direct Electric field Reconstruction (SPIDER) [Iaconis and Walmsley, 1998]. SPIDER is an interferometric technique that measures both the amplitude and phase of ultrashort pulses. At ASTRA, a SPIDER was built from scratch to measure the spectral phase of the 30fs 1 kHz laser pulse system. Phase information is sent back to the Dazzler situated at the CompactPro amplification stage (Chapter 3) to optimise the compressed pulse duration. This method produces a full characterisation of the pulse, and is based on spectral interferometry which will be described first.

Spectral interferometry measures the spectral phase difference between two fields. The input beam is split and propagates through the two arms of an interferometer, acquiring a spectral phase in each arm of $\phi_1(\omega)$ and $\phi_2(\omega)$ (Figure 2.11). The electric field of each pulse is given by:

$$\widetilde{E}_1(\omega) = \left|\widetilde{E}_1(\omega)\right| e^{i\phi_1(\omega)} \tag{2.14}$$

$$\widetilde{E}_2(\omega) = \left|\widetilde{E}_2(\omega)\right| e^{i\phi_2(\omega)} \tag{2.15}$$

The detected signal is a coherent superposition of the two electric fields

$$I(\omega) \propto \left|\widetilde{E}_1(\omega) + \widetilde{E}_2(\omega)\right|^2 \tag{2.16}$$

$$I(\omega) = |E_1(\omega)|^2 + |E_2(\omega)|^2 + 2\,|E_1(\omega)E_2(\omega)|\cos(\Delta\phi) \tag{2.17}$$

where $\Delta\phi = \phi_1 - \phi_2$. The relative phase difference appears in the interference term, and can therefore be extracted from the resulting interferogram if the phase in one arm

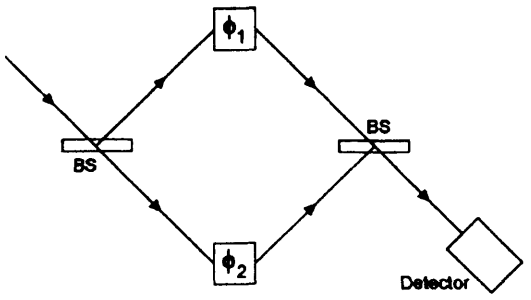

Figure 2.11: Schematic of a spectral interferometer, showing how the beam is split and recombined after acquiring a spectral phase in each arm. The resulting interferogram is recorded on a detector.

is known. The most robust method of phase extraction is based on Fourier analysis [Takeda et al., 1982]. In order to implement this method a linear phase term must be added, which is introduced by increasing the length of one arm of the interferometer with respect to the other. This results in a relative time delay τ and therefore an extra phase term $\omega\tau$, in the interferogram:

$$I(\omega) = |E_1(\omega)|^2 + |E_2(\omega)|^2 + 2\,|E_1(\omega)E_2(\omega)|\cos(\Delta\phi + \omega\tau). \tag{2.18}$$

By Fourier transformation of this interferogram, the spectral phase difference $\Delta\phi$ between the two pulses can be measured.

To measure the spectral phase of a single pulse, SPIDER creates two replicas of this pulse and generates a spectral shear between their carrier frequencies. The pair of pulse replicas are separated in time by a fixed delay τ, and then mixed with a chirped pulse in a nonlinear medium. The spectral phase of the input pulse can be reconstructed from the resulting interferogram.

SPIDER at Astra uses the 4% reflections from the front and back surfaces of a 250μm thick silica etalon to create the two pulse replicas, which have a time delay equal to the etalon round-trip time (Figure 2.12). An interferometer can also be used, allowing variation of the pulse separation. The remaining part of the pulse is transmitted through the etalon and stretched by a 1500 lines/mm grating pair to produce a chirped pulse of approximately 300fs duration. Chirp should be strong enough for each frequency to occur

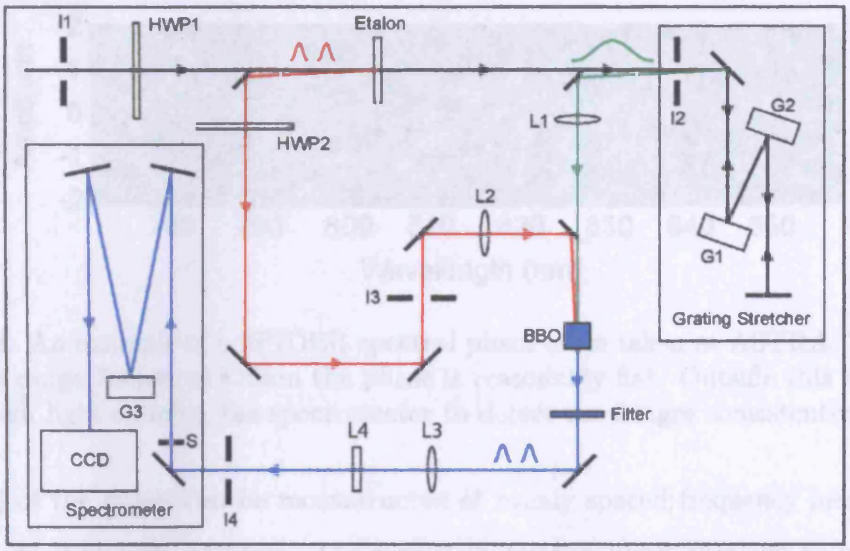

Figure 2.12: Schematic of the SPIDER built for Astra TA1; the paths of the short pulse replicas (red), the stretched chirped pulse (green) and the subsequent upconverted pulse replicas (blue) are shown. I1-4, Irises; HWP1-2, half-waveplates; L1-3, focusing lenses; L4, cylindrical lens; G1-3, gratings; S, slit.

at a different time, such that there is no change in frequency over the duration of the short pulse replicas.

Upconversion of the replicas and the stretched pulse takes place in a 50 μm thick BBO type II crystal. The two beam paths must be equal, and the polarisation of the pulse replicas has been rotated by 90° to ensure type II phase matching in the crystal. As the replicas are separated by a time delay τ due to the thickness of the etalon, each one is mixed with a different temporal and therefore spectral component of the stretched pulse introducing a spectral shear Ω. The pulses are sent to a Czerny-Turner spectrometer [Reader, 1969] where their interference signal is detected.

The resulting spectral interferogram $I_{SPIDER}(\omega)$ can be written as

$$I_{SPIDER}(\omega) = |E_1(\omega)|^2 + |E_2(\omega+\Omega)|^2 + 2\,|E_1(\omega)E_2(\omega+\Omega)| \times \cos(\phi(\omega+\Omega) - \phi(\omega) + \omega\tau). \tag{2.19}$$

It appears as a spectrum modulated by a set of sinusoidal fringes. Spectral interferometry is used to define the linear phase term $\omega\tau$ before making the SPIDER measurement. Total

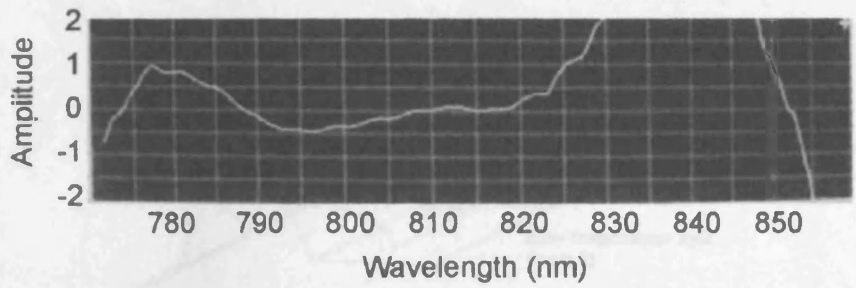

Figure 2.13: An example of a SPIDER spectral phase trace taken at ASTRA. Within the wavelength range 780nm to 825nm the phase is reasonably flat. Outside this range there is not enough light entering the spectrometer to detect the fringes consistently.

phase $\phi(\omega)$ of the pulses can be reconstructed at evenly spaced frequency intervals from $\phi(\omega+\Omega)-\phi(\omega)$ by concatenation. The maximum relative phase that can be measured is limited by the spectrometer resolution, although the theoretical limit set by the Nyquist sampling theorem states that the interferogram must be sampled at least twice per fringe. For the final step, a Fourier transform of the spectral phase shown in Figure 2.13 and an independent spectrum measurement yields the temporal pulse shape. The SPIDER at Astra uses code supplied by Professor Walmsley's group at Oxford University.

SPIDER measures the relative phases of the different spectral components of the pulse (Figure 2.13), which is important for implementing the Dazzler as described in the next section. Installation of this phase measurement system has been beneficial, as previous pulse duration of the 10Hz laser pulses was $\approx$70fs and is now $\leq$40fs.

2.3.4 Dazzler

The Dazzler, a commercial device from Fastlight, is an Acousto-optic Programmable Dispersive Filter (AOPDF). It is designed to pre-compensate for spectral phase errors arising from material dispersion and the B-integral as the beam propagates through the laser system. Phase information obtained from the SPIDER is fed back to the Dazzler, which then ensures that the spectral components of the pulse are all in phase at the laser output. This results in the shortest achievable compressed pulse with the lowest levels of uncompressed background.

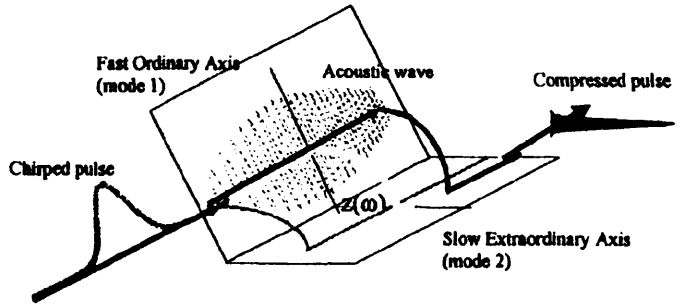

Figure 2.14: Schematic of AOPDF. Optical modes 1 and 2 can be coupled efficiently when there is phase matching. Figure reproduced from [Verluise et al., 2000].

The AOPDF was first proposed by [Tournois, 1997], and demonstrated experimentally by [Verluise et al.. 2000]. The underlying concept of this device is an acousto-optic diffraction of the laser pulse (Figure 2.14). The chirped laser pulse propagates along the fast ordinary axis (mode 1) of a birefringent uniaxial crystal, where it encounters a co-propagating radio frequency controlled acousto-optic wave. Diffraction of the laser pulse occurs as each of its frequency components encounter a phase matched spatial frequency in the acoustic wave, and part of its energy is transfered into the slow extraordinary axis (mode 2). If the velocities of the two modes are different, each frequency component will see a different time delay. Dispersion and amplitude of the pulse can therefore be controlled by the acoustic power at $z(\omega)$ in Figure 2.14. In this way, the Dazzler pre-compensates for the gain narrowing which will occur in the amplifier, and corrects for dispersion induced phase errors.

Chapter 3

Astra Femtosecond Laser

All the present experimental work took place in Target Area 1 (TA1) of the Astra Laser Facility at the Rutherford Appleton Laboratory. The Ti:Sapphire system employs chirped pulse amplification (CPA) technology to produce two pulsed femtosecond laser beams; one at 1 kHz repetition rate, the other at 10Hz.

3.1 1 kHz Laser System

This laser system comprises a commercial Ti:Sapphire oscillator and amplifier (Femtopower Compact Pro, FemtoLasers GmbH) with a prism compressor, resulting in laser pulses at 1 kHz with 30fs temporal duration and 30nm spectral bandwidth. In the next stage, spectral broadening of these pulses is described using a hollow-core fibre which increases the bandwidth to 100nm. Temporal compression is achieved via a set of multilayer chirped mirrors, finally producing pulses of $\approx$10fs duration, measured using the diagnostic techniques described in Chapter 2.

3.1.1 Ti:Sapphire Oscillator and Amplifier

Pulses of 12fs duration and a few nJ in energy are generated in the oscillator at a repetition rate of 75 MHz. The commercial Ti:Sapphire oscillator is pumped by a 532nm frequency-doubled diode-pumped Nd:YVO_4 laser (Millenia, Spectra Physics Inc.) as shown in Figure 3.1. Peak wavelength of the pulses is 800nm and the bandwidth is 80nm. For the first stage of CPA, these oscillator pulses are dispersively stretched to a duration of 20ps in a 10cm long SF57 glass block and pass through an acousto-optic programmable dispersive filter (Dazzler, Fastlite), before being sent to a multipass Ti:S amplifier (Femtopower Compact Pro, FemtoLasers GmbH).

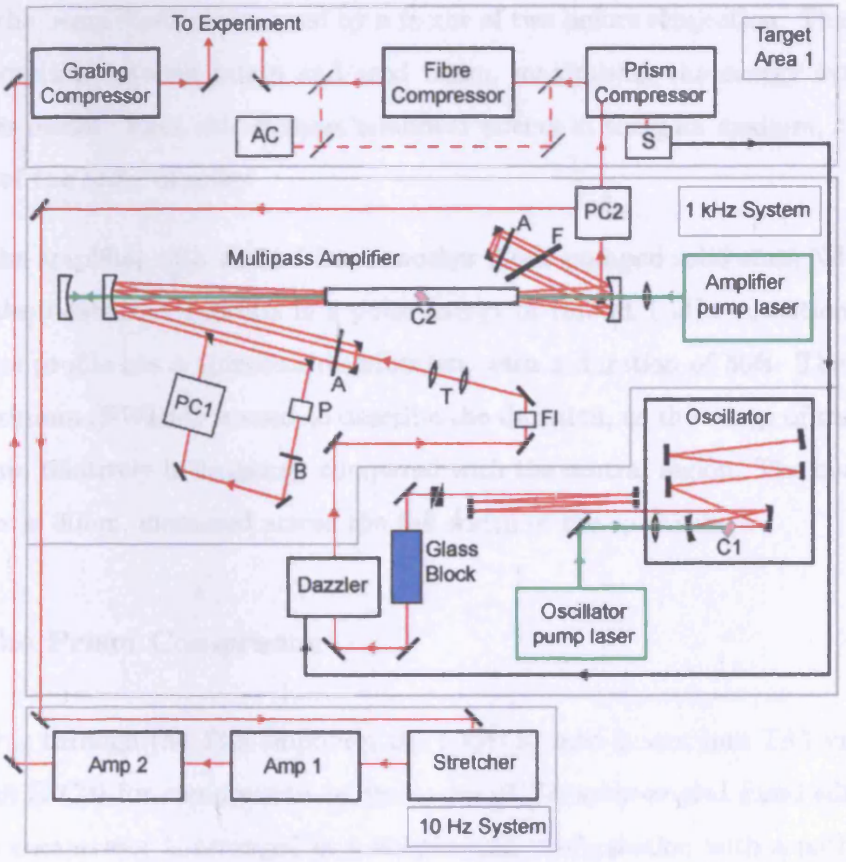

Figure 3.1: Schematic of Astra laser system, showing the 1kHz CompactPro oscillator and amplifier in detail. The 10Hz system and the Target Area 1 compressors are detailed in later figures. C1,2 Ti:Sapphire crystals; FI, Faraday Isolator; T, demagnifying telescope; A, apertures; P, polariser; F, filter; B, Berek polarisation compensator; PC1,2 Pockels Cell. Pulse diagnostics: S, SPIDER; AC, Autocorrelator.

This amplifier, shown in Figure 3.1 consists of two curved mirrors, two retroreflectors and a 3.5mm thick Ti:S crystal C2, which is cut at the Brewster angle to minimise losses. To reduce the effect of thermal lensing, the crystal is housed in a vacuum chamber and cooled to -15°C. One of the retroreflectors is made up of two chirped mirrors designed to pre-compensate for the higher-order dispersion in the prism compressor and the material dispersion from the amplifier. After four passes through the crystal a Pockels cell (PC1) selects pulses at 1 kHz from the 75 MHz pulse train, and also suppresses the amplified spontaneous emission (ASE) arising from the first four passes. The selected pulses the are reinjected for a further six passes of the amplifier, where a 1μs long ASE background of 210nJ energy is unavoidably acquired. Before the last two passes, the pulse is coupled out again and the beam diameter reduced by a factor of two before reinjection. This optimises the mode overlap between pump and seed beam, maximising the energy extraction in the last two passes. Also, this reduces nonlinear effects in the gain medium, keeping the B-integral of the order of unity.

Pumping the amplifier with 10.5mJ from another diode-pumped solid state Nd:YLF laser (Jade, Thales Laser S. A.) results in a pulse energy of 1mJ at 1 kHz repetition rate. The spatial pulse profile has a Gaussian distribution, with a duration of 30fs. The full width at half maximum (FWHM) is used to describe the duration, as the wings of the Gaussian pulse contain relatively little energy compared with the central region. The bandwidth of these pulses is 30nm, measured across the full width of the spectrum.

3.1.2 The Prism Compressor

After passing through the Ti:S amplifier. the 1 kHz output is sent into TA1 via a second Pockels Cell (PC2) for compression by two pairs of Brewster-angled fused silica prisms. This prism compressor is arranged in a double pass configuration with a path length in air of 6m, shown in Figure 3.2.

As light is passed through a prism, the different frequency components are refracted through different angles. This angular dispersion, which deflects the blue component the most, produces a negative chirp on the pulses. Dispersion is controlled within this

compressor by manually altering the path length in glass travelled by the beam, since the second prism pair is mounted on a linear translation stage. By adjusting this distance S (Figure 3.2), the negative chirp can be adjusted to compensate for the positive chirp introduced by the stretcher previously (glass block in Figure 3.1). Some higher order dispersion may still remain in the pulses as this is extremely difficult to remove completely, preventing full transform limited pulse compression to a duration of ≈25fs. When the chirp is removed as much as possible, pulses have a duration of 30fs, which is measured at the output of the prism compressor by in-line autocorrelation (AC).

Pulse Length	30 fs
Energy per Pulse	0.6 mJ
Central Wavelength	790 nm
Repetition Rate	1 kHz
Beam Diameter	10 mm

Table 3.1: Typical prism compressor output

As prisms in this compressor require a horizontally polarised beam, but diagnostics and experiments require vertical polarisation, a periscope (P) after the prism compressor exit rotates the polarisation angle by 90°. In both cases the polarisation direction is perpendicular to the beam propagation axis. The pulses are near-transform limited with a bandwidth of 30nm measured using a fibre optic spectrometer. For an input of 0.9W power output is 0.6W from this compressor.

3.1.3 The Fibre Compressor

On leaving the prism compressor, pulses pass through the fibre compressor (Attosecond Technology UK) which effects further compression of the pulse duration to ≈10fs. In order to support this shorter pulse length, a larger bandwidth is needed. The bandwidth is increased in the Argon-filled hollow core fibre by self-phase modulation (SPM) of the pulses as described in Chapter 2. Group velocity dispersion (GVD) also occurs during the path in air and any transmissive optics. After propagation through the fibre, bandwidth is increased from 30nm to 100nm. Recompression by a series of ten multi-layer chirped mirrors produces a pulse duration of 10fs, measured by on-line autocorrelation and FROG.

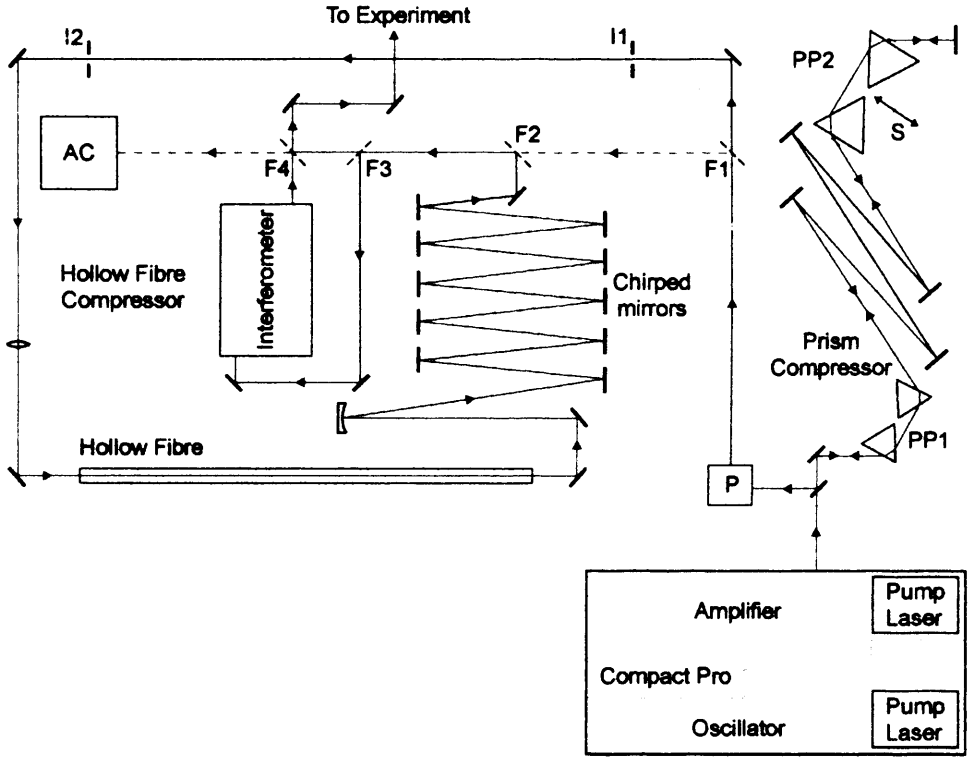

Figure 3.2: Schematic of prism compressor and fibre compressor for the 1kHz laser system. PP1,2. prism pair; P periscope; F1-4. flip mirrors; I1,2 iris; AC, Autocorrelator. Arrow S indicates prism separation for dispersion control. Dotted lines indicate temporary beam paths to the autocorrelator via flip mirrors. Interferometer indicates position of Mach-Zehnder interferometer used for pump-probe experiments (Chapter 5).

A 1m long fused silica hollow fibre wave guide and a series of ten chirped mirrors form the basis of this compressor (Figure 3.2). Single mode propagation of the pulses takes place through grazing incidence reflections at the dielectric inner surface of the fibre, which has a diameter of 250μm. For optimal coupling into the fundamental mode, the laser should be focused into the fibre with a focal diameter 0.65 times the inner channel diameter. This corresponds to a focal spot size of 160μm.

Argon gas is introduced into the hollow fibre by differential pumping. This creates a vacuum at the input end of the fibre, with increasing pressure towards the exit end (0.35bar). Brewster windows at both ends of the fibre minimise transmission losses. The main advantage of a differentially pumped over a statically filled hollow fibre is that it prevents ionisation of the Argon gas at the fibre entrance during laser-fibre coupling leading to plasma generation and a change in the refractive index at the fibre entrance, which will destroy the pulse. Additional advantages are a decrease in the dependency of energy transmission on the input laser pulse, and improved shot-to-shot output energy fluctuations [Robinson et al., 2006].

The fibre compressor is also senstive to the duration of the input pulse. A shorter pulse duration is preferred as this indicates a larger bandwidth, which is then more susceptible to broadening. The input beam is 30fs at 1kHz, with an energy of 0.6 mJ/pulse. The beam is carefully aligned through two alignment irises and focused into the fibre with a 1m focal length lens. A CCD camera images the focused beam coupling into the fibre input. Further adjustments to the alignment can be made by slight movements of the fibre itself, which is mounted with an x-y translation stage at each end.

Pulse Length	$\approx$10 fs
Energy per Pulse	0.25 mJ
Central Wavelength	790 nm
Repetition Rate	1 kHz
Beam Diameter	10 mm

Table 3.2: Typical 10fs laser system output

The spectrally broadened pulses exiting the fibre are collimated by a f = 1m mirror, and are then reflected off a series of multilayer dielectric coated chirped mirrors (Layertec

GmbH) to recompress the pulses temporally. A series of 10 chirped mirrors are used, which also compensate for the previous path length in air and the 3mm thick fused silica input window on the UHV interaction chamber of the TOFMS. Protected silver coated mirrors (Layertec GmbH) which do not induce chirp transport the beam out of the compressor, ready for use in experiments. One of the turning mirrors is mounted in a flip mount, which when lowered sends the beam into the autocorrelator (AC in Figure 3.2).

3.2 10fs 1 kHz Laser System Performance

Differential pumping allows for smooth tuning of the pulse duration of near transform-limited pulses by altering the gas pressure in the fibre. As the energy transmission is constant in the differentially pumped fibre, the spectral bandwidth ($\Delta\omega$) now increases linearly with gas pressure [Tisch et al., 2005] described by the following relationship:

$$\Delta\omega \propto Ep\eta_2/\tau^2 \tag{3.1}$$

where input energy E $\leq$ 1 mJ, p is the gas pressure (bar), η_2 is the nonlinear refractive index per bar of gas pressure and the input pulse duration $\tau \approx$ 30fs. Pulse duration and spectral bandwidth of pulses exiting the fibre compressor were measured using an autocorrelator and a fibre optic spectrometer respectively for a range of gas pressures from 0 bar up to 0.7 bar (Figure 3.3).

For the 0 bar pressure measurement the fibre was evacuated, producing a wavelength spectrum very similar to the input spectrum from the prism compressor as expected. The increase in pulse duration to 47fs from the 30fs input pulse is due to the chirped mirrors over-compensating for dispersion. As the pressure is increased, the spectrum broadens from 30nm to an optimum of 100nm at 0.35 bar, showing amplitude modulations characteristic of a SPM process. The slight asymmetry of the spectrum about the central wavelength can be attributed to the spectrometer detection efficiency, which is maximum at 600nm. Increasing the pressure past 0.5 bar leads to over-broadening, causing energy to be lost into the wings of the pulse and lengthening the pulse duration. Experiments

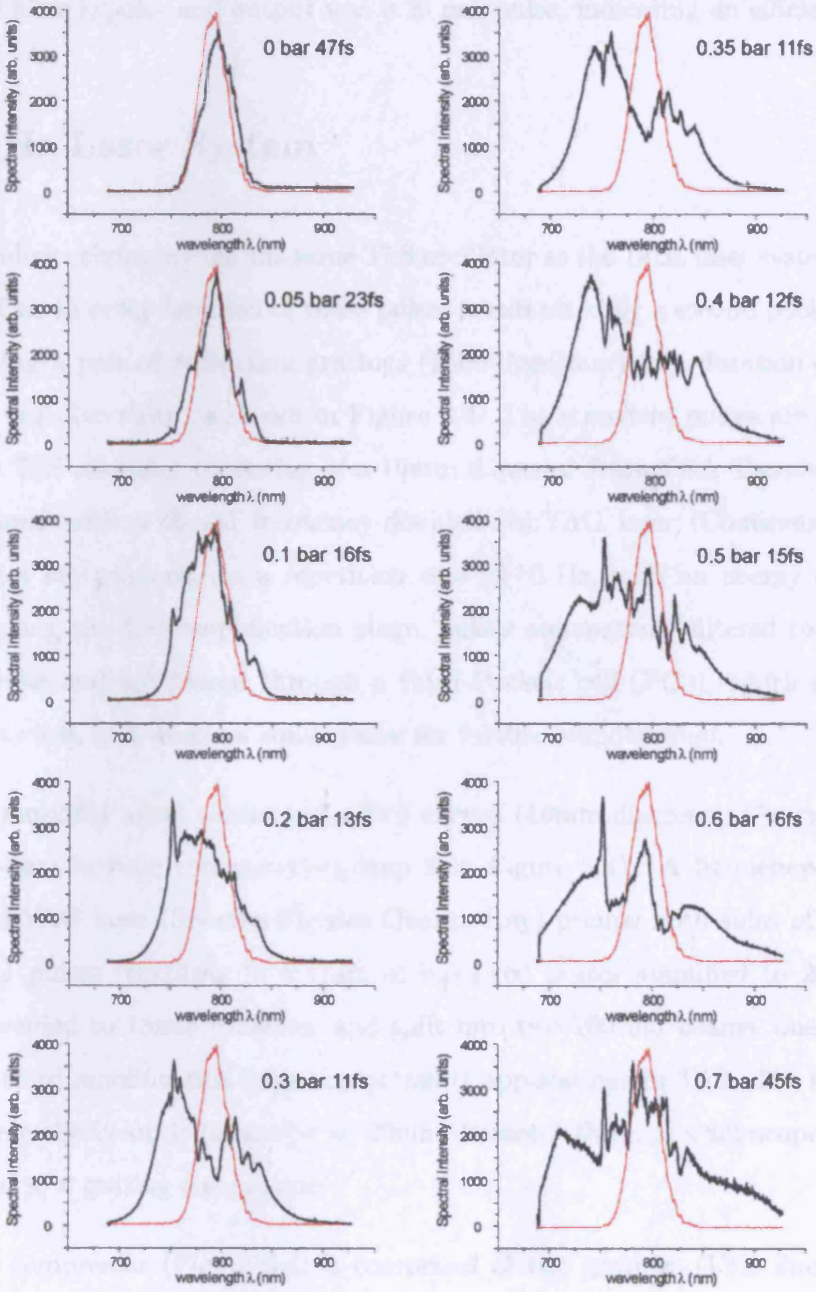

Figure 3.3: Hollow fibre and chirped mirror compressor output wavelength spectra for different gas pressures within the hollow fibre (black). The red graphs show the input wavelength spectrum from the prism compressor for a 30fs pulse. Pulse durations are autocorrelation measurements. Optimum spectral broadening is obtained at a gas pressure of 0.3-0.35 bar, producing pulses of 11fs duration.

were performed using a gas pressure of 0.35 bar, which produced pulses of 11fs. The input power was 0.67 mJ/pulse and output was 0.29 mJ/pulse, indicating an efficiency of 43%.

3.3 10 Hz Laser System

The 10 Hz pulses originate from the same Ti:S oscillator as the 1kHz laser system described previously. One in every hundred of these pulses is extracted by a second pockels cell, and stretched using a pair of diffraction gratings (1500 lines/mm) to a duration of 530ps, by introducing negative chirp as shown in Figure 3.4. The stretched pulses are amplified in a three-pass Ti:S amplifier consisting of a 10mm diameter 7mm thick Titanium Sapphire crystal pumped with a 65 mJ frequency-doubled Nd:YAG laser (Continuum Surelite). Output pulses are produced at a repetition rate of 10 Hz, with an energy of 5 mJ per pulse. Following the first amplification stage, pulses are spatially filtered to smooth the intensity profile and are passed through a third Pockels cell (PC3), which removes any pre- or post-pulses and selects a single pulse for further amplification.

The second amplifier again consists of a Ti:S crystal (10mm diameter, 12mm thick), now with a four-pass bow-tie configuration(Amp 2 in Figure 3.4). A frequency-doubled Q-Switched Nd:YAG laser (Spectra Physics Quanta-Ray) pumps both sides of this crystal with 400 mJ pulses, resulting in a train of infra red pulses amplified to 200 mJ. The beam is expanded to 18mm diameter and split into two 100 mJ beams, one of which is passed to a third amplification stage for petawatt applications in TA2. The other is sent to TA1. where the beam is expanded to 20mm diameter through a telescope and finally recompressed in a grating compressor.

The grating compressor (Figure 3.4) is comprised of two gratings (1500 lines/mm), one of which is mounted on a manually adjustable, micrometer accuracy linear translation stage allowing their separation to be changed. A periscope P1 is used to change the polarisation direction to horizontal before the beam entrance. The amount of positive chirp is controlled by the separation of the gratings, which is set so that the negative chirp induced by the stretcher in the first stage of CPA is compensated for. Pulses are

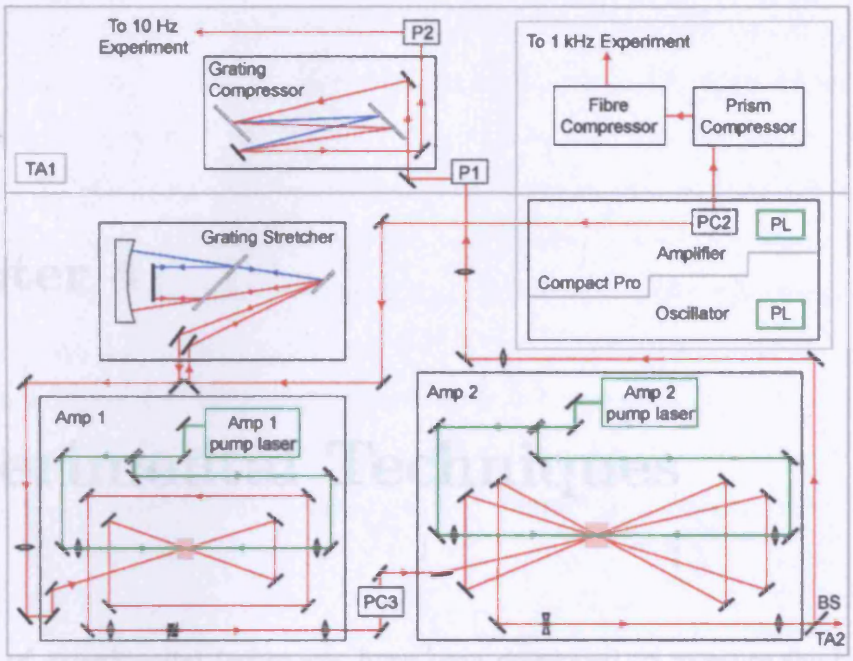

Figure 3.4: Schematic of Astra femtosecond laser 10Hz system. Details of the stretching stage, amplifiers 1 and 2 and compression stage of CPA are described in the text. PC2,3 Pockels Cells; P1,2 periscopes; BS, beam splitter; PL, pump laser.

Pulse Length	40 fs
Energy per Pulse	20 mJ
Central Wavelength	790 nm
Repetition Rate	10 Hz
Beam Diameter	20 mm

Table 3.3: Typical 10 Hz laser system output

recompressed from 530ps to a typical pulse duration of 40fs. These longer laser pulses are utilised in the intensity selective scan technique (Chapter 5) to produce results which are highly resolved in intensity.

Chapter 4

Experimental Techniques

A number of experimental techniques have been developed to measure the behaviour of atoms and molecules in an intense laser field. The well-established time-of-flight mass spectrometry technique employed in this thesis is described in detail, and an overview of other current experimental techniques will also be given. The time-of-flight method produces a measurable yield of charge states from atomic and molecular targets, while the kinetic energy release can also be obtained for molecular fragmentation.

Two types of apparatus are used for the present experiments; a time-of-flight mass spectrometer and an ion beam spectrometer. They are used to detect the ion fragments generated by the interaction of femtosecond laser pulses with neutral gas targets and ion beam targets respectively.

4.1 Time-of-Flight Mass Spectrometer

The time-of-flight mass spectrometer (TOFMS) consists of three main stages: First, the ions are produced in the interaction region by laser-induced ionisation of a diffuse gas target; in the next stage ions are separated due to their mass and charge in a field free drift region; finally, the ions are detected according to their flight time using a channel plate detector.

A stainless steel ultra high vacuum chamber houses the TOFMS, and is pumped by a turbo-molecular pump backed by an oil-free diaphragm pump. To attain a base pressure of 5 x 10^{-10}mbar (measured by a hot cathode Bayard-Alpert ionisation gauge) the chamber is heated to 120°C, significantly reducing the amount of contaminant gases and water vapour present. High purity target gas is then introduced into the chamber through a hypodermic needle of internal diameter 150μm behind the interaction region. A needle valve controls the gas flow to a pressure of 3 x 10^{-8}mbar, low enough to avoid space-charge effects [Cornaggia et al., 1990], again measured by the ionisation gauge. The chamber has a fused silica window of 3mm thickness in front of the interaction region, allowing the laser beam to be transmission focused into the interaction region or reflection focused from inside the chamber.

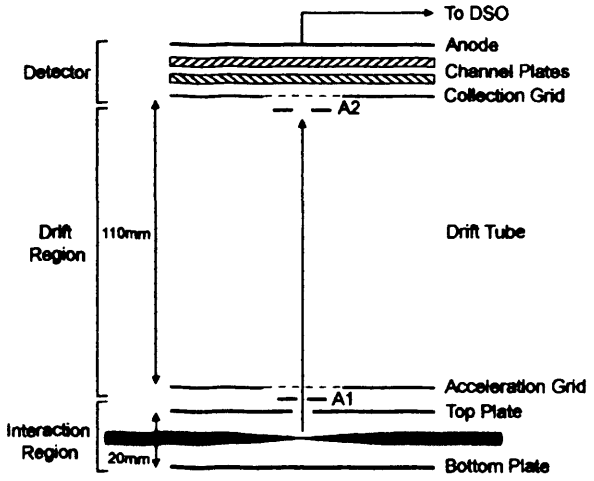

Figure 4.1: Schematic of the Time-of-Flight mass spectrometer. The arrow in the centre shows the path of ion fragments produced by the laser in the interaction region. A1, 250μm aperture; A2, 2mm aperture.

For ion production, the laser beam is focused into the interaction region as shown in Figure 4.1, and the resulting ion fragments are extracted by a uniform potential applied across top and bottom plates. A photograph of the interaction region is shown in Figure 4.2. An aperture (A1) of 250μm diameter directly above the interaction region limits the detector to fragments produced by only a small slice of the laser focus, enabling intensity selective scanning (Chapter 5).

After extraction, the ion fragments pass through a fine tungsten wire grid where a second

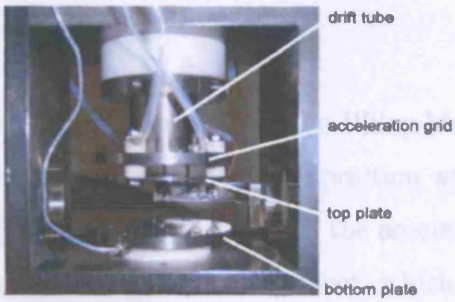

Figure 4.2: Photograph of the Time-of-Flight mass spectrometer interaction region, constructed from stainless steel and insulated with PTFE.

potential accelerates the ion fragments into the drift region. This 110mm long drift region is field free so that the ions are separated in time according to their mass and charge. Another aperture (A2) of 2mm diameter is located at the top of the drift tube, increasing the angular resolution. Ion fragments then arrive at the detector, where an applied potential to the collection grid accelerates them on to a pair of 2mm thick Philips Photonics G25-25DT/13 channel plates. These plates are made up of a series of 25μm channels at an angle of 13° to the TOFMS axis, and are mounted in a chevron formation to reduce back scatter. Incident ions produce electron cascades with a gain of $\approx 10^7$ in these microchannels due to the high voltage (2.8kV) that is applied across the channel plates. Finally, the signal is collected by an anode and sent to a digital storage oscilloscope which records the time-of-flight spectra (Figure 4.3).

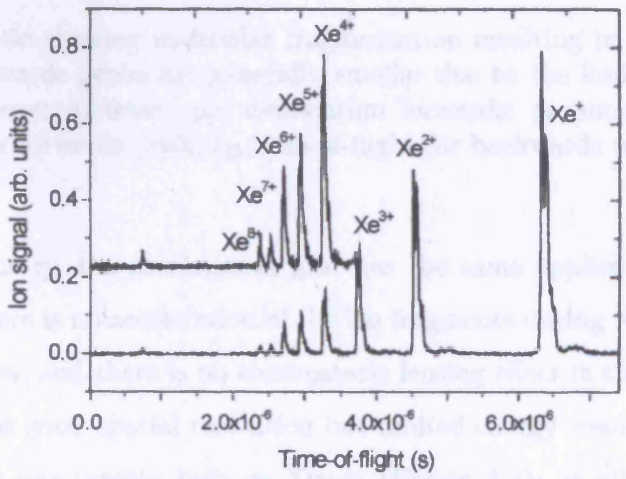

Figure 4.3: A typical time of flight spectrum from the TOFMS showing 8 charged states of Xenon produced by the 1 kHz 11fs laser at Astra.

4.1.1 Configuration of the TOFMS

The TOFMS can be operated in two modes. In the Wiley-McLaren geometry, the total flight time of the ions is independent of their initial position within the interaction region [Wiley and McLaren, 1955]. The voltage applied to the acceleration grid in Figure 4.1 is increased in this geometry to produce a lensing effect, which causes charged fragments of different initial fragmentation energies to spatially separate in the drift region. This enables good energy resolution of the ions created by the laser in a molecular gas target, where charged fragments can be projected in a forwards or backwards direction with respect to the detector (Figure 4.4), as ion arrival time becomes a function of kinetic energy. However, this lensing effect results in a loss of positional information; if this is required the Spatial mode is used.

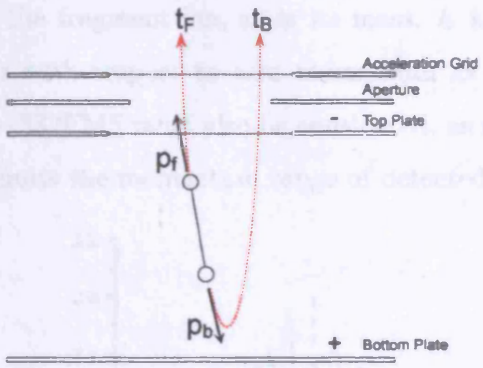

Figure 4.4: Schematic showing molecular fragmentation resulting in forwards and backwards peaks. Backwards peaks are generally smaller due to the limited detector acceptance angle of the spectrometer. p_f, momentum forwards; p_b, momentum backwards; t_F, time-of-flight for forwards peak; t_B,time-of-flight for backwards peak. Adapted from [Goodworth, 2002].

In the Spatial geometry, the acceleration grid has the same applied voltage as the top plate. Therefore, there is no acceleration of the ion fragments during their extraction from the interaction region, and there is no electrostatic lensing effect in the drift region. As a result, this mode has good spatial resolution but limited energy resolution. It is suitable for studying atomic gas targets such as Xenon (Figure 4.3), as all the ion fragments are initially produced with thermal energy. An example of the voltages applied when using Spatial or Wiley McLaren modes in the TOFMS for H_2 are given in Table 4.1. A

	Spatial	Wiley McLaren
Acceleration Grid	20V	60V
Top Plate	20V	20V
Bottom Plate	20V	20V

Table 4.1: Voltages applied to the TOFMS for the detection of H^+ ions from a H_2 target for Spatial and Wiley-McLaren configurations.

comparison of time-of-flight spectra taken in both configurations for a Hydrogen gas target is shown in Figure 4.5. The improved energy resolution of the forwards and backwards H^+ peaks in the Wiley-McLaren geometry is apparent in (a). Kinetic energy of the ion fragments can be calculated from this spectrum using a kinematic equation of motion:

$$KE = (qE\Delta t)^2/2m \tag{4.1}$$

where q is the charge of the fragment ion, m is its mass, E is the extraction field and t is the ion time of flight with respect to zero momentum as shown in Figure 4.5 (a). Collection efficiency of the TOFMS must also be considered, as reducing the aperture size improves resolution but limits the momentum range of detected ions [Bryan, 2001].

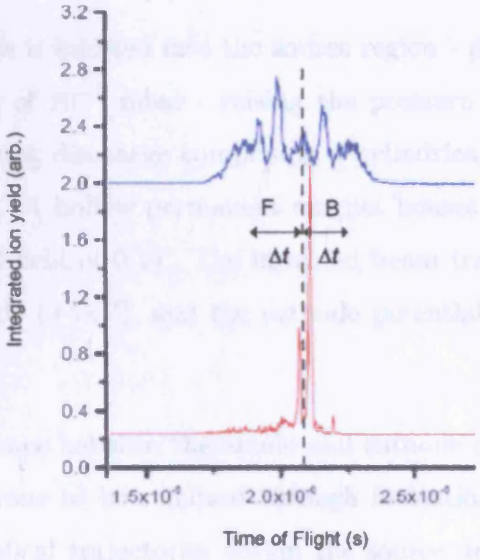

Figure 4.5: A comparison of H spectra from H^2 taken with the two different TOFMS configurations. Blue spectrum (top) Wiley-McLaren, red spectrum (bottom) Spatial. F and B refer to forwards and backwards peaks. Δt is the ion time of flight with respect to zero momentum.

4.2 Ion Beam Spectrometer

This apparatus enables experiments using a beam of positive ions with a known vibrational distribution. The ion beam apparatus has five main sections; the ion source and extraction lens system, momentum selection, focusing and deflection, interaction region and the detector. A schematic is shown in Figure 4.6.

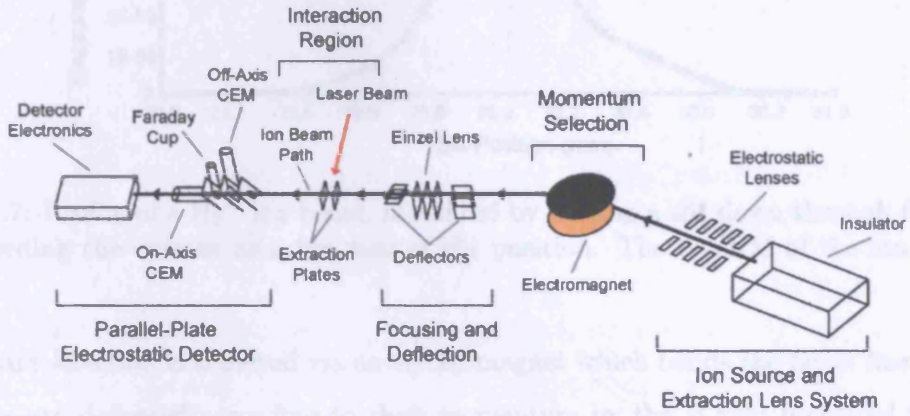

Figure 4.6: Schematic of the ion beam spectrometer showing the five main sections. CEM, channel electron multiplier.

Spectrally pure neutral gas is injected into the source region - pumped by a turbo pump to a background pressure of 10^{-7} mbar - raising the pressure to 3 x 10^{-6} mbar. The source is a compact Penning discharge comprising a cylindrical anode surrounded by a larger cylindrical cathode. A hollow permanent magnet houses this source, producing a confining permanent axial field of 0.1T. The intended beam transport energy is applied as a potential to the anode (+2kV), and the cathode potential (-1.5kV) is floated with respect to this voltage.

The large potential difference between the anode and cathode creates a discharge in the neutral gas causing electrons to be removed through ionisation, creating positive ions. Free electrons move in helical trajectories within the source due to the Lorenz force of the crossed electric and magnetic fields. This increased path length causes collisional ionisation within the neutral gas, producing a low energy plasma. Source conditioning optimises the production of a particular charged state. The ions are then accelerated out

by the potential through a 2mm extraction aperture, and the resulting beam is controlled by a series of five electrostatic lenses. The beam is stable for long periods, typically days.

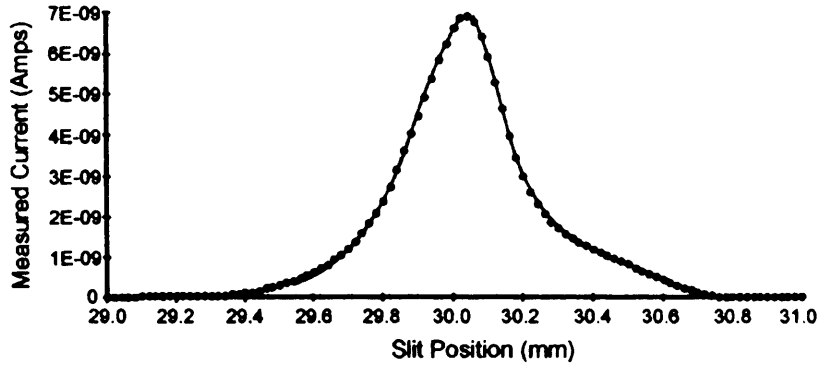

Figure 4.7: Profile of a H_2^+ ion beam, measured by driving a slit down through the beam and recording the current as a function of slit position. The FWHM of the ion beam is 0.4mm.

Momentum selection is achieved via an electromagnet which bends the beam line through 30°. Ions are deflected according to their momentum by the B-field produced from the current-controlled magnet. A rectangular 2mm wide aperture selects only those ions with the desired momentum, producing an ion beam of a single species. The beam is loosely focused into the interaction region by a combination of an Einzel lens with horizontal and vertical electrostatic deflectors.

The interaction region is defined by a pair of extraction plates, each with a centrally located 10mm aperture to allow the ion beam into the region and provide an exit for products of the interaction. The laser beam passes through the centre, perpendicular to the ion beam path. Polarisation is usually linear and orientated parallel to the ion beam propagation direction, optimising the detection of neutral forwards and backwards dissociation products. A beam probe slit can be driven down into the interaction region to measure the ion beam current profile as a function of slit position, as shown in Figure 4.7.

All products from the laser interaction and the initial ion beam are passed into the parallel plate analyser for separation before detection (see photograph 4.8). The analyser is constructed from three parallel 2mm thick stainless steel rectangular plates, orientated at

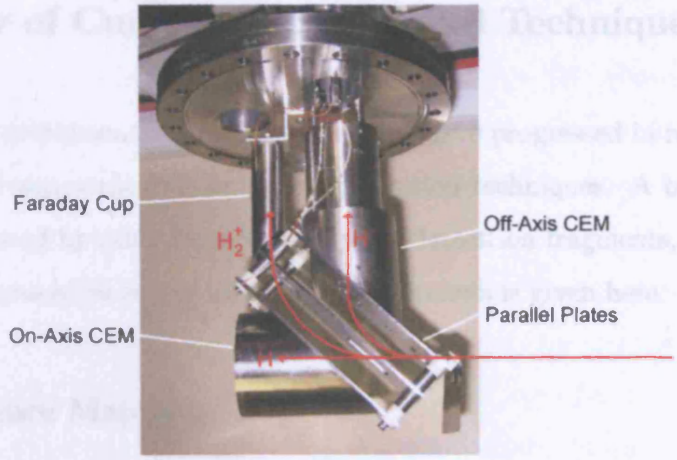

Figure 4.8: Photograph of the parallel plate analyser and detectors. Red lines show the paths of the ion beam H_2^+into the Faraday cup, the H^+ ion fragments into the off-axis CEM, and the neutral H fragments into the on-axis CEM.

45° to the ion beam propagation direction. Potentials are applied to the plates such that the front plate is at earth and the rear and middle plates are supplied in a two-to-one ratio, with the exact potential dependent on the ion species.

Neutral fragments are not deflected by the parallel plate analyser, and therefore pass through to the on-axis channeltron for detection. In order to protect the on-axis channeltron detector from saturation, the ion beam can be pulsed by application of a square wave pulse train to the horizontal deflector plates, although this is not a requirement of the experiments detailed here. Ion fragments are deflected by the middle plate and bent into the off-axis channeltron by a negative potential, where they are detected. As the initial ion beam is more energetic and of greater mass than the ion fragments, it passes through the middle plate and is deflected by the larger potential of the rear plate into the Faraday cup. As in the TOFMS, the resulting channeltron signal is collected as a potential difference with respect to earth and sent to the digital storage oscilloscope, which records the ion spectra.

4.3 Review of Current Experimental Techniques

Advancements in experimental imaging technology have progressed in recent years alongside the developments made in laser pulse generation techniques. A brief review of the current methods used by other research groups to detect ion fragments, electrons or both in coincidence produced in strong laser field experiments is given here.

4.3.1 Covariance Mapping

The detection of multiply charged fragments with high kinetic energy has been of particular interest e.g. [Sanderson et al., 1997]. These fragment ions are the result of molecular Coulomb explosion in an intense laser field. A correlation technique using time-of-flight (TOF) spectra to identify the ionisation channel through which the fragments were produced was proposed [Frasinski et al., 1989] called covariance mapping. In a one dimensional TOF spectrum it is not possible to differentiate between the process $[CO^{2+}] \rightarrow C^{+} + O^{+}$ from the processes $[CO^{+}] \rightarrow C^{+} + O$ and $[CO^{+}] \rightarrow C + O^{+}$ as the neutral particles are not detected.

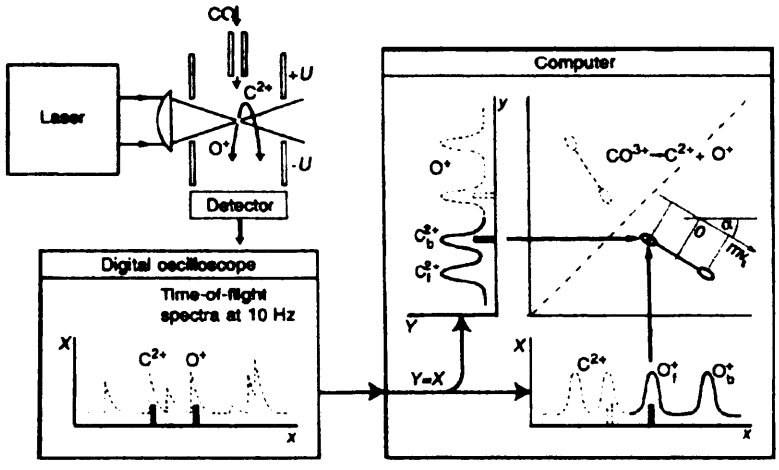

Figure 4.9: The covariance mapping technique illustrated for a particular fragmentation channel of CO described in the text. Subscripts f and b denote forwards and backwards ions as seen by the detector. Adapted from [Frasinski et al., 1989].

To generate a covariance map, an individual TOF spectrum must be collected for each laser

shot, rather than averaging over a number of shots to collect one spectrum. For a particular CO fragmentation channel such as $CO \rightarrow [CO^{3+}] \rightarrow C^{2+} + O^{+}$ (shown in Figure 4.9), if an O^{+} fragment is detected, there is an enhanced probability of detecting a C^{2+} fragment. The covariance between the two TOF points is calculated over many pulses to show a correlation between O^{+} and C^{2+} fragments. To find all correlated channels. the covariance is calculated for each pair of TOF points to create a 2D ion covariance map. This has also been extended to 3 dimensions by our research group for the molecule carbonyl sulfide (OCS) in [Bryan et al., 2006a]. To minimise the possibility of false coincidences which occur when more than one Coulomb explosion event occurs in one laser shot, the gas pressure should be kept low, $\approx 3 \times 10^{-9}$ mbar (10^{-10}mbar backing pressure). This should ensure that only one Coulomb explosion event takes place per laser shot. The covariance mapping technique has also been extended to calculate electron-ion and electron-electron coincidence measurements [Frasinski et al., 1992].

4.3.2 Mass Resolved Momentum Imaging

The momentum of the Coulomb explosion fragments can also be studied by determining the angular distribution of the fragment ions. This technique was developed by [Hishikawa et al., 1988] and is called mass resolved momentum imaging (MRMI) or ion momentum imaging (IMI). To obtain this angular distribution, TOF spectra are collected for a number of different laser polarisation angles with respect to the detector axis. The momentum of the ion fragment is calculated from equation 4.1. The results are combined in polar form to give the signal as a function of momentum and angle with respect to the laser polarisation direction.

A MRMI for O_2 fragmentation in a high intensity laser field is shown in Figure 4.10. Fragmentation channels (1,0) from $O + O^{+}$ and (1,1) from $O^{+} + O^{+}$ are clearly resolved in the image, however when the laser polarisation is orthogonal to the detector axis, high energy fragments are not detected due to the limited acceptance angle of the detector.

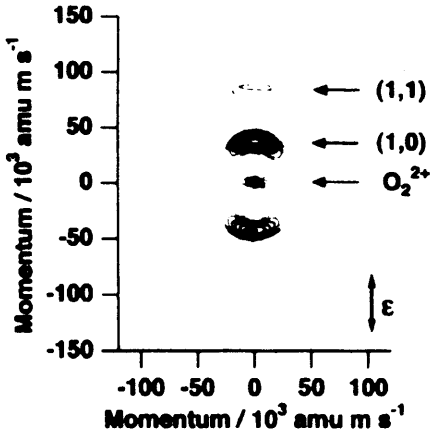

Figure 4.10: Mass resolved momentum image of O^+ produced from O_2 in a 795nm 2 $\times$ 10^{14} Wcm^{-2} laser field. The laser polarisation vector ε is indicated by the arrow. Figure reproduced from [Hishikawa et al., 1988].

4.3.3 Electron-Ion Coincidence Experiments

When performing photoionisation experiments it is an advantage to detect both the photoion and photoelectron fragments in coincidence as both can provide important information on the ionisation event [Lafon et al., 2001]. Such a photoion-photoelectron coincidence experiment (PEPICO) usually requires two TOF detectors, one for ions and one for electrons as shown schematically in Figure 4.11. Here, the laser beam is crossed with a continuous molecular beam causing ionisation. Following an ionisation event, the electron is accelerated towards a time and position sensitive detector in a direction perpendicular to both laser and molecular beams, and the ion is accelerated in the opposite direction towards a similar detector. The detector records the arrival time, and therefore the fragment velocity in one direction, while the other two dimensions of the particle velocity are obtained from the position of the fragment. The arrival time of the ion also provides mass selection. As the particles are detected in coincidence, less than one ionisation event per laser shot is required to prevent false coincidences. The detection of many coincidence events leads to a complete 3D ion and electron velocity distribution.

A full 3D measurement of the energy and angular distributions for coincident fragment ions and electrons is particularly useful for the study of double ionisation. The electron spectra correlated to the single and double ionisation of xenon and argon obtained by

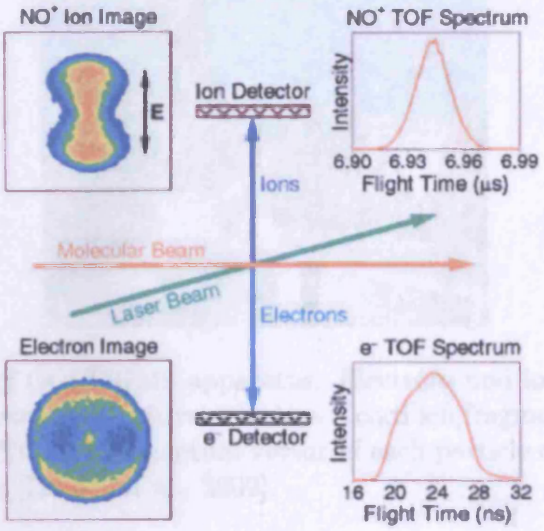

Figure 4.11: Schematic diagram of PEPICO imaging apparatus. Detector images and TOF spectra for NO^+ ions and coincident electrons are shown for the dissociative ionisation of NO_2 at 375.3nm. Each TOF spectrum is measured along the direction of acceleration of the charged particles, while each image is recorded in a plane perpendicular to this direction. Arrow E indicates the direction of laser polarisation, parallel to the detector planes. Figure reproduced from [Davies et al., 1999].

[Chaloupka et al., 2003] is consistent with the recollision model for argon, but indicates an underlying transition in the double ionisation of xenon, perhaps involving multiphoton processes.

4.3.4 COLTRIMS

Although the electron-ion coincidence experiments described in section 4.3.3 have produced important results, there still remains an experimental challenge to detect more than one electron from a multiple ionisation event. Conventional electron spectrometers usually cover only a small part of the total 4π collection solid angle and therefore fails to detect all electrons emitted. This problem has been solved by the COLTRIMS (Cold Target Recoil Ion Momentum Spectroscopy) technique [Ullrich et al., 2003] as it provides a 4π collection solid angle for low energy electrons up to a few hundred eV, as well as 4π solid angle and high resolution detector for coincident ion momentum imaging.

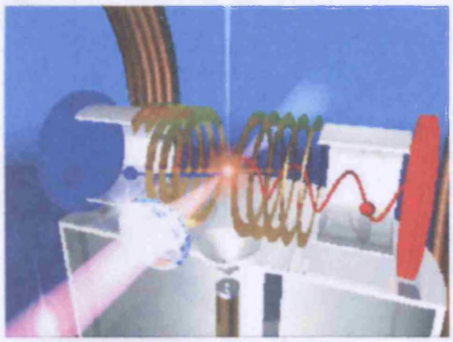

Figure 4.12: Diagram of COLTRIMS apparatus. Electrons and ions are created in a supersonic gas jet. TOF position sensitive detectors record ion fragments (left) and electrons (right) in coincidence. The 3D momentum vector of each particle can then be calculated. Figure reproduced from [Dorner et al., 2002].

In most atomic interactions with photons, the ion momenta are of the same order of magnitude as the electron momenta. However, because of their mass the ion energies are in the range of μeV to meV, which are below thermal motion at room temperature. As a result the atoms must be substantially cooled, usually by a supersonic gas jet which reduces the initial momentum spread to below 0.1au in the direction of the laser polarisation (along z-axis in Figure 4.12).

Ions generated by the focused laser are guided towards the position sensitive channel plate detector by a weak electric field. From the position of impact and time-of-flight all three components of the momentum vector and the charge state are obtained. Electrons are also guided to a second position sensitive detector by the electric field, but to detect electrons with large transverse energies a homogeneous magnetic field is applied parallel to the electric field. The electrons therefore travel in a cyclotron trajectory towards the detector. For a magnetic field of 10 Gauss, 4π solid collection angle is achieved for electrons up to 30eV. The typical detection probability of an electron is 30% to 40%, so in most cases only one electron is detected for multiple ionisation. However, by detecting one electron in coincidence with the ion the momentum components of the second electron can be calculated through energy conservation [Weckenbrock et al., 2004].

Chapter 5

Laser Techniques

Ultrashort laser pulses can be exploited to obtain the maximum time and energy resolution in experiments. The pump-probe technique is commonly used to build up an image of the molecular dynamics with respect to the time delay between pump and probe pulses. Pulses of the order of 10fs are employed to temporally resolve molecular motion. When using longer pulses of 40fs, an intensity selective scanning method is employed, which utilises the entire intensity range of the laser focal region. Properties of the focused laser beam are discussed, including diffraction effects.

5.1 Properties of Gaussian Beams

In the fundamental TEM_{00} mode, the beam is a plane wave propagating along z with a Gaussian intensity profile in r, described by:

$$I = I_0 \exp\left(\frac{-2r^2}{\omega_0^2}\right) \tag{5.1}$$

where I_0 is the peak on-axis intensity and ω_0 is the beam waist. The Fourier transform of this distribution is also Gaussian, so that as the beam propagates throughout the laser system its profile retains this Gaussian distribution [Siegman, 1986].

5.1.1 Gaussian Beam Focusing

The laser beam is focused using transmissive optics (for ≈40fs pulses) or reflective optics (for ≈10fs pulses) for the present experiments. It is useful to know the dimensions of a focused laser pulse and the intensity associated with its spatial distribution, as some experiments in this thesis are performed by scanning across the focal volume. The parameters of the laser confocal volume shown in Figure 5.1 are described here.

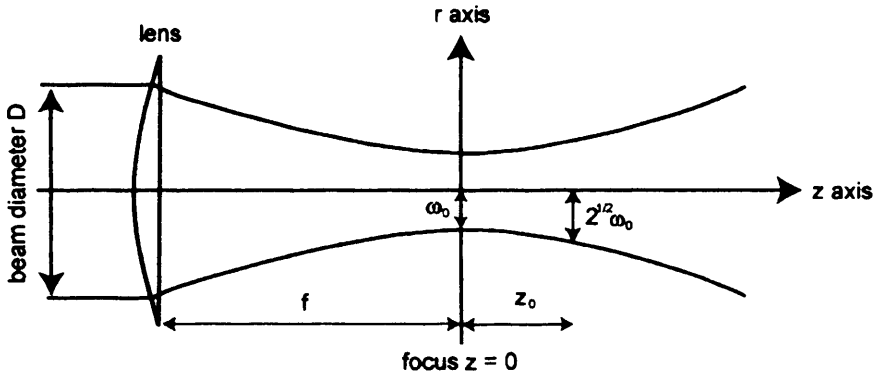

Figure 5.1: Geometry of a laser beam focused by a lens of focal length f.

A Gaussian laser beam of wavelength λ and diameter D can be focused to a point by a lens of focal length f (Figure 5.1). The minimum waist ω_0 of the focused beam can be calculated:

$$\omega_0 = \frac{2f\lambda}{\pi D} \tag{5.2}$$

The Rayleigh range z_0 is defined as the distance along the propagation axis at which the waist expands to $\sqrt{2}\omega_0$, and is also known as the depth of focus:

$$z_0 = \frac{\pi\omega_0^2}{\lambda} = \frac{4\lambda f^2}{\pi D^2} \tag{5.3}$$

A general equation for the size of the beam waist at a distance z from the focus, ω_z, can also be calculated from:

$$\omega_z = \omega_0\sqrt{1+\left(\frac{z}{z_0}\right)^2}. \tag{5.4}$$

The intensity at the focus (z=0) can be calculated from these dimensions. The peak intensity of a focused laser pulse of duration τ is given by the power divided by the

cross-sectional area at the focus

$$I_0 = \frac{2E}{1.06\tau\pi\omega_0^2} \tag{5.5}$$

where E is the energy of the laser pulse. Intensity variation along the propagation axis (z-axis) is Lorentzian, and can be determined from

$$I_z = \frac{I_0}{1+\left(\frac{z}{z_0}\right)^2} \tag{5.6}$$

where I_z is the local on-axis peak intensity. As the radial intensity distribution is Gaussian, the entire intensity profile of the laser pulse is given by:

$$I_{r,z} = \frac{I_0}{1+\left(\frac{z}{z_0}\right)^2} \exp\left(\frac{-2r^2}{\omega_0^2\left[1+\left(\frac{z}{z_0}\right)^2\right]}\right). \tag{5.7}$$

Equation 5.7 can be rearranged and solved for a particular intensity $I_i = I_{r,z}$ to find the radial component r_i of the isointensity contour:

$$r_i = \frac{\omega_0^2}{2}\left[1+\left(\frac{z}{z_0}\right)^2\right]\left[\ln\left\{\frac{I_0}{I_i\left[1+\left(\frac{z}{z_0}\right)^2\right]}\right\}\right]^{\frac{1}{2}} \tag{5.8}$$

The full isointensity contour within the focal volume where the intensity is above the value I_i can be determined by a spatial integration of equation 5.8 over both the radial (r) and axial (z) directions [Posthumus, 2001]:

$$V(I > I_i) = \pi\omega_0^2 z_0\left[\frac{2}{9}\left(\frac{I_0}{I_i}-1\right)^{\frac{3}{2}} + \frac{4}{3}\left(\frac{I_0}{I_i}-1\right)^{\frac{1}{2}} - \frac{4}{3}\tan^{-1}\left(\frac{I_0}{I_i}-1\right)^{\frac{1}{2}}\right] \tag{5.9}$$

At high intensity as I approaches I_0, the first term of equation 5.9 dominates, and the volume increase is proportional to $I^{3/2}$.

The laser is generally assumed to retain its Gaussian distribution throughout beam propagation and focusing, in which case the equations given above provide an accurate description of the intensity distribution at focus. However, any apertures (such the focusing lens)

in the beam path which are of a similar diameter to that of the beam cause diffraction. This produces a significant effect on the intensity distribution of the confocal volume, which will be described in section 5.3.

5.1.2 B-Integral

Degradation of the beam profile can arise as a result of the beam propagation through transmissive optics. The quality of the beam is affected by non-linear optical effects as it passes through elements such as lenses. This non-linear interaction is called the Kerr effect, which occurs at high intensities and results in self-focusing of the beam. The Kerr effect generates a non-linear polarisation in the transmissive optic, which alters the refractive index. As the beam propagates through the optic, the refractive index n for the beam changes as

$$\Delta n = \eta_2 I \tag{5.10}$$

where η_2 is the non-linear index for the optic material, and I is the beam intensity. A time dependent phase shift is accumulated during the passage, which is called the B-integral:

$$B = \frac{2\pi}{\lambda} \int \eta_2 I(z) dz \tag{5.11}$$

where $I(z)$ is the beam intensity at a position along the beam axis z. The perfect optical system would have a B-integral of zero, although this is generally unattainable. The 10 Hz ASTRA laser system ($\approx$40fs) has a typical B-integral value of 2, while the 1 kHz ASTRA laser system has a B-integral $\leq$1. For values of $3 \leq B \leq 5$ self-focusing can occur, which results in an increased intensity that can damage optical components.

5.2 Intensity Selective Scanning

Intensity selective scanning (ISS). first proposed by [Hansch et al., 1996], is employed to obtain the volume-independent ionisation probability. In the present work, the 40fs 10Hz laser system was used. This ISS technique exploits the 250μm ion aperture positioned in

the top plate of the interaction region on the TOFMS (Chapter 4), which limits the region of confocal volume of the focused high intensity laser pulse that the detector is exposed to. Previous studies on ionisation processes of atomic and molecular gas targets tend to utilise the entire focal volume of the laser, so that the detected signal (S) is integrated over the range of intensities present along the radial (r) and propagation (z) directions:

$$S = \int\int_{r,z} S(I(r,z))drdz = \int_0^{I_0} S(I)dI \tag{5.12}$$

where I is intensity with I_0 being the peak intensity. This integration over spatial coordinates complicates the study of intensity dependent processes.

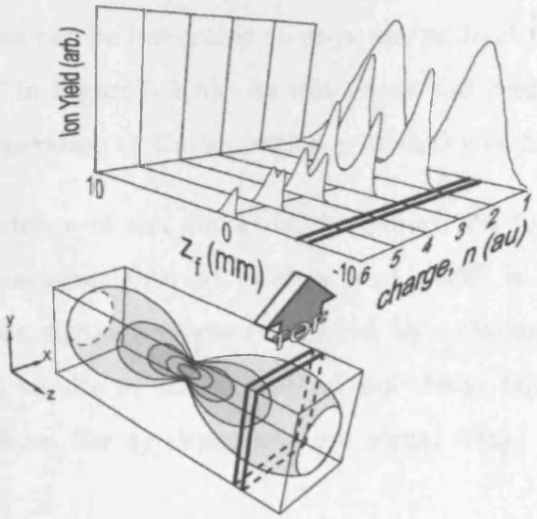

Figure 5.2: Diagram showing the process of Intensity Selective Scanning. A Time-of-Flight spectrum is taken at each position z_f as the laser focus is translated along the propagation (z) axis. The ion yield for each charged state is plotted on the graph. From [Bryan et al., 2006c].

With the Intensity Selective Scanning method, the 250μm aperture permits only ionisation fragments produced from a small slice of the laser confocal volume into the drift tube. The laser focus is translated along the propagation direction z, so that ionisation is produced and subsequently detected from consecutive slices through the focus (Figure 5.2). In this way, the entire laser focus can be scanned with respect to the local peak on-axis intensity $I_0(z)$. Radial intensity variations within each slice can be calculated from equation 5.9,

where the isointensity volume above I_i is:

$$V(I > I_i) = \frac{\pi}{2}\omega_0^2 \Delta z \left[1 + \left(\frac{z}{z_0}\right)^2\right] \ln\left\{\frac{I_0(z)}{I_i}\right\} \tag{5.13}$$

where Δz is the 250μm width of the aperture. The volume between two intensity values can be found by subtraction, i.e. $V(I > I_i) - V(I > I_{i+1})$. This equation has been used to generate theoretical Gaussian volumes as a function of z_f in order to model experimental ISS data by [Goodworth, 2002].

When the ISS technique is applied, good resolution of intensity dependent features is observed as can be seen from the well resolved charge states of Xe in Figure 5.3(a). The individual charge states can be integrated to show the amount of ionisation as a function of z_f, shown for Xe^{2+} in Figure 5.3(b). As this result still contains focal volume effects, it is not a clear representation of the ionisation probability of Xe^{2+}.

To remove the dependency of the ionisation probability on focal volume for each slice of the ISS, a technique established by [Walker et al., 1998] is employed. This is called deconvolution of the ion signal, and can be applied for a Gaussian or non-Gaussian laser focus. Deconvolution results in the ionisation probability $\Omega(I)$ as a function of laser intensity, calculated from the z_f dependent ion signal $S(z_f)$ via the on-axis intensity distribution $I_{ax}(z_f)$:

$$\Omega[I_{ax}(z_f)] \propto \left(\frac{I_{ax}(z_f)}{dI_{ax}(z_f)/dz_f}\right) \frac{d}{dz_f}[I_{ax}(z_f)S(z_f)] \tag{5.14}$$

When repeated for each slice of the ISS, this produces the amount of ionisation as a function of intensity with all focal volume effects removed. For a Gaussian confocal laser volume, $I_{ax}(z_f)$ is equivalent to the volume calculated in equation 5.13. To apply this equation for a non-Gaussian laser focus, the new on-axis intensity distribution $I_{ax}(z_f)$ must be calculated. This is described in section 5.3.

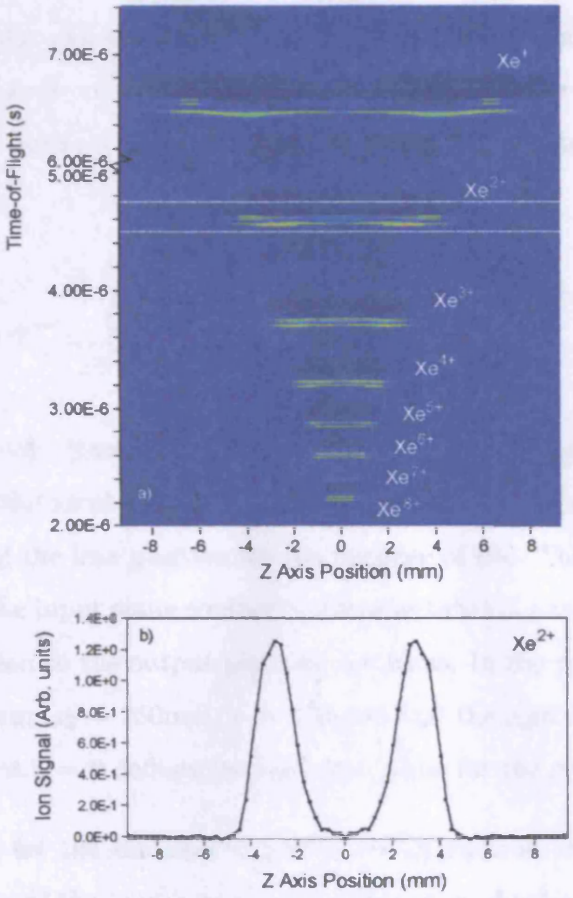

Figure 5.3: An example of an Intensity Selective Scan using Xenon target gas (a). The Xe^{2+} signal is integrated over the time-of-flight as shown in (b). The white lines indicate integration limits.

5.3 Non-Gaussian Deconvolution

All previous studies of ion yield as a function of laser intensity have been dependent on the geometry of the laser focus, which has generally been assumed to be Gaussian. However, diffraction may occur during beam propagation or focusing, affecting the intensity distribution at the laser focus. This could lead to misinterpretation of experimental results. Here, the solution for an arbitrary $ABCD$ optical system is employed to calculate this non-Gaussian geometry dependence from the ISS results, published in [Bryan et al., 2006b]. This takes into account the diffraction at the laser focus caused by an aperture. The experimental ISS set up is shown in Figure 5.4. The dimensions on this diagram correspond to the system matrix:

$$\begin{pmatrix} A & B \\ C & D \end{pmatrix} = \begin{pmatrix} 1-(z_2/f) & z_1+(1-z_1/f)z_2 \\ -1/f & 1-(z_1/f) \end{pmatrix} \tag{5.15}$$

where z_1 and z_2 are the distances between the aperture and lens, and lens and focus respectively, and f is the focal length of the lens. The position $z_f = z_2 - f$ is also shown on Figure 5.4, defining the lens position for the purpose of ISS. The system matrix is the transformation from the input plane containing the aperture via a translation, a refraction, and a second translation to the output plane at the focus. In the present experiment, the values are: $z_1 = 300$mm, $z_2 = 250$mm, $f = 250$mm, and the aperture radius $a = 11$mm. The fixed aperture a at $z = 0$ defines the reference plane for the system matrix.

A solution is derived for the the laser intensity distribution in the focal region, which accounts for diffraction of the laser beam at the aperture a. As the radius of the aperture a is fixed, the beam radius ω_g is varied to produce the conditions of the current experiment. Figure 5.5 shows the results of simulating the focus of the optical system for a range of beam radii. Isointensity contours are drawn around the focus, separated by an order of magnitude. When the beam radius is small ($\omega_g = 5$mm) the focus is identical to the Gaussian focus described by the equations in the previous section. However, as the beam radius is increased the diffraction effects from the aperture become more obvious. When

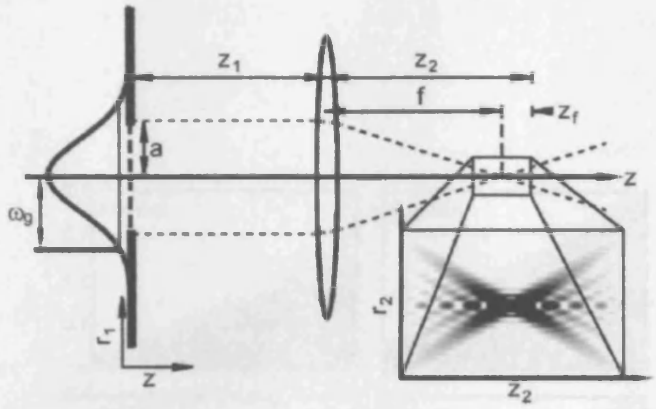

Figure 5.4: Illustration of the cylindrically symmetric optical system employed in the current experiments. The aperture of radius a lies in the input plane at z=0 with radial coordinate r_1. The focus lies in the output plane at $z = z_1 + z_2$ with radial coordinate r_2. The focal length of the lens is f and $z_f = z_2 - f$ is position with respect to the focus. Figure taken from [Bryan et al., 2006b].

the beam radius is comparable to the aperture radius i.e. $\omega_g \approx a$ (Figure 5.5f), peaks and troughs of maximum and minimum intensity within the focus become apparent. This is the case for the current experimental conditions. It can be seen from the isointensity contours that the focal spot size increases along r_2 as the beam radius is increased. This increase is not expected in the case of a purely Gaussian beam.

The deconvolution technique in equation 5.14 is refined to allow for the non-Gaussian nature of the focused beam, and also to remove the dependence of ionisation probability on the intensity distribution within the laser focus, accounting for the presence of diffraction. This is achieved by calculating a new on-axis intensity distribution I_{ax}, equivalent to the intensity U on the output plane at $r_2 = 0, z$:

$$U(r_2 = 0, z) = \frac{\pi}{\lambda BP} \exp(ikz)[\exp(a^2 P) - 1] \tag{5.16}$$

where

$$P = -\frac{1}{\omega_g^2} + \frac{ikA}{2B} \tag{5.17}$$

and $k = 2\pi/\lambda$. Substituting $I_{ax} = |U(r_2 = 0, z_f)^2|$ in equation 5.14 gives the deconvoluted ion signal from which all focal geometry and diffraction effects have been removed. This

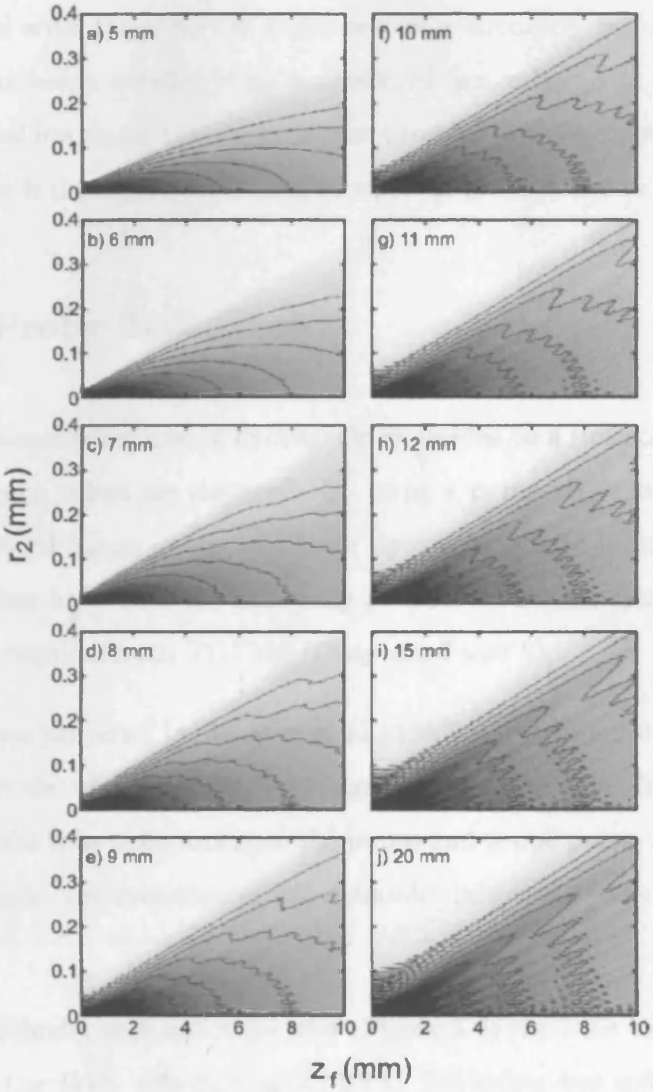

Figure 5.5: Simulated intensity distributions in logarithmic grayscale for the optical system in Figure 5.4. Isointensity contours separated by an order of magnitude are shown. For a)-j) the aperture radius $a = 11$mm is kept constant, while the beam radius ω_g is varied from 5 to 20mm. Diffraction effects are visible even when the aperture is larger than the beam radius. Figure taken from [Bryan et al., 2006b].

can be described as the partial probability of ionisation (PPI) for a particular charge state.

The technique of effective intensity matching (EIM) can also be included in the non-Gaussian deconvolution to enable direct comparison of the results produced by a linearly polarised laser field with those results produced by a circularly polarised field. The intensity of the linear beam is reduced by a measured factor R_{EIM} in order to match the amount of sequential ion signal produced to that produced by a circularly polarised beam. The EIM technique is deployed in Chapter 9, where it is described in greater detail.

5.4 Pump-Probe Technique

To observe the dynamic behaviour of hydrogenic molecules on a timescale of femtoseconds, ultrashort ≈10fs laser pulses are required. By using a pump-probe technique with these pulses, a time resolved image of the molecular dynamics can be built up over a variable delay time. This has been used for the study of vibrational and rotational wave packet dynamics in D_2 molecules in the TOFMS (Chapters 7 and 8).

The method was first proposed by [Dantus et al., 1987]: a pump pulse initiates a dynamic process in the molecule, and a probe pulse images the ion spectrum after a controlled time delay. By varying the time delay between the pump and probe pulses from zero to several hundred femtoseconds, the evolution of the dynamics initiated by the pump pulse can be recorded.

A co-linear Mach-Zehnder type interferometer (Figure 5.6) was built to generate pump and probe pulses from the 1kHz 10fs laser at ASTRA. The beam was split into two, and one arm delayed with respect to the other before being recombined so that the pump and probe pulses are overlapped. Thin (5μm) broadband pellicle beamsplitters were used to split and recombine the beam to minimise the amount of chirp induced by the transmission, which can lengthen the pulse duration. This extreme thinness also virtually eliminates losses and multiple reflections which can lead to ghost images. However, the pulse duration is increased by 2 fs in both arms, from 10fs to 12fs.

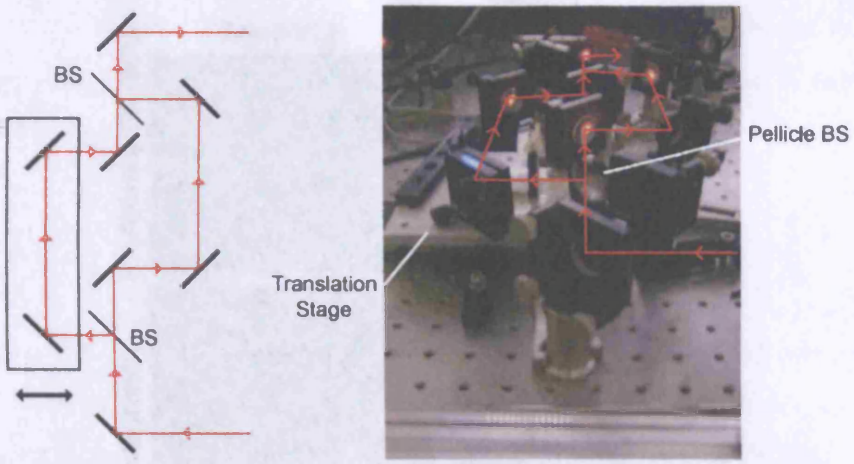

Figure 5.6: Schematic and photograph of the pump-probe interferometer. Red lines show the beam path. BS, beamsplitter.

To produce the time delay, one arm was mounted on a computer driven translation stage, which controlled the probe pulse delay with 300as time resolution. Tests to ensure spatial and temporal overlap of the two pulses at the interaction region are performed at the beginning of each experiment, externally to the TOFMS. Spatially this is achieved by focusing both co-linear beams with a 1m focal length lens onto a heavily filtered CCD camera and adjusting a turning mirror within the interferometer for perfect overlap of the two spots shown in Figure 5.7. For a temporal overlap, the now spatially overlapped pulses are focused into the autocorrelator. The pulses are split and recombined in the SHG crystal, which displays three peaks in the frequency doubled light if the pulses are not quite at temporal overlap as in Figure 5.7. The peaks combine into a single peak in the SHG signal as the translation stage is moved to a position where the temporal and spatial overlap is optimised.

In the fixed (pump) arm, a half-wave plate is mounted to alter the polarisation direction of these pulses. For most experiments, the pump arm polarisation direction is perpendicular to the time-of-flight axis so that any ionisation fragments resulting from these pulses are not detected by the TOFMS. Conversely, the probe arm has a polarisation direction parallel to the time-of-flight axis in order to maximise detection of the ionisation fragments it produces. Some experiments require variation of the polarisation direction of the pump pulses over 90°, which is easily achieved by rotation of the half-wave plate.

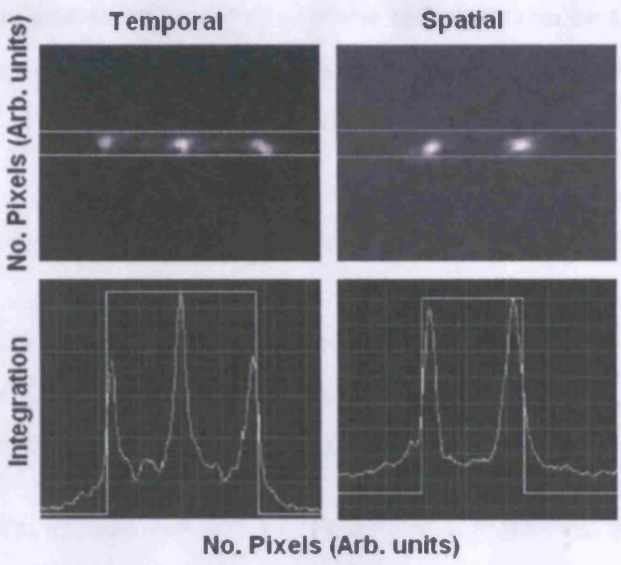

Figure 5.7: Screen shots showing how the pump and probe pulses are overlapped temporally and spatially before each experiment. Spatial overlap is achieved first by focusing the two beams onto a CCD camera, and overlapping the two spots. Temporal overlap is achieved by sending the two spatially overlapped beams into the autocorrelator and moving the translation stage until the three peaks observed in the SHG signal merge into one.

Other methods of creating a pump-probe delay have been employed by different research groups, namely the use of a glass two piece core annulus [Lee et al., 2006]. In this configuration, the central part of the beam passes through the core section of glass and the remaining outer part passes through the annulus of glass surrounding the core section. Each glass optic can be independently rotated about a radius causing the inner and outer sections of the beam to pass through different thicknesses of glass, resulting in a time delay between them.

The advantage of using a core annulus is that the pump and probe beams overlap perfectly in space without the need for beamsplitters. However, limitations of this method may include cropping and diffraction of the beam at large delays which complicates the shape of the focal volume, and the chirp of the pulses due to transmission through glass. Also, it would not be possible to control the polarisation of the pump beam, which is key for the experiments described in this thesis.

For future work, the interferometric pump-probe technique can be tailored to the experiment, using different pulse lengths or wavelengths for pump and probe. A third pulse can also be introduced as a control pulse between the pump and probe.

5.4.1 Pump-Probe as a Pulse Diagnostic

The high resolution and stability of the pump-probe interferometer gives rise to an at-focus laser pulse diagnostic. An indication of the temporal profile of the pulse can be obtained from an experimental pump-probe study of Xenon ionisation in the TOFMS.

In the interferometer, a single 12fs 17μJ pulse is split and one arm is increasingly delayed in 1/3fs steps (the maximum resolution of the computer controlled translation stage) with respect to the other. Pulses are recombined and reflection focused using a f = 75mm spherical mirror into the interaction region of the TOFMS, producing ionisation of Xenon target gas as described previously. Ionisation yields for the first six charge states of Xe are shown in Figure 5.8 on (a) linear and (b) log scale y axes. It can be seen that when the pump and probe delay time is around 0fs the two pulses are overlapped and optically interfere, producing peaks and troughs in the detected ionisation signal. Peak to peak separation of this interference structure is equal to one optical cycle of the laser pulse, which is 8/3fs at the central wavelength of 800nm.

From the signal shown on a linear scale in Figure 5.8(a), it can be seen that maximum interference across all charge states occurs over 30fs, within the time delay region of -15fs to +15fs. This interference in the ionisation yield is delay dependent over this range, arising as the peaks of the two laser pulses overlap. It can be inferred from these results that the duration of the laser pulse is in the region of 15fs, which is in agreement with the autocorrelation measurements of 14fs (pulse duration is increased from 12fs to 14fs within the Mach-Zehnder interferometer).

However, a variation with charge state can also be observed, as there are additional wings present in the interference structure which extend out to almost 100fs in the Xe^+ signal. These wings can be more easily seen in the log plot of the signal in Figure 5.8(b). The

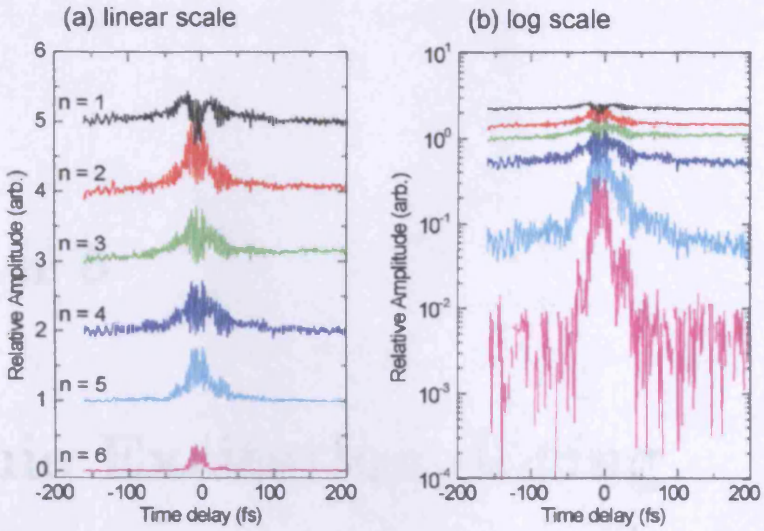

Figure 5.8: Xe^{n+} (n = 1 to 6) ionisation yields as a function of pump-probe delay time (a) on a linear y scale and (b) on a log y scale.

interference in the wings decreases as the charge state increases, which indicates a strong dependence on laser intensity, as a higher intensity is required to produce each higher charge state. It is therefore concluded that the interference in the wings may be due to either a low intensity pulse pedestal or low intensity pre- or post-pulse on the main 14fs laser pulse. A theoretical model is currently under development to simulate the interference produced in the ion signal when two pulses of known duration are overlapped, which will permit a full characterisation of this low intensity pedestal pulse.

Chapter 6

Atomic Excitation during Multi-Electron Tunnel Ionisation

As described in Chapter 1, an ultrafast laser pulse can generate an electric field strong enough to tunnel ionise the valence electrons of an atom. The states of the remaining bound electrons are not normally considered to have any effect on the tunnel ionisation event. However, it has recently been suggested [Kornev et al., 2003], [Fabian et al., 2003] that the ionisation process simultaneously induces *shake-up*; the excitation of one or more remaining electrons to a bound state. A novel experimental technique pioneered by our research group in which both the laser focal geometry and beam diffraction are removed from the results is employed to observe the effects of such an atomic excitation process for the first time. No recollision is produced, which would mask these effects, as a circularly polarised laser pulse is used. The results of this experiment are published in [Bryan et al., 2006c] and [Bryan et al., 2006d].

6.1 Theoretical Studies of Multi-Electron Tunnel Ionisation Dynamics

Theoretical studies of the ionisation process generally employ the single active electron (SAE) model [Eichmann et al., 2000], where only the weakest bound electron interacts with the field, and this electron is assumed to be independent of the remaining electrons which are frozen in their initial configuration. The SAE model has been successfully employed in the past for greater understanding of intense field laser-matter interactions [Scrinzi et al., 1999].

Another simplification required for theoretical calculations is the strong field approximation (SFA). This makes use of the fact that the evolution of electrons in the continuum is dominated by the intense laser field, and that in comparison the Coulomb potential has negligible influence on a free electron. The SAE and SFA are employed for quantum mechanical solutions of the intense field laser-matter interaction because an exact solution requires extremely large computer capacities.

Recent experiments in atoms [Moshammer et al., 2000] and molecules [Hankin et al., 2000] have shown that there are limitations to the SAE approach, leading to the development of new models which include multi-electron tunnel ionisation (METI) effects. These new models attempt to understand the interplay between ionisation and bound electron dynamics in atomic and molecular systems. The shake-up process is considered to be the main excitation mechanism in these studies. As well as shake-up, the related process of *shake-off* has been investigated for the case of double ionisation, where a bound electron is excited and immediately ionised following the ionisation of the first electron.

6.1.1 The Shake-Up Mechanism

The concept of *inelastic tunnelling* was introduced [Zon, 1999], whereby the parent ion can be left in an excited state following the ionisation of one of N identical valence electrons. The initial ionisation diabatically distorts the electron wave functions, resulting in the

excitation of a second electron. This excitation mechanism, called shake-up, was first proposed by [Carlson et al., 1968] to explain single UV photon absorption leading to the ionisation of a first electron followed by excitation of a second electron. It relies on the sudden approximation, which is valid in the case of ultrafast tunnel ionisation if the ionisation potential is far greater than the excitation energy of the ion; a fast (sudden) excitation can be produced in these lower lying states during the tunnelling time.

A general theoretical expression for the rate of N-electron tunnel ionisation has been derived by Zon and Kornev [Kornev et al., 2003] based on the work of Keldysh [Keldysh, 1965]. This new theory is described as multi-electron tunnel ionisation (METI) to distinguish it from standard sequential tunnel ionisation, and accounts for shake-up excitation occurring during tunnel ionisation. As a consequence of this mechanism, a lower intensity is required to ionise subsequent electrons as shown in Figure 6.1.

The similar process of shake-off (where the remaining electrons are ionised rather than excited [Fittinghoff et al., 1992]) has been studied in helium atoms using a linearly polarised laser field, and has recently been investigated theoretically with S-matrix calculations [Becker and Faisal, 2002]. The ratio of shake-off to recollision ionisation was calculated, and it was found that shake-off ionisation was many orders of magnitude weaker. Therefore, the presence of shake-off in strong field ionisation in a linearly polarised laser field is considered to be negligible, and as a result the similar excitation process of shake-up has also been largely ignored. However, our research group has re-examined the evidence for shake-up processes in the case of argon and krypton in a circularly polarised field, as the lowest lying excited states in Ar^{X+} and Kr^{X+} (X = 1 to 6) are easily accessible during tunnel ionisation. This means that excitation of Ar^{X+} and Kr^{X+} can occur within the sudden approximation, contrary to the extremely high excitation energies of He^{+} which are not within the sudden approximation.

6.1.2 *Ab initio* Methods to Calculate METI dynamics

As the number of electrons involved in the tunnelling process increases, the theoretical description becomes more complex. High power computers are necessary for *ab initio*

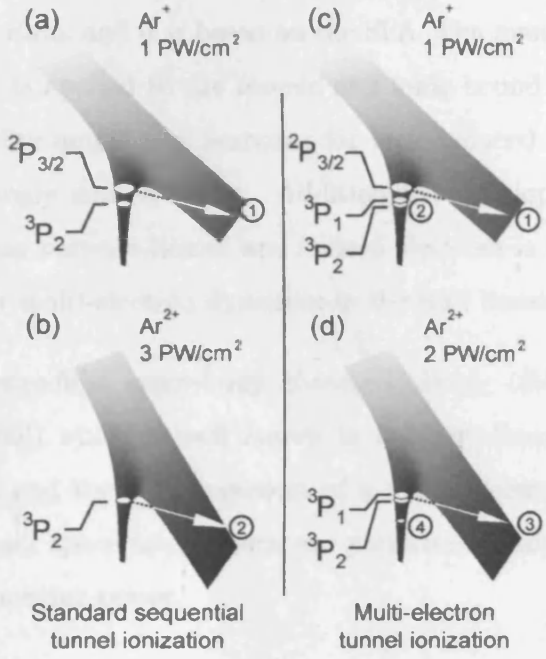

Figure 6.1: Tunnel ionisation and resulting excitation mechanisms in the Coulomb potential of argon. Normal sequential tunnel ionisation: a) At an intensity of 1 PWcm^{-2} the ground state ($^2P_{3/2}$) of Ar^+ has a significant probability to tunnel ionise (1). b) As the intensity is increased to 3 PWcm^{-2}, the ground state ($^3P_2$) of Ar^{2+} can ionise (2). When multi-electron processes are considered, tunnel ionisation is significantly influenced by excitation. c) As the $^2P_{3/2}$ electron tunnels from the Ar^+ ion (1), a significant population is transferred from the $^3P_2$ to the $^3P_1$ excited state in the Ar^{2+} ion (2). d) A lower intensity (2 PWcm^{-2}) is then required to ionise the population in the $^3P_1$ state (3), whereas the $^3P_2$ state ionises at 3 PWcm^{-2}) as shown in b). The generation of Ar^{2+} can then further excite the Ar^{3+} ion (4). We measure the dependence of the probability of ionisation on the laser intensity and charge state. From [Bryan et al., 2006c].

solutions, but even with these, calculations for more than two active electrons become extremely large. The theoretical methods other than tunnelling equations used to calculate multi-electron dynamics are reviewed briefly here.

A recent study [Fabian et al., 2003] starts with the 3-dimensional Schrodinger equation for many electron atoms and ions in the dipole approximation. The atom is assumed to be initially in the ground state, and it is based on the SFA. The main feature of this method is that full correlation is applied to the atomic and ionic bound states: the equation of motion of the probability amplitudes accounts for laser-induced transitions between the bound states of the singly ionised target. Additionally, the population transfer due to the Coulomb interaction between bound and ionised electrons is included. However, this theory is calculated for multi-electron dynamics in the field ionisation regime.

An alternative is intense-field many-body S-matrix theory (IMST) (for a review see [Becker and Faisal, 2005]) which is well known in collision theory. This calculates the Coulombic interaction and the rearrangement of a many electron system in an intense field. The 6-dimensional space integrations are performed analytically, so this method also requires large computing power.

6.1.3 Tunnelling Theory to Calculate METI

A simpler alternative to the *ab initio* calculations is provided by the tunnelling equation based on Keldysh theory (Chapter 1). This has been used by [Litvinyuk et al., 2005] and [Kornev et al., 2003] to describe multi-electron dynamics during tunnel ionisation. Calculations using molecular ADK theory and experimental results for METI were presented by [Litvinyuk et al., 2005] for the molecule D_2. Here we present the first results for atomic excitation in Ar and Kr during METI.

Tunnelling theory is commonly used to describe single ionisation in the tunnel regime within the SAE. where only the outermost electron interacts with the laser field and electron-electron interaction is assumed to be negligible. However, the tunnelling equation provides a convenient and straightforward formula to calculate the atomic ionisation rate

in both linearly and circularly polarised laser fields, which can be extended to include more than one electron and subsequent factors such as inelastic tunnelling. This extension of Keldysh's tunnelling theory is described here. The theoretical calculations in this chapter have been performed by Kornev and compared with our experimental results obtained using the ASTRA Laser Facility.

6.1.4 Modifications to Tunnelling Theory

Presented here is a brief summary of Kornev's theoretical predictions [Kornev et al., 2003], which is shown for completeness and to put our experimental work into context. Standard tunnelling theory provides a reasonable description of singly charged ions created by the tunnel ionisation of an electron in the ground state. It is therefore the starting point for the calculations of Kornev to describe the creation of multicharged ions accompanied by core excitation during tunnel ionisation. As tunnel ionisation of electrons from excited states (as well as the ground state) is considered, the theory has been extended to include the tunnel ionisation of N electrons.

A constant $C_{\nu l}$ describes the behaviour of the asymptotic electron wave function if N equivalent electrons are removed from an atom via tunnelling. In the quasiclassical approximation this is given by:

$$C_{\nu l} = (2\pi\nu)^{-1/2}(2/\nu)^{\nu}\left(\frac{1-\varepsilon}{1+\varepsilon}\right)^{(l+1/2)/2}\left(1-\varepsilon^2\right)^{-\nu/2} \tag{6.1}$$

where ν is the principal quantum number calculated below, and l refers to the orbital angular momentum. Here $\varepsilon = (l+1/2)/\nu$ corresponds to the eccentricity of the classical elliptic orbit of the electron ($\varepsilon < 1$). The effective principal quantum number ν depends on the binding energy of the emitted electron E_b as:

$$\nu = \left(NZ^2e^2/2aE_b^{(N)}\right)^{1/2} \tag{6.2}$$

where e is the electron charge, $a = \hbar^2/m_e e^2$ is the Bohr radius and Z is the residual ion charge.

The tunnelling theory is limited to small values of the Keldysh parameter γ corresponding to the tunnelling regime ($\gamma < 1$), which is discussed in Chapter 1. The N electron Keldysh parameter is given by:

$$\gamma_N = \frac{\sqrt{2m_e E_b^{(N)}}/N}{eF}\omega < 1 \tag{6.3}$$

where ω is the laser frequency and F is the strength of the laser field. The electric field of the atomic core F_a is given by:

$$F_a = \frac{e}{a^2}\left(\frac{Z}{\nu}\right)^3 \tag{6.4}$$

Modification of the tunnelling theory is required to account for the excitation of the ion after an electron is tunnel ionised. As it is similar to inelastic scattering, this process is termed inelastic tunnelling.

The tunnel ionisation of a number of equivalent electrons, occurring over one half cycle of the light field can be incorporated into the theory. The N electron tunnelling rate in a linearly polarised laser field is given by this equation:

$$\begin{aligned} W_{Nlin}^{(nl\{m\})} = & \frac{\sqrt{3\pi}\hbar}{a^2 m_e}\frac{M!(2l+1)^N C_{\nu l}^{2N}}{2^{M-3/2}N^{M+3/2}}Q^2\left(\frac{Z}{\nu}\right)^{3N-1} \\ & \times \prod_{j=1}^{N}\frac{(l+|m_j|)!}{(|m_j|!)^2(l-|m_j|)!}\left(\frac{2F_a}{F}\right)^{2N(\nu-1)-M+1/2} \\ & \times \exp\left(-\frac{2NF_a}{3F}\right) \end{aligned} \tag{6.5}$$

Q is the overlap integral between the wave functions of the electrons in their initial states of the atom or ion with the wave functions in the excited ionic state, and is calculated in Appendix B of [Kornev et al., 2003]. The index $\{M\}$ refers to the set of magnetic quantum numbers of the tunnelling electrons $m_1, m_2, \ldots, m_N$ such that:

$$M = \sum_{j=1}^{N}|m_j|\,. \tag{6.6}$$

The validity of equation 6.5 is determined by the Keldysh parameter given in equation 6.3.

In the case of circular polarisation a limitation of the tunnelling theory becomes evident as it was assumed that the rate of tunnelling in the circularly polarised field is the same as in the linear field [Perelomov et al., 1966]. Although the absolute value of the electric field has no time dependence in the circular case, the rate of tunnelling depends on the magnetic quantum number of the tunnelling electron. Therefore, in the circularly polarised field the projection of electron angular momentum is conserved in the direction of light wave propagation only, and not in the direction of the electric field which is time dependent.

This dependence of the tunnelling rate on the electric field for circular polarisation can be incorporated into ADK theory. In the dipole approximation, the electric field $F(t)$ of the circularly polarised light wave propagating along the z-axis is given by:

$$F(t) = F\left(e_x \cos\omega t + \eta e_y \sin\omega t\right) \tag{6.7}$$

where $e_{x,y}$ are unit vectors along the respective axes, and $\eta = \pm 1$ for right (left) circular polarisation. The electron-field interaction V is given by:

$$V = e\mathbf{r}\mathbf{F} = erF\sin\theta\cos(\varphi - \eta\omega t) \tag{6.8}$$

where θ, φ are the polar and azimuthal angles of the vector $\mathbf{r}$.

An expression to connect the N-electron tunnelling rates (where D represents the electron wave function) in a linearly or circularly polarised laser field is given by:

$$\begin{aligned} W^{(nl\{m\})}_{Ncirc} = \; & (\pi F_a/3F)^{1/2} \textstyle\sum_{m'_1,\ldots,m'_N} \left| D^l_{m'_1 m_1}(0,\pi/2,0)\ldots \right. \\ & \left. \times\, D^l_{m'_N m_N}(0,\pi/2,0)\right|^4 W^{(nl\{m'\})}_{Nlin}. \end{aligned} \tag{6.9}$$

The kinetics of multicharged ion formation were also considered. This means that all possible ionisation channels from ground and excited states are included in the calculation. Kinetic equations describe this as multichannel multi-cascaded reactions, including both single electron and multielectron cascading transitions. Ionisation processes accompanied by excitation of atomic and ionic cores are incorporated. The number of cascading channels

increases significantly as the charge state of the ion increases. A table of the ionisation and excitation energies of Ar^{X+} and Kr^{X+} ions are show in Table 6.1. Only the lowest and therefore the most easily accessible excited states are included in the calculation to comply with the sudden approximation.

X	Outer	subshell	Ar	Kr
0	p^6	$^1S_0$	0.0	0.0
1	p^5	$^2P_{3/2}$	127109.8	112914.4
		$^2P_{1/2}$	1431.5831	5370.10
2	p^4	$^3P_2$	222848.2	196475.4
		$^3P_1$	1112.175	4584.4
		$^3P_0$	1570.229	5312.9
		$^1D_2$	14010.004	14644.3
		$^1S_0$	33265.724	33079.6
3	p^3	$^4S_{3/2}$	328550.0	298020.0
		$^2D_{3/2}$	21090.4	17036.8
		$^2D_{5/2}$	21219.3	18699.9
		$^2P_{1/2}$	34855.5	31055.2
		$^2P_{3/2}$	35032.6	33404.9
4	p^2	$^3P_0$	481400.0	423400.0
		$^3P_1$	765.23	3742.86
		$^3P_2$	2028.80	7595.34
		$^1D_2$	16298.9	19722.93
		$^1S_0$	37912.0	39203.92
5	p^1	$^2P_{1/2}$	606000.0	521800.0
		$^2P_{3/2}$	2207.1	8108.0
6	p^0	$^1S_0$	734000.0	633100.0

Table 6.1: Ionisation and excitation energies (in cm^{-1}) of Ar^{X+} and Kr^{X+} ions (X = 1 to 6) taken from the NIST database. Only the lowest excited states are shown, as these are valid for the present experiment, although many more excited states exist. From [Kornev et al., 2003].

A ratio of the concentration of ions in one state n_f to the initial concentration of neutral atoms n_{tot} is defined as:

$$C_f = n_f/n_{tot}, \quad n_{tot} = \sum_{f=0}^{f_{tot}} n_f \tag{6.10}$$

The emitted electrons may have different values of the magnetic quantum number m_q, which increases the number of ways in which the multiple atomic ionisation process can occur. The kinetic equations used are those given in [Fittinghoff et al., 1992] and [Kulander et al., 1995] and assume that the laser pulse contains at least three optical cy-

cles. This condition is fully satisfied for the experimental results obtained by our research group.

6.1.5 Theoretical Results

The result of applying the equations described above to the case of argon atoms in a circularly polarised laser field are shown in this section, published in [Kornev et al., 2003]. In Figure 6.2, the concentration of ions Ar^{X+} in each charge state as a fraction of the total number of Ar atoms is calculated for a pulse duration of 50fs. Two sets of results are displayed: the solid lines include all valid METI channels as described in the previous section, including all the possible excited states given in Table 6.1, and the dotted lines show only sequential single-electron ionisation from the ionic ground states (pure tunnelling theory without modification).

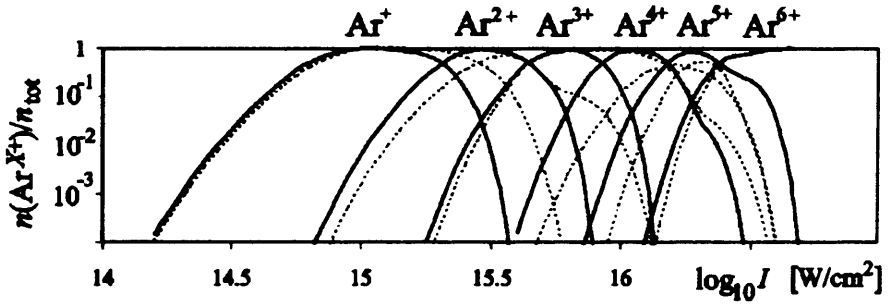

Figure 6.2: Concentration of multiply charged Ar ions $n(Ar^{X+})$ up to Ar^{6+} as a function of intensity. Results are obtained for a circularly polarised laser pulse of 50fs duration without including the focal geometry. n_{tot} is the initial concentration of neutral atoms. Solid lines include all ionisation channels, while dotted lines are calculated from the ground state only using pure tunnelling theory. Figure taken from [Kornev et al., 2003].

A significant difference can be seen between the two sets of results, especially for the higher charge states. It can be seen that both of the calculated concentrations of Ar^{+} ions have a similar magnitude on the rising edge as no excitation will be present here. However, for the higher charge states Ar^{2+} to Ar^{5+} a significant difference appears between the ground state calculations and those including the excited states. This illustrates the importance of taking the excited states (inelastic tunnelling) into account for studies of atomic tunnel ionisation.

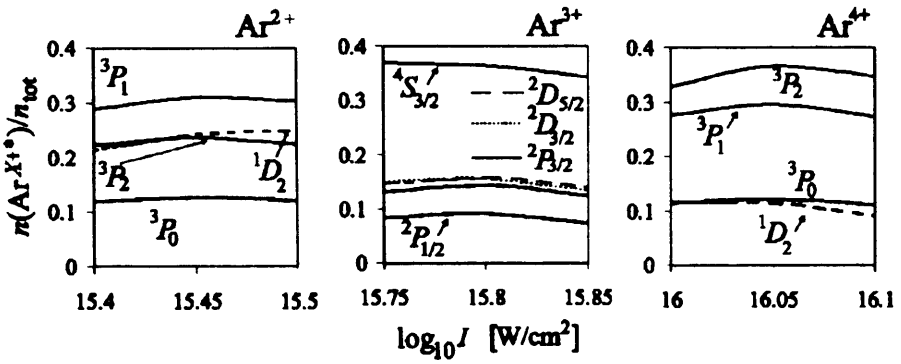

Figure 6.3: Populations of ground and excited states of ions Ar^{2+} to Ar^{4+} as a function of intensity for a 50fs circularly polarised laser pulse. Figure taken from [Kornev et al., 2003].

Ground and excited state populations of Ar^{2+}, Ar^{3+} and Ar^{4+} ions as a function of laser intensity as presented by [Kornev et al., 2003] are shown in Figure 6.3. It can be seen that the population of the Ar^{2+} ground state $^3P_2$ is similar to that of the excited state $^1D_2$. Contributions to the ionisation of Ar^{2+} from this state would be expected. The populations of ground and excited states for Ar^{3+} are also comparable, while some Ar^{4+} excited state populations are greater than the ground state population. This presents a clear case for the inclusion of excited states when calculating tunnel ionisation rates.

Theoretical results for krypton were also published in [Kornev et al., 2003], and are shown here in Figure 6.4 and Figure 6.5. The concentrations of each charge state in Figure 6.4 reach a maximum at a slightly lower laser intensity than for argon due to its lower ionisation potential, but otherwise exhibit the significant difference between the results for all METI channels and the results for the pure ground state calculation as seen for argon. It can be seen from Figure 6.5 that the excited state populations of krypton charge states are comparable with the ground state populations for Kr^{4+}, Kr^{2+} and Kr^{3+}.

Argon and krypton are ideal targets for observing METI as they have a low excitation energy ($\leq$4eV) so there is an increased effect of inelastic tunnelling during ionisation. For ions with high excitation energy such as those of helium, the effect of inelastic tunnelling is decreased.

These theoretical results obtained by Kornev demonstrate the significance of inelastic

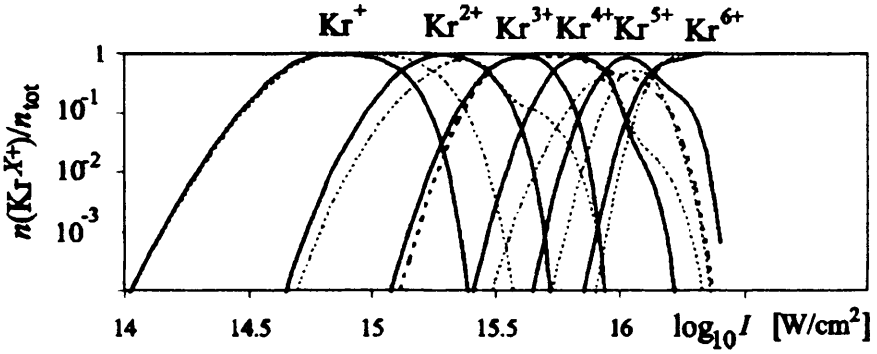

Figure 6.4: Concentration of multiply charged Kr ions $n(\mathrm{Kr}^{X+})$ up to Kr^{6+} as a function of intensity for the same conditions as Figure 6.2. Solid lines include all ionisation channels, while dotted lines are calculated from the pure tunnelling theory. Figure taken from [Kornev et al., 2003].

tunnelling during the creation of multiply charged ions. Experimental results were required to verify this theoretically predicted atomic excitation process, which have been performed for the first time by our research group [Bryan et al., 2006c] and form the subject of this Chapter.

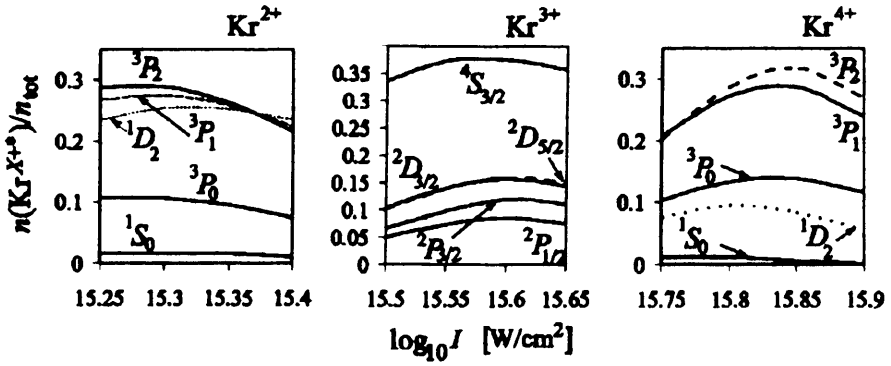

Figure 6.5: Populations of ground and excited states of ions Kr^{2+} to Kr^{4+} as a function of intensity for a 50fs circularly polarised laser pulse. Figure taken from [Kornev et al., 2003].

6.2 Experimental Procedure

The ASTRA Laser Facility at RAL described in Chapter 3 was used for these experiments. The 10 Hz beam producing 40fs pulses at 790nm is focused using a $f/11$ lens to generate

a peak intensity of $8\times10^{16}\mathrm{Wcm}^{-2}$ in the interaction region of a time-of-flight mass spectrometer (described in Chapter 4). Laser polarisation was made circular by inserting a quarter-wave plate into the path of the linearly polarised beam. The intensity selective scanning (ISS) technique was used (Chapter 5), whereby the lens position is moved along the direction of laser propagation and a limiting aperture in the spectrometer exposes only a small slice of the focal volume to the detector. By translating the lens in 125μm steps an ISS scan of the relative ion yields of Kr^{X+} and Ar^{X+} (X = 1 to 6) have been measured.

The polarisation of the laser field is important in this experiment. If linear polarisation were used, recollision effects would alter the ionisation rates and this would have to be incorporated into the theory. As recollision ionisation is a complex process, highly dependent on the pulse intensity and the charge state of the ion, it is simpler to remove it from the experiment altogether. Recollision effects are also orders of magnitude greater than shake-up excitation, and could therefore mask the smaller effect of shake-up excitation. Following tunnel ionisation, the free electron is driven by the electric field. If the field is linearly polarised, the electron may be driven back along its path when the field changes sign and return to the core to cause further ionisation (recollision). A circularly polarised field will drive the electron on a spiral path, removing it from the ion and preventing recollision. Therefore the use of a circularly polarised laser field in our experiments prevents any recollision ionisation occurring, allowing the smaller but still significant effects of shake up to be observed.

In order to compare these results directly with theoretical predictions, the spatial integration over intensity in each slice of the laser focus is removed through an intensity deconvolution technique [Walker et al., 1998] which relies on a knowledge of the laser intensity distribution. In a new advancement on this technique by our research group [Bryan et al., 2006b], any diffraction of the laser beam is also calculated by solving the Huygens-Fresnel diffraction integral and removed from the results (Chapter 5).

6.3 Results

The experimental results obtained using the apparatus described above have been compared to the theoretical predictions of [Kornev et al., 2003]. The combination of experimental techniques allows the tunnel ionisation probability of argon and krypton to be measured accurately, independently of the focal geometry.

6.3.1 Intensity Selective Scan Measurements

Raw intensity selective scan (ISS) data for krypton taken using circularly polarised 40fs laser pulses is presented here in Figure 6.6. The data is presented as a 3-D plot with scanning lens position along the x-axis and time-of-flight along the y-axis. The ion yield is shown as a colour scale in z in which at least six charged states are observed. A 2000 laser shot average is used to record the ion yield at each distance from the focus. Kr gas pressure is kept low ($\approx 3\times10^{-8}$bar) to avoid space charge effects which would be apparent as a significant spread in the flight time of each charge state.

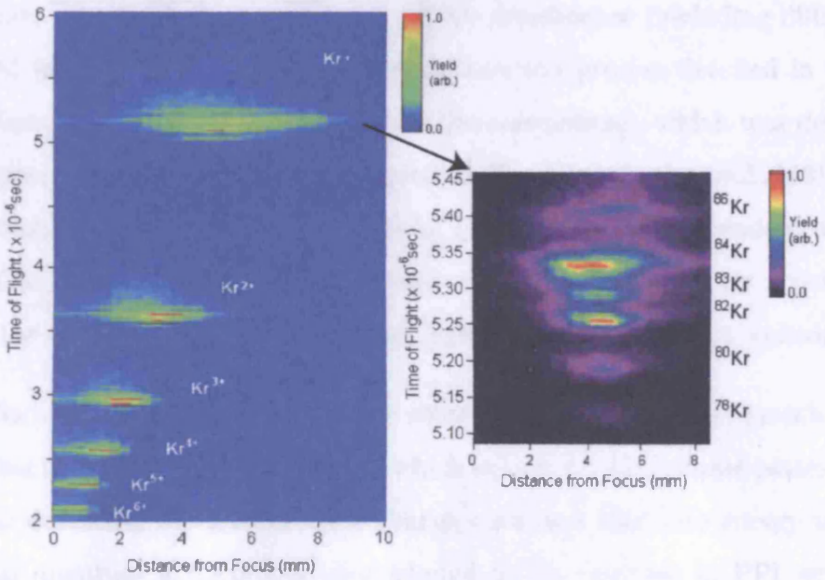

Figure 6.6: ISS data for the first six charge states of krypton generated in the TOFMS using focused 40fs 800nm laser pulses. The Kr^+ charge state is shown in detail on the right. The six main isotopes of krypton can be identified from this ISS data.

The six main isotopes of Kr are resolved in the ISS data, also shown in Figure 6.6. These isotopes are ^{78}Kr, ^{80}Kr, ^{82}Kr, ^{83}Kr, ^{84}Kr and ^{86}Kr with natural abundances of 0.35%, 2.28%, 11.58%, 11.49%, 57.00% and 17.30% respectively. Also, some degeneracy may occur with background contaminants, for example $^{84}Kr^{3+}$ is degenerate with N_2^+ which has a much lower ionisation threshold. Therefore, only the non-degenerate isotopes (78, 80, 82 and 86) are integrated with respect to flight time for this experiment.

Raw ISS data for argon is shown in the next section (Figure 6.7). There are only three naturally occurring isotopes of argon, ^{36}Ar, ^{38}Ar, and ^{40}Ar, with natural abundances of 0.33%, 0.06% and 99.60% respectively, which have no significant degeneracy with atmospheric contaminants.

6.3.2 Measured Probability of Ionisation

In order to make a direct comparison with the theory, the non-Gaussian intensity deconvolution described in Chapter 5 is applied to the ISS data. A schematic of this process is given in Figure 6.7. First, an integration over the time-of-flight for a single charge state is performed. Next, the known confocal volume dependence (including diffraction effects) is removed from the data through the deconvolution process detailed in Chapter 5. A beam radius (ω_g) of 10.25mm was used in the calculations, which was determined from a measurement of the unfocused beam profile. The result is the probability of ionisation of a particular charge state as a function of laser intensity, independent of focal volume effects. This is called the partial probability of ionisation (PPI) for a particular charge state, as the deconvolution method is only valid at intensities below saturation.

The results of the PPI curves for Kr are shown in Figure 6.8. The quantum efficiency of the detector is present in these results, which occurs as the channel plates become more efficient at detecting the ions as their charge state and therefore energy increases. This increase in quantum efficiency is proportional to the increase in PPI with which each charge state of Kr saturates relative to the Kr^+ saturation at unity.

The quantum efficiency has been removed from the results for Ar in Figure 6.9, and the

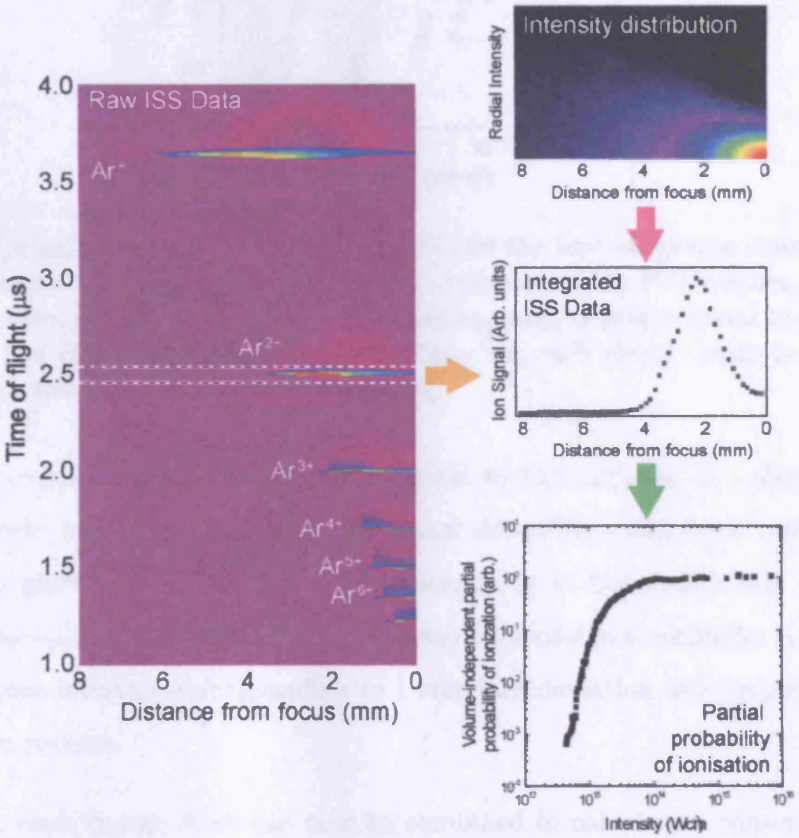

Figure 6.7: ISS data for the charge states of argon (left) produced by 40fs laser pulses in the TOFMS. The data is integrated over a single charge state and an intensity deconvolution is applied. This results in a partial probability of ionisation signal as a function of intensity, with all confocal volume effects removed.

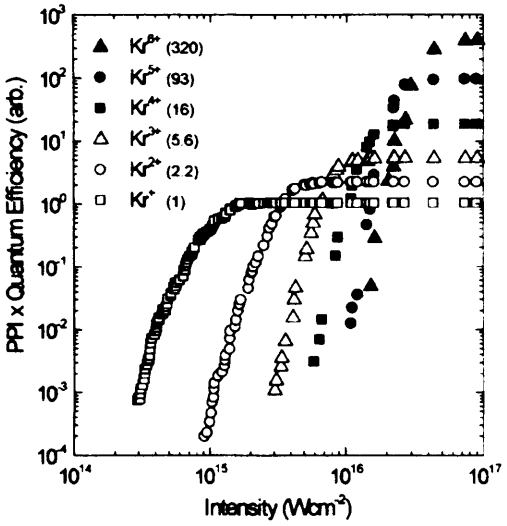

Figure 6.8: Partial probability of ionisation (PPI) for the first six charge states of krypton, recovered from the ISS scan in Figure 6.6. The point at which PPI reaches saturation in each charge state, relative to the Kr^+ saturation at unity, is proportional to the quantum efficiency of the detector. The relative efficiency for each charge state is given in the legend. Figure taken from [Bryan et al., 2006d].

PPI now saturates at unity. It is now equivalent to the response of a single atom to a spatially infinite laser focus, as all instrumental dependence has been removed. Error bars are also plotted on Figure 6.9. The uncertainty in the results was estimated by calculating the statistical deviation in the average time-of-flight results for Ar. Upper and lower confidence intervals corresponding to 1 standard deviation were applied during the deconvolution process.

The PPIs for each charge state can now be combined to calculate a conserved probability of ionisation (CPI), which includes all ionisation states (Figure 6.10). The PPI for Ar^+ in Figure 6.9 is small at low intensity, increasing up to saturation at an intensity of 10^{15}Wcm^{-2}. However, at this intensity the PPI for Ar^{2+} is non-zero. In order to conserve the probability of ionisation, the sum of probabilities must be less than unity below the saturation intensity for Ar^+ or equal to unity above it. Therefore probability is conserved by subtraction of Ar^{2+} PPI from Ar^+ PPI. Probability is conserved throughout the experiment by repeating this subtraction for all charge states (Figure 6.10(c)).

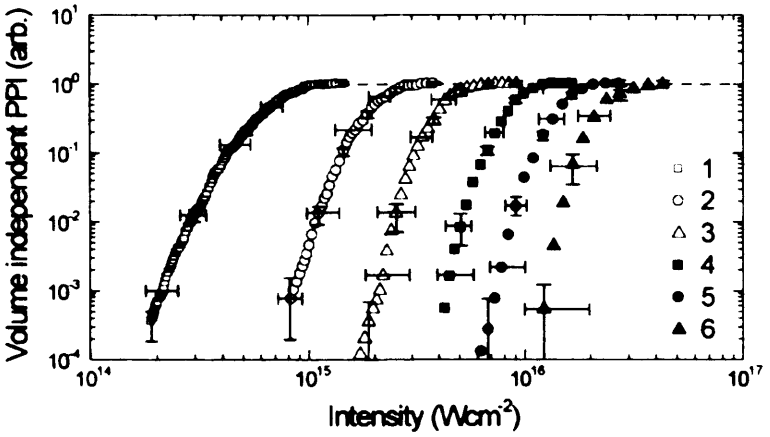

Figure 6.9: PPI for the first six charge states of argon, recovered from the ISS scan in Figure 6.7. The effect of detector quantum efficiency has been removed from the results so that the PPI for all charge states saturates at unity (dotted line). Points above saturation are not shown as the deconvolution method is only valid for points below saturation. Error bars show the experimental uncertainty. Figure adapted from [Bryan et al., 2006c].

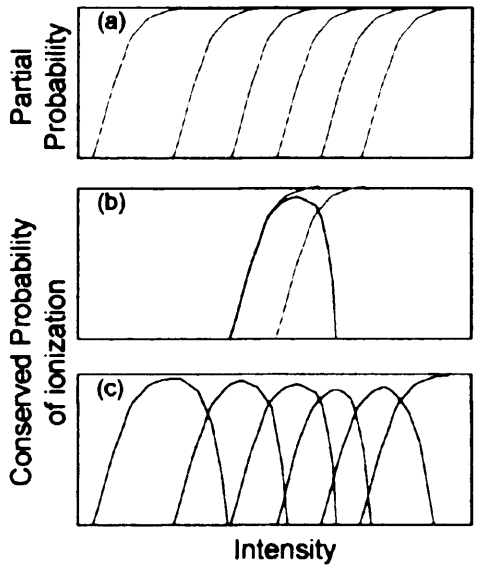

Figure 6.10: Diagram to show probability conservation; results are converted from PPI (red) to CPI (blue). (a) All partial probabilities are normalised to unity. (b) To conserve Ar^{X+}, the PPI of $Ar^{(X+1)+}$ is subtracted from the PPI of Ar^{X+}, resulting in the blue CPI curve. (c) The process is repeated for all charge states, resulting in a series of conserved probabilities of ionisation (CPI) for Ar^{X+} where $X = 1$ to 6.

6.3.3 Comparison with Theoretical Predictions

The experimental CPI results can now be directly compared with the theoretical calculations of Kornev (METI). This is shown in Figure 6.11 for Kr and Figure 6.12 for Ar. In both figures the theoretical results for tunnelling theory (thin lines) accounting only for ground state tunnel ionisation are shown as well as METI (thick lines) which includes contributions from shake up, the theory of which was described in the previous section. These are compared with the experimental data (points). The experimental data has been normalised in intensity to the point of Kr^{+} saturation in the theoretical results.

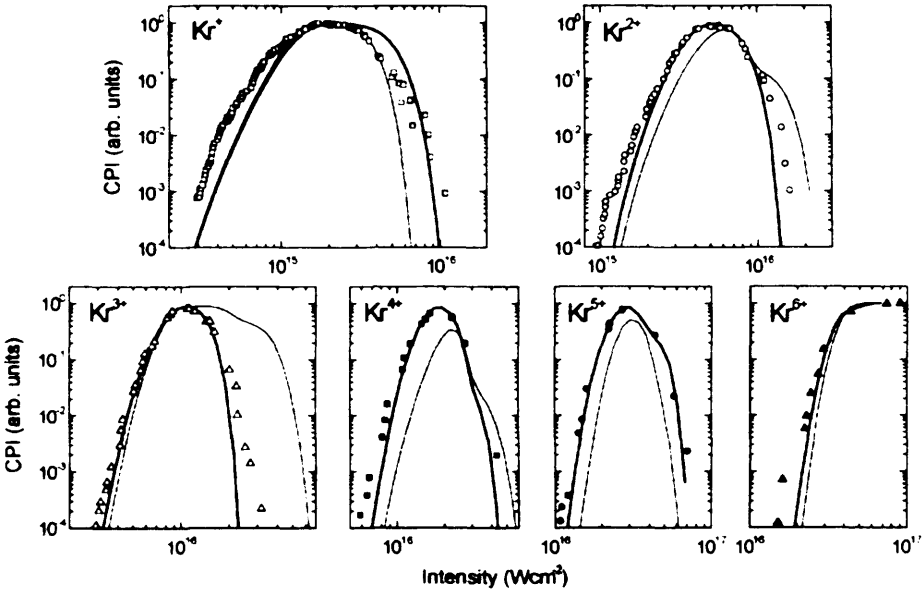

Figure 6.11: Conserved probability of ionisation (CPI) to Kr^{X+} (X =1 to 6) for a 40fs circularly polarised laser pulse. All optical and geometrical dependency has been removed to allow direct comparison with the theoretical predictions of [Kornev et al., 2003]. In all frames, the thin line is the sequential tunnel ionisation from the ground state prediction (ADK theory), and the thick line is the multi-electron tunnel ionisation (METI) prediction including excitation to lower lying states. Figure taken from [Bryan et al., 2006d].

The difference between theory and experiment when only sequential tunnel ionisation from the ground state is considered (thin line) can be seen clearly in both Figures 6.11 for Kr and 6.12 for Ar. In Figure 6.11, the rising edge of the first charge state of Kr does not fit either theory curve. This is due to additional multiphoton ionisation (MPI) occurring at lower intensities in the perturbative regime, which is not incorporated into the theory. At intensities close to the saturation point of Kr^{+} both theory curves provide a good fit to the

data. This is as expected, because in this region of intensity the results should be purely from tunnel ionisation, with no excitation effects as this curve is for single ionisation. A smaller discrepancy at low intensity between experimental and both theoretical results is observed in the Kr^{2+} data (Figure 6.11) around $10^{15}Wcm^{-2}$, also attributed to MPI. As the intensity increases, the METI curve is in much better agreement with the Kr^{2+} experimental data, indicating that excitation effects are lowering the intensity required for ionisation by a measurable amount from that predicted by the tunnelling theory curve.

A much improved fit to the experimental data is observed with METI over tunnelling theory for Kr^{3+}, Kr^{4+} and Kr^{5+} over the entire intensity range. It can be seen that tunnelling theory underestimates the CPI of Kr^{4+} by more than an order of magnitude at an intensity of $10^{16}Wcm^{2}$. At the highest intensities in this experiment where Kr^{6+} is observed, a good agreement is obtained for both theoretical curves, although the METI fit is still slightly better.

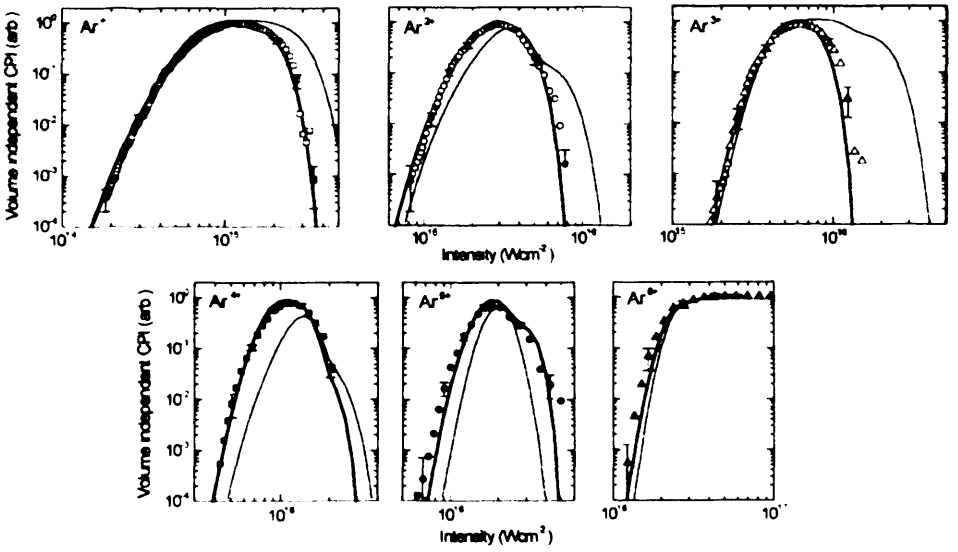

Figure 6.12: Conserved probability of ionisation (CPI) to Ar^{n+} (n=1 to 6) for a 40fs circularly polarised laser pulse. All optical and geometrical dependency has been removed to allow direct comparison with the theoretical predictions of [Kornev et al., 2003]. In all frames, the thin line is the sequential tunnel ionisation from the ground state prediction (tunnelling theory), and the thick line is the multi-electron tunnel ionisation (METI) prediction including excitation to lower lying states. Error bars are included to show the experimental uncertainty. Figure taken from [Bryan et al., 2006c].

In Figure 6.12 for Ar, there is a marked improvement of the METI predictions over the

tunnelling theory curves. The tunnelling theoretical prediction lies outside the calculated experimental error bars for most of the charge states. A good fit to both theory curves is observed for Ar^{+} experimental data at intensities below saturation as there is no influence of excitation. However, as the intensity increases beyond saturation for Ar^{+} the METI curve matches the experiment far more accurately than the tunnelling theory curve. The METI curves continue to demonstrate a much improved fit to the experimental results than that of the tunnelling theory curves for all the charge states of Ar.

Throughout the results presented in Figures 6.11 and 6.12 the METI calculations have provided an excellent quantification of the experimentally obtained CPI data generated by 40fs circularly polarised laser pulses. This is due to the inclusion of excitation of the bound valence electrons in the atomic ion in the tunnelling theory calculations. The shake-up process can only cause excitation at high laser intensities, as the departing electron must have enough energy to excite the remaining bound electrons [Eichmann et al., 2000]. This view is consistent with the present results as no significant excitation is observed until the laser intensity reaches $10^{15}\mathrm{Wcm}^{-2}$. It is predicted that the contribution of shake-up to the ionisation yield is many orders of magnitude lower than that of recollision [Eichmann et al., 2000], however through the removal of recollision by the use of circularly polarised laser pulses the smaller effect of shake-up excitation has been quantified in this experiment. This observation would not have been possible without the geometry-independent intensity deconvolution technique to generate conserved ionisation probabilities.

6.3.4 Excitation in Previous Experiments

In order to demonstrate why the effect of excitation during tunnel ionisation has not been observed previously, a brief review of other experimental results using circular polarisation is presented. The most important reason why excitation has not been observed in these studies is that it is a relatively small effect which may be masked by the presence of focal volume effects. The point is that the present non-Gaussian deconvolution method has been instrumental in this first experimental observation of atomic excitation during

tunnel ionisation.

As very few other comparable studies have been made using circularly polarised light, this review does not present a conclusive result. However, an attempt is made to explain the discrepancies between experiment and theory in these previous studies in light of the present results. The ion yield as a function of laser intensity (containing focal volume effects) and the corresponding tunnelling calculations from three such previous studies are analysed. Although not directly comparable with the results obtained in this chapter due to differences in experimental apparatus or pulse duration, intensity or wavelength they illustrate the shortcomings of a tunnelling theory that only considers ionisation from the ground state.

To illustrate the advantage of the ability to remove all focal volume effects, the experimental results obtained in the present study have been scaled to include the entire focal volume of the laser. It is now comparable with the calculations of Kornev in the latter section of [Kornev et al., 2003] that have been spatially averaged over the focal volume. The experiment is compared to the volume-scaled results for tunnelling theory (thin lines) and METI theory (thick lines) in Figure 6.13.

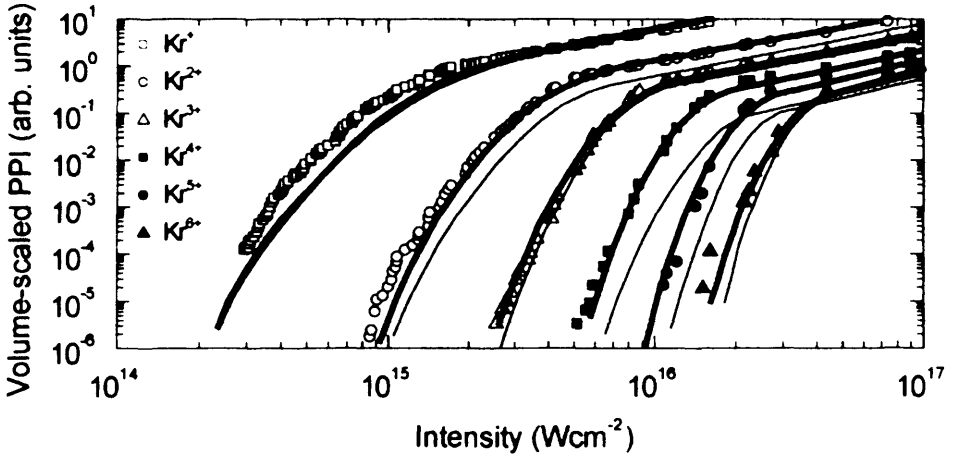

Figure 6.13: Volume-scaled partial probability of ionisation to Kr^{X+} ($X = 1$ to 6) for a 40fs circularly polarised laser pulse (points). This is compared to the volume-scaled predictions of [Kornev et al., 2003] to show how ionisation-induced excitation could be difficult to identify from standard intensity variation measurements. Thin lines - tunnelling theory, thick lines - METI. Figure taken from [Bryan et al., 2006d].

It is now far more difficult to observe which model provides the best fit, especially above saturation intensities. The change in volume within the laser focus can mask the difference between ground state only tunnelling and METI calculations. Excitation can be observed as a vertical shift in the apparent yield, with further small variations in the intensity. This difference between experimental results and tunnelling theory could be misinterpreted, for example as detector efficiency, or it could be overlooked when the experimental results are normalised to the theory. This demonstrates the importance of an accurate deconvolution process to these results, as it permits the resolution of these less obvious, but important METI features.

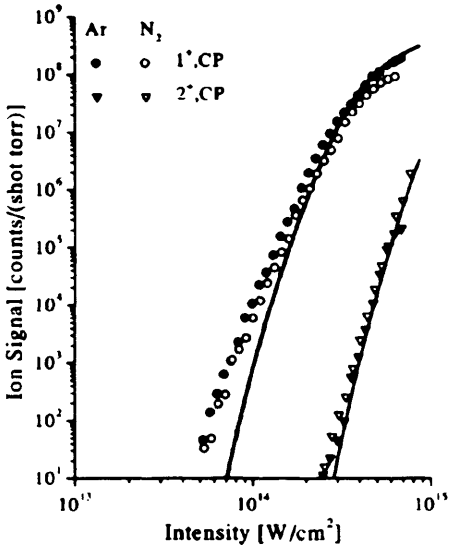

Figure 6.14: Single and double ionisation yields for N_2 and Ar using circular polarisation (CP). Pulse duration was 30fs and wavelength was 800nm. Tunnelling calculations are shown by the full curves. Figure adapted from [Guo et al., 1998].

A previous study of single and double ionisation of argon using circularly polarised 30fs laser pulses has been performed by [Guo et al., 1998]. As an intensity variation method with an apertured detector is utilised here to collect the TOF data, the results are not directly comparable with the METI calculations of Kornev - the results cannot be averaged over the entire focal volume to give the usual $I^{3/2}$ dependence in the saturation region. Nor has all spatial dependence of the focal volume been removed, which would allow for a direct comparison with theory. In Figure 6.14 results for N_2 are compared in this work as the ionisation potentials are very similar to Ar for single ionisation (Ar, 15.76eV; N_2,

15.58eV) and double ionisation (Ar, 27.63eV; N_2, 27.12eV), although this is not relevant to the present discussion.

In order to calibrate the intensity in [Guo et al., 1998], the Ar^+ ion yield from linear polarisation was matched to the tunnelling equation (ADK). This agreed with the absolute intensity calculated from the beam spot size, pulse duration and pulse energy to within a factor of 2. The tunnelling rate was obtained by integrating over the measured pulse duration and focal volume. The tunnelling theory appears to match the data well for the Ar^{2+} curve although only the lower intensity part ($\leq 10^{15}$Wcm^2) is shown. It does not fit the low intensity part of the Ar^+ data. which may be because of multiphoton effects. If more results were available, or if an accurate deconvolution method had been applied it may have been possible to detect a difference due to METI effects. However, the fact that an aperture was used would prevent a direct comparison with Kornev's theory, as the number of detected ions averaged over the entire pulse is required.

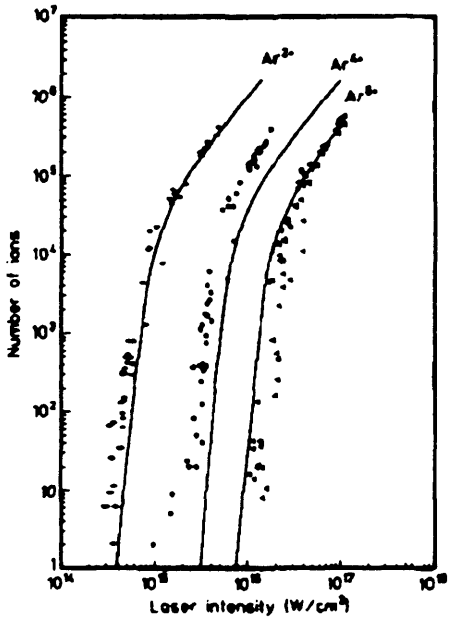

Figure 6.15: Plot showing the absolute number of Ar^{2+}, Ar^{4+} and Ar^{6+} ions produced as a function of peak laser intensity. Circularly polarised laser pulses of 1ps duration 1053nm wavelength were used for this study. Figure taken from [Auguste et al., 1992].

A second study of multiple ionisation also in Ar has been published by [Auguste et al., 1992] shown in Figure 6.15. Although this data is performed using the entire laser focal volume,

the pulse duration of 1ps and wavelength of 1053nm means that these results are not directly comparable either. However, the charge states Ar^{2+}, Ar^{4+} and Ar^{6+} are shown along with tunnelling theory calculations. The experimental data is shifted by a factor of 1.3 in the intensity scale to fit the theory.

The Ar^{2+} tunnelling theory calculations underestimate the ion yield at low intensities. This could be evidence of METI occurring below the saturation intensity, but above saturation the tunnelling calculation appears to fit the data well. In the Ar^{4+} data, the difference between theory and experiment is clearly evident for the full intensity range. This supports the prediction that tunnelling theory underestimates the ion yield; by including ionisation channels from all possible excited states in the calculation, a more accurate fit to the experiment should be obtained. Full removal of all focal volume effects would permit a more conclusive comparison with the METI calculation. For the Ar^{6+} the fit between experiment and theory is very good above saturation, but below saturation the tunnelling theory now overestimates the observed ion yield. The reason for this is not clear, although for this charge state the tunnel and METI calculations in Figure 6.13 are quite similar, especially above saturation so it would be difficult to observe METI effects in this curve in any case.

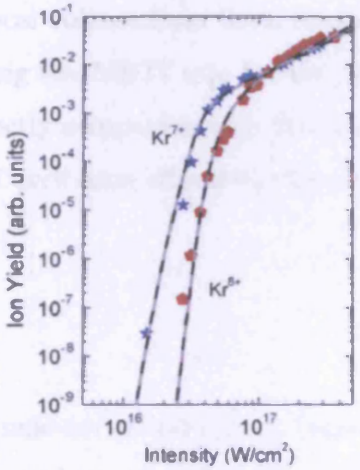

Figure 6.16: Intensity dependent ion yields for Kr^{7+} and Kr^{8+}. Experimental data points are compared with tunnelling calculation curves for circular polarisation. Figure taken from [Gubbini et al., 2006].

The third study, which is of ionisation in krypton using circularly polarised laser pulses, is from a paper by [Gubbini et al., 2006]. This study is performed using 40fs pulses at 815nm but it is at a much higher intensity than the present study, obtaining experimental data for charge states up to Kr^{13+} where relativistic effects have a significant influence. Their results for Kr^{7+} and Kr^{8+} are shown here in Figure 6.16, compared with tunnelling theory calculations. The experimental data has been shifted by a factor of 1.3 in intensity.

A good fit between theory and experiment is observed for Kr^{7+} across the full intensity range. A reasonable fit for Kr^{8+} is also observed below saturation, however above saturation the tunnelling calculation appears to slightly underestimate the ionisation rate. As the predictions given by Kornev do not extend up to these higher charge states, it is purely speculative to attribute this slight discrepancy to METI. Again, removal of the focal volume would be necessary to observe any effects due to shake-up excitation conclusively.

This brief examination of other experimental work on intensity dependent ionisation yields demonstrates how excitation effects have been overlooked in previous studies. It is clearly more difficult to distinguish METI in results containing the focal volume, although the tunnelling calculations which are shown (considering ionisation from the ground state only) do underestimate the ion yield in some cases, a possible indication of shake-up excitation effects. Full removal of the focal volume from these results would also help to clarify the ionisation channel. Calculating the METI rate for the pulse durations and wavelengths used in these studies and directly comparing with the experiment should provide further evidence of the importance of excitation effects during tunnel ionisation.

6.4 Conclusion

Experimental evidence for atomic excitation during tunnel ionisation has been presented for the first time, showing a marked agreement with previous theoretical METI predictions. This has been made possible through the development of a new deconvolution technique pioneered in our research group, removing all focal volume and diffraction effects. The use of circularly polarised laser pulses has also been important, allowing the removal of

recollision ionisation effects, although excitation is also expected to occur in a linearly polarised laser field. This research leads to the conclusion that excitation during tunnel ionisation must be considered in future studies. It is predicted that excitation will have an even greater effect in a 5fs laser pulse [Kornev et al., 2003], and should therefore become a significant consideration in few cycle pulse experiments. This work also has important implications for the generation of attosecond pulses; the influence of these excited states must be determined in order to predict the energy of the emitted XUV photons accurately.

Chapter 7

Study of Vibrational Dynamics in D_2^+

Ultrashort laser pulses can be utilised to observe molecular dynamics occurring on an ultrafast timescale. In this experiment, infrared laser pulses of 12fs duration are used to map the motion of a vibrational wave packet in an ensemble of D_2^+ molecules in an essentially field free environment. Vibrational revival dynamics are observed and modelled. This work is currently in submission to Physical Review Letters.

The pump laser pulse tunnel ionises an ensemble of neutral D_2 molecules, exciting a vibrational wave packet in the resulting D_2^+ ions. At the same time, this pump pulse also excites a rotational wave packet in the residual D_2 molecules. A probe pulse is used to map the evolution of both the wave packets after a variable delay time through photodissociation or Coulomb explosion of the D_2^+ ions. The vibrational wave packet dynamics in D_2^+ are isolated and compared with a theoretical simulation. The rotational dynamics observed in the D_2 ensemble will be described in the Chapter 8.

7.1 Introduction

Future targets of ultrafast molecular physics include coherent control [Niikura et al., 2006], where the motion of a molecule is controlled purely by a strong ultrafast laser field. The potential to extend this control to large molecular systems and therefore control reactions in biological molecules is also a long term target [Zewail, 2000]. The present study investigates the simpler systems of hydrogenic molecules, although these molecules are also the fastest systems, vibrating on a timescale of ≈20fs (for D_2^+ $\nu = 0$). Previously, this has been experimentally challenging as the pump and probe pulses used must be of a shorter duration than the timescale of the process to be measured. Pioneering experiments on H_2 and D_2 [Niikura et al., 2003] have lead the way for observations on small molecules. Coulomb explosion is usually used to image the destruction of the wave packet, as after the removal of both electrons the fragments represent a pure two-centre Coulomb system. However in the present study, the low energy photodissociation of the ion has also been used to observe the bound wave packet, in addition to high energy Coulomb explosion.

Another method previously used to trace the motion of the wave packet is the novel *molecular clock* method [Niikura et al., 2003]. Here an electron is tunnel ionised and is subsequently driven back to the core by the laser field to form an ultrafast probe. The electron can produce recollision induced electron-impact fragmentation [Alnaser et al., 2004] or high-harmonic generation [Baker et al., 2006]. Although this technique provides excellent sub-femtosecond time resolution it has some disadvantages, namely that the return times of the electron probe are fixed by the laser frequency, and that it can only investigate molecular motion in the presence of a strong laser field. Pump-probe experiments have the advantage that they can have any delay time and are only limited by the resolution of the translating apparatus producing the delay (which is better than 0.3fs in this experiment). It is also possible to map the almost field-free evolution of the vibrational motion over a long period, as demonstrated by the 750fs range in the present experiment, as the pump pulse has gone before the probe arrives.

7.2 Theory of Vibrational Wave Packet Revivals

An ensemble of D_2^+ ions is created from their neutral ground states by a linearly polarised pump pulse as shown in Figure 7.1. During this ionisation process, a number of vibrational levels are populated in accordance with the Franck-Condon principle. In this way, a vibrational wave packet is created from the coherent superposition of states on the $1s\sigma_g$ potential surface and is allowed to evolve for a time t before a probe pulse causes photodissociation (PD) or Coulomb explosion (CE) of the D_2^+ ions.

The wave packet motion in the potential can be described classically as a series of vibrational states from $v = 0$ to $v = 13$ populated from the D_2 ground state by the laser pulse as shown in Figure 7.1. At the time of creation $t = 0$, the wave packet in the potential is well-defined as the different vibrational states are populated over a short range of R and are in phase with one another. However if allowed to evolve for many periods, the vibrational state populations dephase as they oscillate back and forth across the potential. This dephasing is due to the anharmonicity of the potential well; each vibrational state will oscillate at a different frequency as the energy spacing between levels is no longer constant. Each component of the vibrational wave packet will therefore oscillate with a different frequency, depending on its vibrational state, leading to dephasing. An integer number of periods later, the vibrational states will rephase to form the original well defined wave packet. This wave packet revival can be described classically as the lowest common multiple of all the vibrational state frequencies.

A more quantitative description of the wave packet behaviour is obtained from quantum mechanics. A Fourier expansion can be used to express the coherent superposition of D_2^+ vibrational eigenstates ψ_v which make up the total D_2^+ wave packet $\Psi(R,t)$. Each eigenstate has a frequency $\omega_v = E_v/\hbar$ similar to a classical period, which depends on the eigenenergy (E_v), where v is the vibrational quantum number of the excited eigenstates:

$$\Psi(R,t) = \sum_v a_v \psi_v e^{-i\omega_v t} \tag{7.1}$$

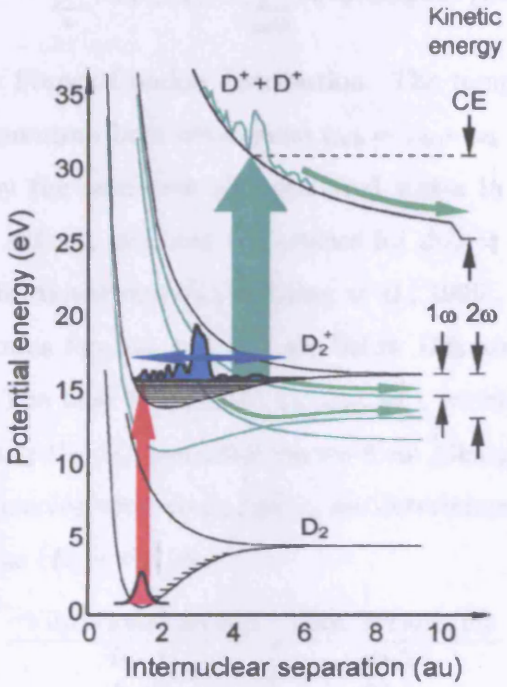

Figure 7.1: Potential energy diagram showing how a vibrational wave packet is created when D_2 is ionised to D_2^+ in an ultrafast 12fs laser pump pulse, and imaged by a 12fs probe pulse. The pump (red) creates a coherent superposition of vibrational states (i.e. a wave packet) in D_2^+ from the ground eigenstate of the D_2 molecule. The wave packet (blue) then evolves on the $1s\sigma_g$ surface, temporally dephasing as a result of the potential energy surface anharmonicity. The probe pulse (green) causes bond fracture either through 1ω or 2ω photodissociation through the photon dressing of the $1s\sigma_g$ and $2p\sigma_u$ surfaces (green surfaces), or Coulomb explosion (CE) shown by the vertical green arrow onto the D^++D^+ repulsive curve.

Here a_v is the overlap integral between D_2^+ eigenstate ψ_v and the neutral D_2 $v = 0$ state which determines the population of a given state, and t is the evolution time of the system created at time $t = 0$. This initially well-defined vibrational wave packet is allowed to propagate temporally, and for a given time t the probability density can be described by $|\Psi(R,t)|^2$:

$$|\Psi(R,t)|^2 = \sum_v |a_v|^2 |\psi_v|^2 + \sum_{v \neq k} a_v a_k^* \psi_v \psi_k^* \cos\{(\omega_v - \omega_k)t\} \tag{7.2}$$

Here, a_v^2 is given by the Franck-Condon distribution. The temporal motion of the wave packet depends on the quantum beat frequencies $\omega_{vk} = \omega_v - \omega_k$ rather than any classical frequencies, as shown by the sum over all populated states in equation 7.2. It should therefore be possible to extract the beat frequencies for Δ_{vk} = 1,2,3... from the experimental results of the vibrational revival [Vrakking et al., 1996]. However, the periods of the significant contributions for Δ_{vk} = 2,3... are below 15fs and will not be resolved in the experimental data. The beat frequencies for $\Delta_{vk} = 1$ which are shown in Table 7.1, have been calculated using the D_2^+ potential curves from [Sharp, 1970] to determine the eigenenergies. Beat frequencies between ω_v and ω_k are determined from the energy spacing of the vibrational levels as $(E_v - E_k)/\hbar$.

Vibrational level v	Beat Period (fs)
0 - 1	21.2
1 - 2	22.1
2 - 3	23.0
3 - 4	24.0
4 - 5	25.1
5 - 6	26.3
6 - 7	27.6
7 - 8	29.0
8 - 9	30.5

Table 7.1: Table showing the period of vibrational beats in D_2^+ at room temperature for $\Delta_{vk} = 1$, i.e. the vibrational beats between levels 0 and 1, 1 and 2, and so on, are calculated.

The wave packet motion is simulated in Figure 7.2 by plotting $|\Psi(R,t)|^2$ for different evolution times t. This shows the probability of finding the molecule at a particular internuclear separation, should the wave packet be collapsed at a particular time t. The initially well-defined wave packet, created over a small range of R, can be seen at $t = 0$.

As it oscillates within the potential well as time progresses, the delocalisation of the wave packet along R can be observed at $t = 50$fs. The subsequent rephasing of all its components in a full wave packet revival can be seen around $t = 550$fs. Also shown at $t = 280$fs is a half-revival, which occurs when all eigenfunctions are stationary, but the even eigenfunctions are out of phase by π with the odd eigenfunctions [Vrakking et al., 1996]. Therefore, at $t = 280$fs the wave packet is fully reconstructed but phase shifted by π from the original wave packet revival at $t = 550$fs.

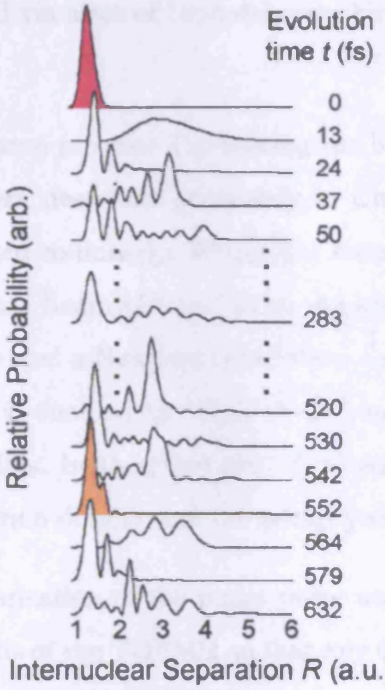

Figure 7.2: Simulations showing how the components of an initially well defined wave packet evolve in time, leading to dephasing. At $t = 0$ when the wave packet is created (pink), the vibrational modes are all in phase. As t increases, the wave packet oscillates spreading out across the $1s\sigma_g$ potential surface. By $t = 50$fs the wave packet has dephased. An integer number of oscillations later, the vibrational modes will rephase to resemble the initial wave packet. Full wave packet revival occurs at $t = 550$fs (orange), the revival period of D_2^+.

7.3 Experimental Configuration

The neutral D_2 gas target was present with a pressure of 3×10^{-7}mbar in the interaction region of the time-of-flight mass spectrometer (TOFMS) previously described in Chapter 4. The laser used was the 1 kHz Femtolasers Ti:Sapphire system at the Astra laser facility producing 30fs pulses at 800nm, which is described in detail in Chapter 3. Using a 1m long argon filled hollow fibre, the pulses were spectrally broadened to a bandwidth of 120nm, then temporally recompressed via a set of 10 multilayer chirped mirrors (Section 2.1.2) to a duration of $\approx$10fs.

The pump and probe pulses were produced by passing the beam through a Mach-Zehnder interferometer, which has been described previously in Chapter 5, to produce two 12fs pulsed beams which propagated co-linearly. Within the interferometer, the pulses are split and recombined in 4μm pellicle beamsplitters which minimised the dispersion. One arm of the interferometer incorporated a Newport translation stage, interfaced to a LabVIEW data acquisition system which enabled the high resolution (1/3 fs) variable time delay between pump and probe pulses. In the other arm there was a thin broadband $\lambda/2$ plate which controlled the polarisation direction of the pump pulse.

For this experiment, the polarisation of the pump pulse was orientated perpendicular to the time-of-flight detection axis of the TOFMS, so that any deuterium fragments produced by this pulse would not pass through the 250μm limiting aperture before the drift tube. The polarisation of the probe pulse was parallel to the detection axis to ensure maximum detection of the fragments produced, as the aperture limits the field of view of the TOFMS to $\leq 2°$. The aperture also exposes only a 250μm slice of the laser focus to the detector, so that the fragments are produced by only the high intensity central region. This prevents averaging over the whole intensity range of the focus. The 12fs pulses were reflection focused into the interaction region using a f/5 spherical mirror mounted inside the vacuum chamber of the TOFMS. Pulse intensities were 8×10^{14}Wcm^{-2} and 6×10^{14}Wcm^{-2} for pump and probe pulses respectively.

7.4 Results

The resulting D^+ ion spectra from the pump-probe experiment are displayed in Figure 7.3 as a function of kinetic energy and evolution time. The low energy band (0eV - 1eV) is due to photodissociation (PD), while the high energy band (2eV - 6eV) results from Coulomb explosion (CE) of the molecular ion. The PD band is a combination of 1ω and 2ω dissociation, which cannot be individually resolved as a range of vibrational levels around the 3ω gap can be accessed (Chapter 1) leading to overlap in the energy distributions from the two processes. The PD signal clearly shows a periodic modulation in the ion yield of ≈24fs at $0 \leq t \leq 100$fs which is repeated at $500 \leq t \leq 650$fs forming the vibrational revival. The revival modulation is also evident in the CE band at higher energy for $500 \leq t \leq 650$fs.

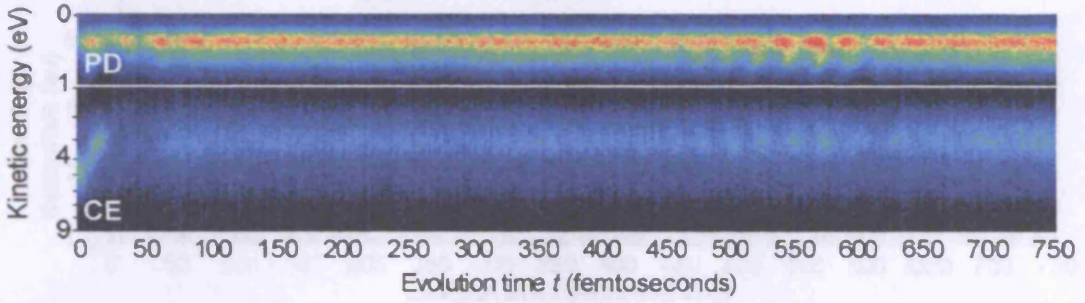

Figure 7.3: False colour map showing the time-of-flight spectra of D^+ ions converted to kinetic energy as a function of pump-probe delay time t (evolution time). The top band is due to photodissociation and has low energy (0eV - 1eV), while the bottom band showing Coulomb explosion has a higher energy (2eV - 6eV).

The energy of the CE fragments is inversely proportional to the internuclear separation R at which the wave packet is promoted to the CE curve. For a very intense laser pulse it would be possible to map the promotion of the wave packet on to this curve for a range of R through the CE energy of the fragments. However the peak intensity of the probe pulse in the present experiment (6×10^{14}Wcm^{-2}) can only image the wave packet at large R when it is closer in energy to the bound $1s\sigma_g$ potential curve. The increase in ion yield in the CE band at $0 \leq t \leq 25$fs is due to the temporal overlap of the pump and probe pulses within these times. This overlap effectively gives rise to one intense laser pulse of varying duration and ellipticity (as pump and probe pulses have orthogonal polarisation

directions) during these delay times.

The first set of modulations show that the pump pulse creates a coherent superposition of vibrational states (i.e. a wave packet) in the D_2^+ ion at $t = 0$fs, which dephases over the next 100fs. The modulations arise from the wave packet oscillating back and forth across the well ($v = 0$ period is 20fs), with an enhancement in the probability of PD or CE at the outer turning point (≈3.5 a.u.). In this way, the internuclear potential surface naturally acts as a quantum shutter or barrier to wave packet detection. The oscillatory motion of the wave packet in the potential is evident from the simulation shown in Figure 7.4, where the probability distribution of the wave packet $|\Psi(R,t)|^2$ has been plotted for $0 \leq R \leq 6$a.u. and evolution times $0 \leq t \leq 750$fs. The population of the vibrational states follows a Franck-Condon distribution. A Gaussian spread of 13fs has been included in the calculation, to allow for both the pump and probe pulse durations.

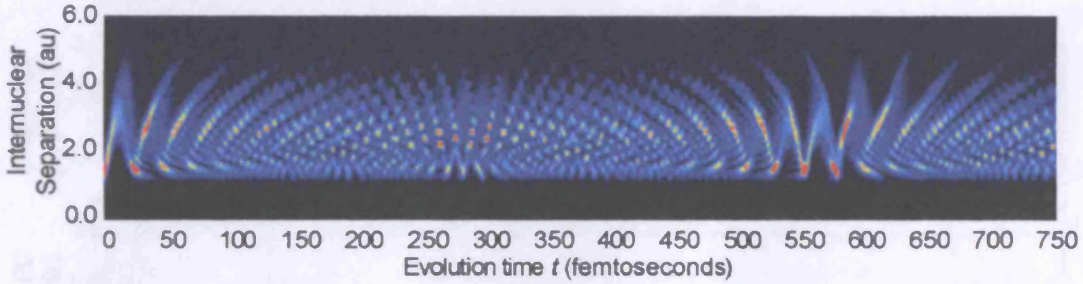

Figure 7.4: Calculated probability distribution of the vibrational wave packet $|\Psi(R,t)|^2$ as a function of internuclear separation R. Vibrational state populations are calculated according to the Franck-Condon principle. When the vibrational states are in phase, their constructive interference leads to wave packet revival structure.

The revival structure results from constructive interference of the different vibrational states ψ_v, which can be seen from the second term of equation 7.2. Initially the states are in phase and constructively interfere, but during their evolution in time dephasing occurs as the wave packet spreads out across R. After approximately 550fs, the vibrational states are back in phase and constructively interfere again giving rise to the revival structure. At an evolution time $250 \leq t \leq 350$fs, a half revival can also be observed in both experimental (Figure 7.3) and theoretical results (Figure 7.4). A degree of constructive interference occurs at this time which is observed as a small revival oscillation at 280fs.

Integrated results are presented in Figure 7.5 for further analysis. It is apparent from the PD results in Figure 7.5(a) which show the data in Figure 7.3 integrated over the energy range 0eV to 1eV that there is a slow modulation also occurring in the experimental results around 280fs. This is due to the presence of a *rotational* half-revival occurring in the D_2 molecule in the observed ion signal. This rotational wave packet is created in the neutral D_2 molecule by the pump pulse at the same time as the vibrational wave packet is created in the D_2^+ ion and is therefore also observed in the D^+ signal. The neutral D_2 molecule vibrates incoherently as the pump duration is greater than the D_2 quasi-classical period of 11fs [Ergler et al., 2006a], so no vibrational revival structure is present from the neutral molecule. The vibrational and rotational processes can therefore be separated as there is no evidence for a rotational revival in the D_2^+ ion. A D_2^+ rotational revival would appear as a slow modulation similar to that observed in the D_2 here, but with half the period [Ergler et al., 2006b].

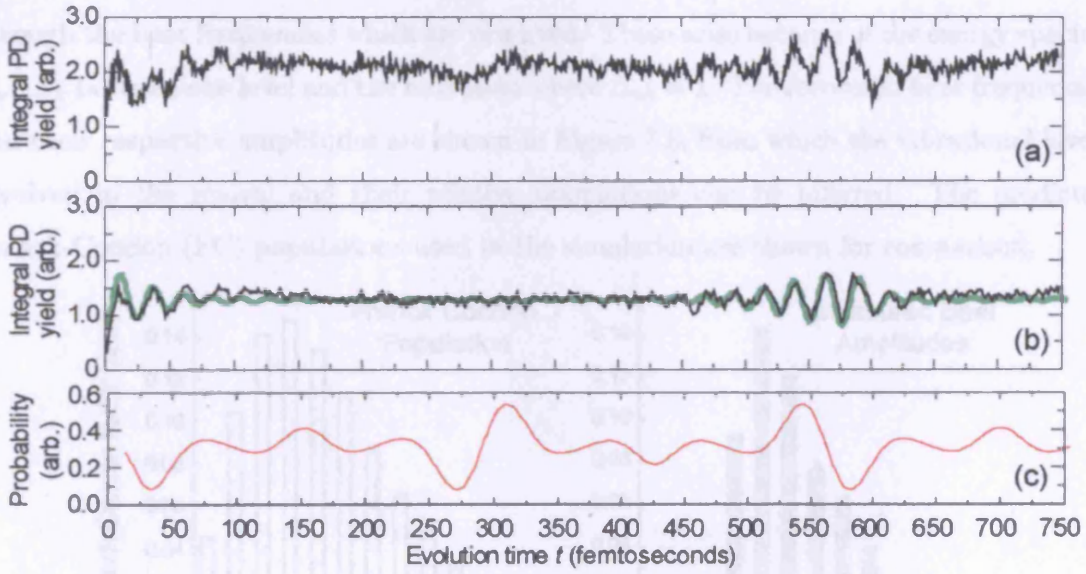

Figure 7.5: (a) Integration of the PD spectra shown in Figure 7.3 between 0eV and 1eV, which contains rotational and vibrational revivals. (b) Integrated PD spectra with rotational revival structure subtracted to leave only vibrational information (black). An integration of the vibrational theoretical simulation in Figure 7.4 $R > 3$a.u. is compared with the experiment. An excellent agreement between experimental and theoretical results is observed. (c) The calculated impulsive rotational alignment of D_2 induced by the pump pulse (see Chapter 8), which has been subtracted from (a).

In order to compare the experimental and theoretical vibrational results directly, the

rotational revival has been subtracted from the data. A calculation of the rotational revival structure by Torres (for details see [Torres et al., 2005]) is shown in Figure 7.5(c). This has been subtracted from the integrated PD ion signal in Figure 7.5(a), leaving only the ion signal due to vibration in D_2^+ shown as the black curve in Figure 7.5(b). Further details of the rotational revivals observed in the D_2 molecule are given in Chapter 8. The PD signal can now be directly compared to the theory (green curve) in Figure 7.5(b). This theoretical curve is an integration of the simulation in Figure 7.4 for $R > 3$a.u. which embraces the outer turning points of the D_2^+ potential well. An excellent agreement between the experimental and theoretical integrals can be observed; the experimentally observed vibrational revival structure is extremely well predicted by the theory.

To determine the beat frequencies of the vibrational levels that lead to vibrational revival, a Fourier transform of the experimental time-dependent PD results in Figure 7.5(b) is performed. The resulting frequency spectrum gives an indication of the vibrational levels through the beat frequencies which are observed. These arise because of the energy spacing $E_v - E_k$ between one level and the next level where $\Delta_{vk} = 1$. The recovered beat frequencies and their respective amplitudes are shown in Figure 7.6, from which the vibrational levels involved in the revival and their relative populations can be inferred. The predicted Franck-Condon (FC) populations used in the simulation are shown for comparison.

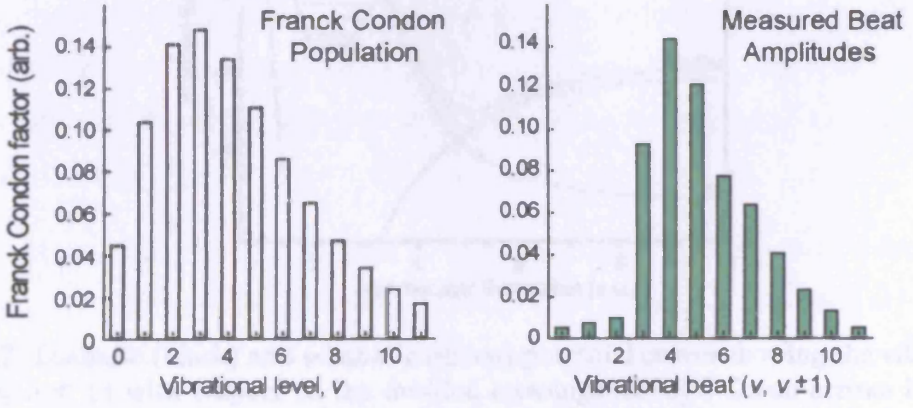

Figure 7.6: The predicted Franck-Condon (FC) distribution of population in the vibrational levels is calculated (left). A Fourier transform (FT) of the experimental PD results (right) yields the beats between vibrational states v and $v + 1$ present in the vibrational revival. The beat amplitude is a measure of the vibrational population.

It can be seen that there is a good agreement between the measured distribution of beat frequencies between vibrational states v, $v+1$ and the expected FC distribution of states for $v > 3$. For states $v \leq 3$ the FC populations are large, but the experimentally measured beats are small. It is expected that these lower lying states are highly populated but are not accessible in the experiment as they lie below the 3ω avoided crossing (as shown in Figure 7.7). The probe intensity in this experiment of 6×10^{14} Wcm^{-2} is not sufficient to open this gap wide enough to allow dissociation of these lower levels, therefore they are not detected.

The majority of the population is within the levels $3 < v \leq 7$, which can be accessed through the 3ω avoided crossing. The probe intensity is sufficient to open the gap wide enough at this point for these v-states to dissociate via a net 2-photon process along the 2ω curve (Chapter 1). A smaller proportion of the FC population is distributed in states $v > 7$. These states can dissociate via the 1ω crossing at the $v = 13$ level when the gap is opened and are therefore also detected.

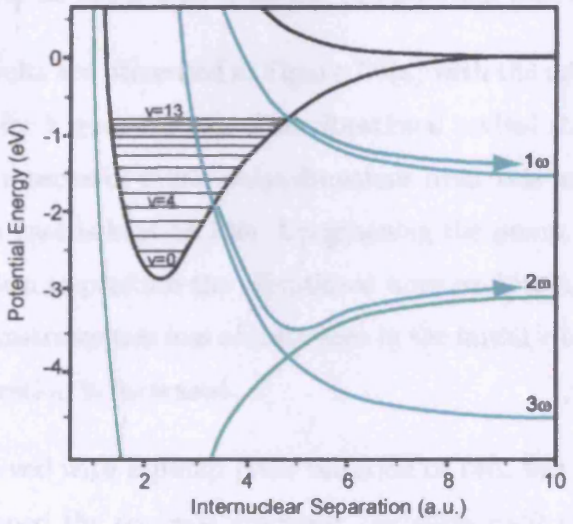

Figure 7.7: Diabatic (black) and adiabatic (green) potential curves showing the vibrational levels $0 \leq v \leq 13$ with respect to the avoided crossings for D_2^+. Green arrows illustrate the dissociation paths (when the gap at each avoided crossing is opened by the laser field) via the 1ω crossing (1ω dissociation) and 3ω crossing (net 2ω dissociation).

Overall there is a good agreement between the Franck-Condon populations and the experimentally obtained vibrational beats, the amplitude of which provide a measure of the

population. The difference observed in the $v \leq 3$ states can be explained after studying the dissociation pathways in Figure 7.7, with the conclusion that the laser intensity is not high enough to suppress the potential and allow dissociation of these lower lying states.

7.4.1 Control of the Vibrational Wave Packet

In order to exert control over the coherence of the wave packet, the pulse durations of the pump pulse and the probe pulse are varied independently. By changing the pump pulse duration, the initial vibrational coherence of the wave packet can be influenced, as the degree of coherence is dependent on the time taken to create the wave packet. When the probe pulse is changed, the ability to distinguish the 24fs modulation structure of the wave packet revival is studied. In both cases, a series of glass slides were used to dispersively stretch the laser pulse, which was measured by autocorrelation. An understanding of the limits to coherent wave packet creation and their subsequent measurement is of great interest and importance for studies on quantum computation [Lee et al., 2004].

The integrated PD results are presented in Figure 7.8(a) with the rotational structure subtracted (as described for Figure 7.5(b)). The vibrational revival structure (black curves) is shown, taken using a series of pump pulse durations from 14fs to 28fs, while the probe pulse duration in each case is kept at 13fs. Lengthening the pump pulse has the effect of increasing the time taken to produce the vibrational wave packet. A loss of contrast in the revival structure demonstrates this loss of coherence in the initial vibrational superposition as the pump pulse duration is increased.

Good contrast is observed with a pump pulse duration of 14fs, but as the duration of the pump pulse is lengthened the contrast gradually decreases until the revival structure is barely distinguishable from the background at 28fs. A number of simulations have been performed, similar to that in Figure 7.4, where the temporal spread over which the wave packet is created has been increased for the same values as in the experiment. Pump pulse duration is kept constant at 13fs. The full simulations for each pump duration are shown in Figure 7.8(b), while an integration over $R > 3$a.u. is compared with each experimental result in Figure 7.8(a) as a magenta curve. There is a good agreement

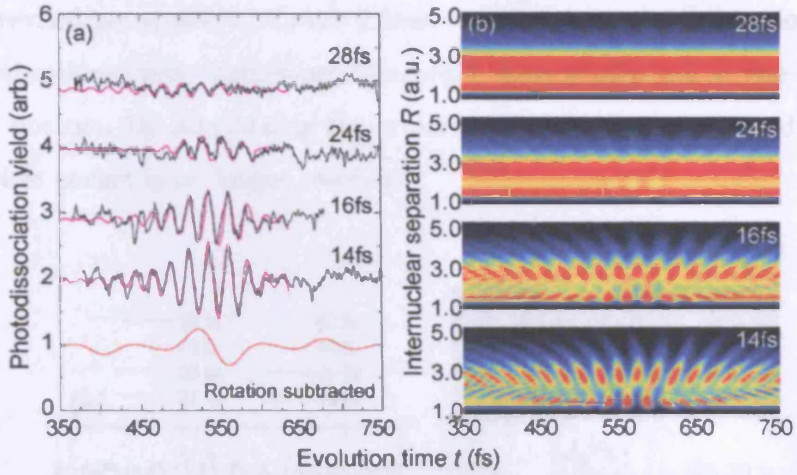

Figure 7.8: Controlling the initial superposition conditions in a vibrational wave packet revival. (a) Integrated PD results (black curve) for a range of pump pulse durations from which the rotational structure (bottom) has been removed. The decreasing contrast of the revival modulation structure shows how the coherence is lost in the superposition as the pump pulse duration increases. (b) Predicted shape of the vibrational wave packet revival, averaged over the varying pump pulse duration. An integration of this simulation is shown in (a) as magenta curves. The spectra are offset for clarity.

between the theoretically predicted and experimentally observed loss of contrast in the vibrational revival structure.

The period of the revival structure oscillation observed in Figure 7.8(a) is 24fs. From the results, it can be inferred that the longer pump pulse of 24fs is able to coherently populate only the higher lying vibrational states, which have a period longer than 24fs. The lower lying states will be incoherently populated as they have a period similar to the duration of the pump pulse, and therefore will not revive. As a consequence of this, the low contrast revival structure observed in Figure 7.8(a) with a 24fs pump pulse is solely due to these higher lying states, the longest of which $v = 13$ has an oscillatory period of 39fs. Although the vibrational states $9 \leq v \leq 13$ make up only 4% of the total population, they still exert an influence over the evolution of the wave packet. It can be concluded that a pump pulse of duration less than 24fs is required to create a coherent wave packet in D_2^+.

In the second stage of this experiment, the pump pulse was kept at a duration of 14fs while the probe pulse was varied from 14fs to 60fs. The integrated PD results showing the

wave packet revival are shown in Figure 7.9(a). As the pump pulse duration is constant at 14fs, the vibrational wave packet produced each time is identical to the simulation in Figure 7.8(b) bottom. By lengthening the probe pulse, a limit can be found at which the vibrational wave packet is no longer resolved.

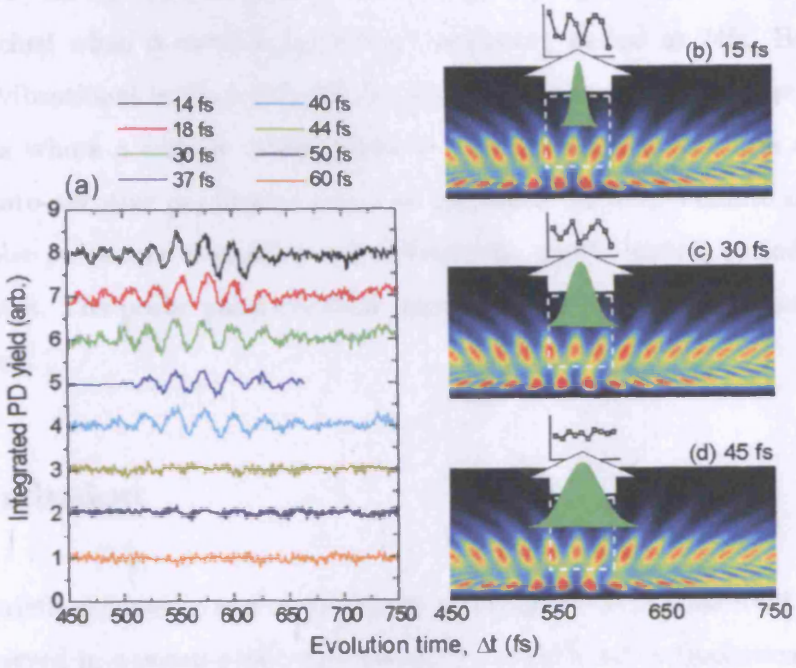

Figure 7.9: Changing the duration of the imaging probe pulse while the pump pulse duration remains constant at 14fs. (a) A sudden loss of contrast in the revival modulations arises for durations > 40fs, as the maxima cannot be resolved. The probe can resolve revival structure at shorter durations, as shown for (b)15fs and (c)30fs but at (d)45fs the wave packet structure cannot be distinguished.

It can be seen that the contrast of the revival structure is well resolved and is almost constant for probe pulse durations between 14fs and 40fs. A slight decrease in modulation amplitude as the probe pulse duration increases from 14fs to 40fs results from blurring of the wave packet image. Above 40fs the resolution is suddenly lost as the 44fs probe pulse fails to detect any vibrational revival structure. This dramatic loss of resolution occurs as the probe duration approaches double the quasi-classical period of the D_2^+ ion (20fs for $v = 0$), as the probe can no longer distinguish between any two maxima in the revival. This is illustrated schematically by the green probe pulse shown in Figure 7.9. At (b) 15fs the structure is well resolved, at (c) 30fs it is less well resolved, and at (d) 45fs the duration

of the probe pulse cannot resolve the structure. A well defined cut-off duration for the probe pulse can be stated as double the quasi-classical period of the observed system.

From this study, the limits of coherent wave packet production and detection can be defined. A cut off for the pump pulse duration producing a coherent vibrational wave packet is reached when it exceeds the revival oscillatory period at 24fs. However, some higher lying vibrational levels could still be populated coherently at this pulse duration. For situations where a strictly defined limit is required such as quantum computing, a method of state-selective population could be employed. A more definite cut off for the resolving probe pulse has been observed at twice the quasi-classical period of vibration for the ion, 40fs. The probe pulse duration must be below this limit to ensure total wave packet collapse.

7.5 Conclusion

The characteristic dephasing and rephasing of an ultrafast vibrational wave packet in D_2^+ has been observed in a pump-probe experiment, and compared to theoretical simulations. Vibrational populations of the wave packet have been determined from the experiment and found to agree with FC predictions. In general, a good agreement has been observed between the experimental and theoretical results. The constraints for pump and probe pulse durations when creating and observing the wave packet have been investigated, which may be of importance for applications such as quantum computing; creating a vibrational wave packet is analogous to writing a vibrational qubit, and its detection at the outer turning point of the potential well is equivalent to reading the final state of the qubit [Lee et al., 2004]. This research on the simple quantum system of D_2^+ is also of fundamental interest in the field of molecular dynamics.

Chapter 8

Rotational Dynamics of D_2 Molecules

This chapter presents a study of the temporal evolution of a rotational wave packet in neutral deuterium molecules observed in a pump-probe experiment, which demonstrates impulsive alignment of the molecule to the laser field polarisation direction. The polarisation angle of the ultrafast (12fs) pump pulse was rotated in a series of experiments, causing impulsive alignment of the molecule to this axis.

The field-free evolution of the rotational wave packet has been mapped by the probe pulse (also 12fs), which initiates a Coulomb explosion process in the molecule. As the detection of this process is highly dependent on the orientation angle of the molecular axis with respect to the polarisation direction, a map of the rotational wave packet has been generated from the results. Rotational revivals of the neutral D_2 wave packet as a function of polarisation direction and evolution time have been observed and compared to a theoretical simulation. The results of this experiment have been published in [Bryan et al., 2007].

8.1 Introduction

An intense linearly polarised laser pulse can interact with a random ensemble of molecules to generate a degree of spatial alignment in the ensemble [Seideman, 1999]. For strong field alignment to occur, the molecular polarisability must be anisotropic. If a long laser pulse is used, the laser field will be applied adiabatically and each molecule will align its most polarisable axis along the laser polarisation direction (adiabatic alignment is described in Chapter 1). If the laser pulse is short in comparison to the molecular rotational period, the pulse imparts angular momentum to the molecules while they remain essentially stationary. The molecule receives an impulse towards the direction of laser polarisation, and the resulting rotational wave packet will continue to rotate diabatically long after the laser pulse has gone. This is the impulsive alignment regime, also described in Chapter 1, in which this experiment takes place. The alignment can be observed as a series of full revivals at integer multiples of the fundamental rotational period.

The use of a short laser pulse to impulsively align an ensemble of molecules was first investigated theoretically by [Seideman, 1995]. Rotational wave packets created in heavy many-electron systems have been studied (e.g N_2 [Dooley et al., 2003]), which have rotational periods of the order of picoseconds and can therefore employ an aligning pulse with a relatively long duration. As the rotational period of D_2 is $(2B_0c)^{-1} = 558$fs, an aligning pulse with a duration of tens of femtoseconds is required. A study of the field free alignment of D_2 using 10fs pulses has also been recently performed by [Lee et al., 2006], although the results have limited temporal resolution. The present study demonstrates improved temporal resolution, and also measures the angular evolution of the rotational wave packet through the rotation of the pump pulse polarisation angle.

In this study, a linearly polarised few cycle laser pulse of 12fs duration is employed to impulsively align an ensemble of D_2 molecules. The rotational wave packet is produced in the neutral deuterium molecule D_2 by one laser pulse, and probed a short time later using a similar pulse that initiates sequential double ionisation to D_2^+, which subsequently Coulomb explodes. The D^+ fragments from Coulomb explosion are detected using a high resolution time-of-flight mass spectrometer, so that a precise gauge of the degree of

alignment of the ensemble is obtained.

In a second set of experiments also presented here, the angular distribution of the ensemble in the region of a half-revival is studied. By rotating the linearly polarised pump pulse for a range of pump-probe delay times a map of the rotational wave packet is created. This is directly compared with a theoretical simulation.

8.2 Theory of Rotational Wave Packet Revivals

A linear molecule is exposed to a nonresonant linearly polarised laser field:

$$\vec{E}(t) = \hat{\varepsilon} E_0 f(t) \cos \omega t \tag{8.1}$$

where $\hat{\varepsilon}$ is a unit vector along the pump polarisation direction, E_0 is the field amplitude, $f(t)$ is the pulse envelope and ω is the laser frequency. The laser pulse shape is assumed to follow a sech^2 distribution, with a pulse duration of 12fs.

The D_2 molecules are described as a thermal ensemble of rigid rotors with the eigenstates of each molecule denoted by quantum numbers J and M in the absence of the laser field. To describe the wave packet produced by the short laser pulse as it evolves in time, a sum over the rotational states can be written:

$$\Psi(t) = \sum_J a_J e^{-iE_J t/\hbar} |J, M\rangle \tag{8.2}$$

where E_J are the energy eigenvalues for the rotational J-states, and $|J, M\rangle$ are spherical harmonics where M determines the orientation of the J vector, and is conserved in a linearly polarised field. The amplitude coefficients a_J are determined by the interaction of the laser pulse with the molecules. The rotational energy eigenvalues E_J can be calculated from:

$$E_J = B_0 J(J+1) \tag{8.3}$$

where B_0 is the ground state rotational constant. For D_2, $B_0 = 30\text{cm}^{-1}$. As deuterium is

a boson, the total wave function of the D_2 molecule must be symmetric with respect to the interchange of nuclei, and the electronic ground state is also symmetric. The nuclei can form $(2I + 1)(I + 1)$ ortho-D_2 (symmetric) nuclear wave functions occupying even J-states, and $(2I + 1)I$ para-D_2 (antisymmetric) nuclear wave functions occupying odd J-states. Therefore, spin statistics for a homonuclear D_2 molecule are given by:

$$\frac{No.\ Symmetric\ Functions}{No.\ Antisymmetric\ Functions} = \frac{I+1}{I} \tag{8.4}$$

As $I = 1$ for each nuclei, the spin statistics weighting of ortho-D_2 : para-D_2 is 2:1 in a thermal ensemble.

The temporal evolution of the rotational wave packet, as in the vibrational case, is dependent on the beat frequencies between rotational levels as shown below rather than the absolute frequencies where $\omega_J = E_J/\hbar$. For the anisotropically polarisable deuterium molecule, allowed Raman transitions are for $J = \pm 2$, so beats between levels J and $J + 2$ are expected. These beats can be calculated from equation 8.5 and are shown in Table 8.1 below:

$$\Delta\omega_{J,J+2} = \frac{E_{J+2} - E_J}{\hbar} = \frac{B_0}{\hbar}[(J+2)(J+3) - J(J+1)] = (4J+6)\frac{B_0}{\hbar} \tag{8.5}$$

J-state	D_2 Beats (fs)	D_2^+ Beats (fs)
0 - 2	182.61	377.16
1 - 3	109.57	266.30
2 - 4	78.26	161.64
3 - 5	60.87	125.72
4 - 6	49.80	102.86
5 - 7	42.14	87.04

Table 8.1: Table showing the rotational beat periods between J-states for D_2 and D_2^+ calculated from equation 8.5. Rotational constants are B_0=30 cm^{-1} for D_2, and B_0=15 cm^{-1} for D_2^+.

The molecular D_2 ensemble is initially isotropic (Figure 8.1). The arrival of the laser pulse induces a rapid net alignment, and each J-state within the rotational wave packet

accumulates a relative phase with a different angular frequency given by

$$\omega_J = \frac{1}{2} J(J+2)\omega_1 \tag{8.6}$$

where $\omega_1 = 4\pi B_0 c$ is the fundamental rotational frequency (1.131×10^{13} Hz in D_2). After the laser pulse has gone, the wave packet is effectively evolving in a field free environment. The constituent J-states quickly dephase with respect to each other, dissipating the initial net alignment. After a time the J-states will start to rephase. When the relative phases of each J-state are equal (to within multiples of 2π), the initial net alignment is reconstructed as the molecular axes are once again parallel to the polarisation vector of the initial pulse. This is called full wave packet revival. The relative phases of the J-states can also produce antialignment in the ensemble, where the molecular axes are orientated perpendicular to the initial pulse polarisation vector, creating a half-revival. As $J(J+2)$ is even for all J, the angular frequencies ω_J are integer multiples of the fundamental frequency ω_1. Therefore, the time at which the first full revival occurs is given by $2\pi/\omega_1 = (2B_0 c)^{-1} = 558$fs. Significant net alignment and antialignment of molecules, observed as a partial revival, can also occur at 1/4 and 3/4 of the rotational period.

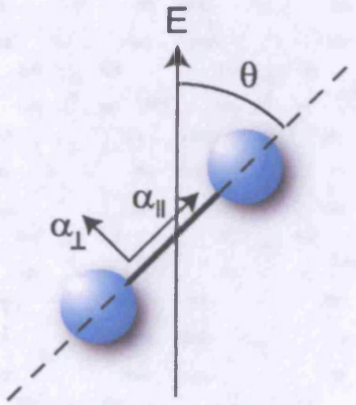

Figure 8.1: Impulsive alignment of a D_2 molecule by an intense femtosecond laser pulse. Due to the polarisability anisotropy $\Delta\alpha = \alpha_\perp - \alpha_\perp$ the molecule experiences a potential in the presence of the laser electric field E. A coherent excitation of the rotational J-states takes place, and molecular alignment is determined by the relative phases of the J-states. Angle θ is defined as the angle between the molecular axis and the electric field vector.

In order to compare theoretical results with the experimentally obtained time- and angle-dependent ion yield, a $\langle \cos^2\theta \rangle$ distribution is plotted, where θ is the angle between the

molecular axis and the laser electric field vector. For an ensemble of molecules in thermal equilibrium, $\langle\cos^2\theta\rangle$ must be averaged over the Boltzmann distribution of initial rotational J-states. The use of $\langle\cos^2\theta\rangle$ plotted as a function of time is typical of rotational revival literature, where a $\langle\cos^2\theta\rangle$ value of 1/3 reflects an isotropic distribution of molecules. A value of 1 would occur for an idealised molecular ensemble perfectly aligned along the electric field (i.e. polarisation direction) axis, whereas a value of 0 indicates that all molecules are aligned in a plane perpendicular to this axis (antialignment).

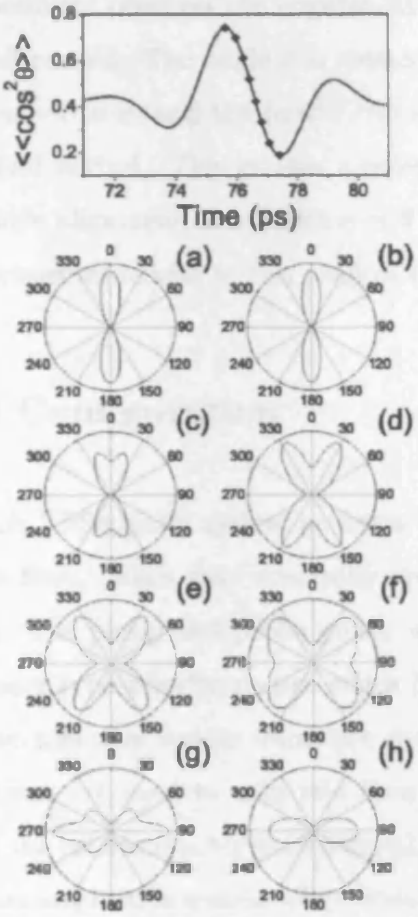

Figure 8.2: Snapshots of the angular distribution of an ensemble of CS_2 at 10K aligned by a laser pulse of 10^{13}Wcm^{-2} and 100fs duration around full revival; (a) t = 75.60ps, (b) t = 75.95ps, (c) t = 76.20ps, (d) t = 76.40ps, (e) t = 76.6ps, (f) t = 76.80fs, (g) t = 77.05ps, (h) t = 77.40ps. The points in the $\langle\cos^2\theta\rangle$ plot corresponding to each snapshot are shown (top). The radii are not at the same scale. Figure reproduced from [Torres et al., 2005].

A calculated $\langle \cos^2 \theta \rangle$ distribution for CS_2 molecules around a full revival is shown in Figure 8.2 from [Torres et al., 2005]. At each point between alignment and antialignment inside the revival, the angular distribution of the molecular ensemble has been calculated. It is interesting to note that the angular distributions always display a degree of alignment (predominantly around 30°) in a variety of butterfly-shaped distributions as the revival evolves, rather than an isotropic distribution. These occur independently of the molecule used and the conditions of the impulsive interaction.

The second part of this experiment observes the angular distribution of the D_2 molecules in the region of the first half-revival. The angle θ is rotated with respect to the electric field direction over the range $-\pi$ to π, and the $\langle \cos^2 \theta \rangle$ for each angle is plotted over the evolution time of the first half revival. This creates a colour map or so-called quantum carpet simulating the ensemble alignment as a function of θ and evolution time Δt which can be compared with experimental results in this chapter (section 8.4.1).

8.3 Experimental Configuration

The laser used was the 1 kHz Ti:Sapphire system at Astra TA1, described in Chapter 3. Using an argon filled hollow fibre, pulses were spectrally broadened then compressed via a set of 10 chirped mirrors. The pump and probe pulses were produced by passing the beam through a Mach-Zehnder type interferometer, which has been described previously in Chapter 5, to produce two identical beams which are co-linearly propagating. Pellicle beamsplitters of 4μm thickness are used to split and then recombine the pulses in the interferometer. One arm of the interferometer incorporated a Newport translation stage, interfaced to a LabVIEW data acquisition system which enabled the high resolution (better than 1/3 fs) variable time delay (probe pulse). In the other arm, a half-wave plate is mounted to allow variation of the polarisation direction of the pump pulse.

For the first experiment, the pump pulse polarisation is orientated perpendicular to that of the probe pulse, defining the direction of the electric field vector described in the previous section (Figure 8.1). The probe pulse is orientated parallel to the detection axis of the

TOFMS. This configuration ensures that only ion fragments produced by the probe pulse enter the detector and contribute to the observed D^+ signal from which the rotational wave packet dynamics are observed. Pump-probe delay times extend up to 800fs to observe half ($t \approx 280$fs) and full ($t \approx 550$fs) revival structures.

For the second experiment, the orientation of the pump pulse is rotated through the range $-\pi$ to π with respect to the unchanged probe polarisation direction (green arrow in Figure 8.3). This has the effect of rotating the molecular axes of the D_2 ensemble, equivalent to rotating the spectrometer around the interaction region. Angular distributions over a pump-probe range around the first half revival ($t \approx 280$fs) are obtained. In this way, we are able to map the rotational wave packet created in deuterium by a 12fs pulse for a large range of initial alignment angles.

Pump and probe pulses have previously been generated by passing the beam through a core-annulus plate [Lee et al., 2006], where the outer part of a circular glass plate is rotated with respect to the central core part to produce the delay. Although the interferometric technique used in this experiment results in greater energy loss due to beamsplitters, it has can produce a much greater time delay between the pulses and also allows for polarisation control using a half-wave plate, which is not possible with the core-annulus technique. A SHG autocorrelator was used to measure a pulse duration of 12fs arriving at the interaction region. The focused intensities of the pump and probe beams were $8\times10^{14}\text{Wcm}^{-2}$ and $6\times10^{14}\text{Wcm}^{-2}$ respectively.

The pulsed beams entered a time-of-flight mass spectrometer (described in Chapter 4), where they were focused into the interaction region using a reflective f/5 optic, as shown in Figure 8.3. D_2 gas was present as a diffuse target within the interaction region. The pump pulse initiates the impulsive alignment and creates a rotational wave packet in the neutral D_2 molecule, and the populated J-states are free to evolve after the pump pulse has gone. The probe pulse sequentially ionises the molecule, producing D_2^+ followed by D_2^{2+} which rapidly Coulomb explodes ($D^+ + D^+$) with high energy ($\approx$5.5eV).

The detection of Coulomb explosion D^+ fragments is a good measure of the alignment of the ensemble, as the direction of the fragments is highly sensitive to the orientation of the

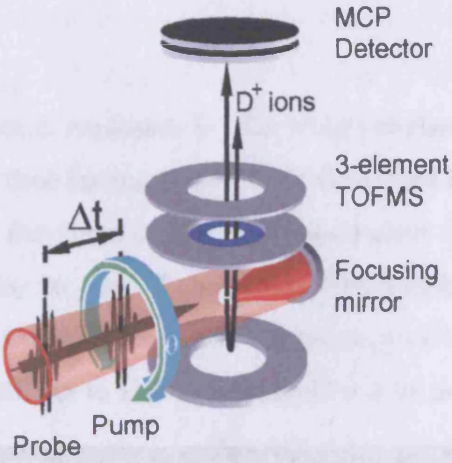

Figure 8.3: Schematic of experimental configuration showing pump and probe pulses and time-of-flight mass spectrometer (TOFMS). The time delay between the pulses is Δt, and the angle θ between (aligning) pump and (imaging) probe polarisation directions is varied by altering the pump polarisation direction. Figure from [Bryan et al., 2007].

internuclear axis. Forwards and backwards ions are produced (as described in Chapter 1), where forwards ions have an initial velocity in the direction of the detector, and that of the backwards ions is in the opposite direction, but they are turned around by the extraction field of the TOFMS and therefore detected at a later time. Only the forwards ions are used for this experiment due to the imperfect turnaround of the backwards ions leading to a low rate of detection.

By extracting the energetic Coulomb explosion fragments through a 250 μm aperture above the interaction region, a precise gauge of the degree of alignment of the ensemble is obtained, as the fragments will only be detected if they Coulomb explode in the direction of the probe pulse, which is parallel to the detection axis. The aperture limits the angular acceptance of the spectrometer to $\leq 2°$ for a 5.5eV D^+ ion, and also restricts the field of view of the spectrometer. As a consequence, only a 250 μm slice of the laser focus is exposed the detector so that the fragments detected are produced by a restricted intensity range. This avoids spatial integration over the focal volume and results in a higher resolution measurement of the rotational wave packet than in previous studies.

8.4 Results

Measurements of the Coulomb explosion D^+ ion yield are shown in Figure 8.4. Ion yield as a function of evolution time (pump-probe delay time) and kinetic energy is plotted as a false colour map in (a). For these results, the polarisation direction of the pump pulse is at $\theta = 90°$, perpendicular to that of the probe pulse which is parallel to the time-of-flight detection axis. Any Coulomb explosion fragments produced by the pump pulse are therefore directed perpendicular to this axis and will not be detected.

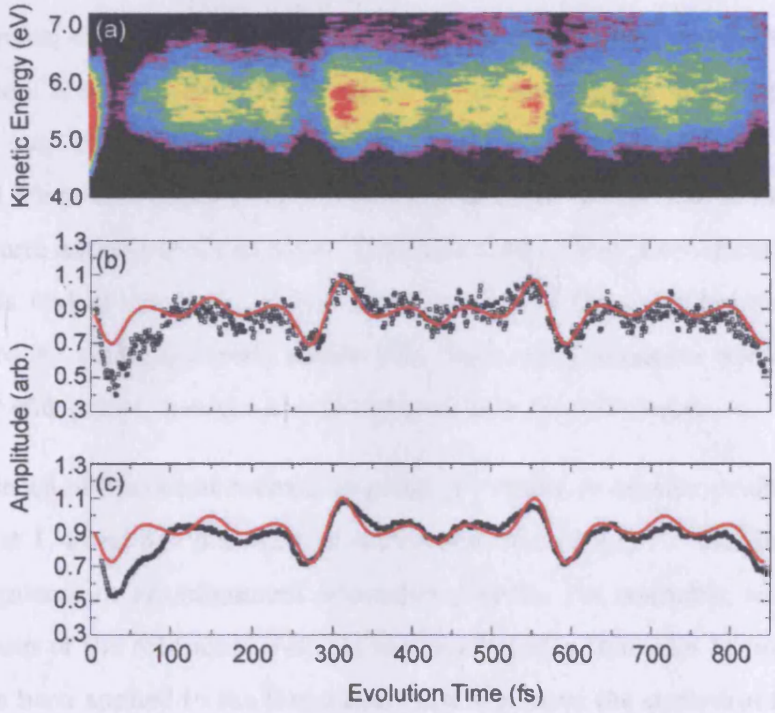

Figure 8.4: (a) False colour representation of the Coulomb explosion yield (D^+ ions) as a function of pump-probe delay (wave packet evolution time). (b) Integrated Coulomb explosion yield (black points) compared with a theoretical simulation of a rotational wave packet in D_2 in the impulsive regime (red line). (c) Integrated Coulomb explosion yield following 11-point smoothing (black points) compared with theory as in (b). For these results, the pump pulse polarisation direction is at an angle of 90°, perpendicular to the probe pulse polarisation direction, which is parallel to the time-of-flight axis. Adapted from [Bryan et al., 2007].

The rotational revival structure is evident from the modulation of the signal throughout the evolution time. In (b) the full revival can be observed at 560fs, very close to the

calculated period of 558fs, and the half revival at 280fs. This plot shows the experimentally obtained D^+ yield shown in (a) integrated over the kinetic energy range (black points). The red curve is a theoretical simulation performed by R. Torres, Imperial College (see [Torres et al., 2005] for details), which is in excellent agreement with the experimental results. At small evolution times of 0fs $\leq \Delta t \leq$ 100fs, the temporal wings of the pump and probe pulses will overlap to produce a resultant circularly polarised pulse at 0fs, while elliptical polarisation will occur at later times. For evolution times $\geq$200fs, the time dependent signal modulation is considered to be solely due to the rotational wave packet.

At the full revival time (when all the eigenstates of the rotational superposition are back in phase), there is a large peak in the signal as the ensemble is aligned parallel to the time-of-flight axis, indicating maximum alignment at 550fs. A large trough is also present in the revival when the ensemble is aligned perpendicular to the time-of-flight axis, indicating maximum antialignment at 590fs. It is clear that a short pulse duration is required to resolve this revival structure, as the alignment axis of the ensemble changes from 0° (alignment) to 90° (antialignment) within 50fs. Such rapid dynamics would be unresolvable using 40-60fs pulses, but are clearly resolved with the 12fs pulses.

There is evidence of fractional revivals in panel (b) visible as smaller peaks and troughs, which occur at 1/4 and 3/4 multiples of the revival time $(2B_0c)^{-1}$. This indicates that a degree of alignment or antialignment is occurring within the ensemble, as some but not all of the phases of the rotational J-states are equal at this time. An 11-point smoothing algorithm has been applied to the integrated data to remove the statistical fluctuations in panel (c). This is an acceptable amount of smoothing for the data, as they are recorded in 1fs time steps using a 12fs pulse. The fine structure of the fractional rotational revivals is revealed without loss of temporal resolution. The 3/4 revival fits the theoretical prediction at an evolution time of 420fs, and the following 1/4 revival at 700fs (after the full revival at 560fs) is also observed from the data.

To put the present results into perspective, the results from another research group [Lee et al., 2006] investigating rotational wave packet revivals in deuterium are shown in Figure 8.5. Key differences are that their study uses the core-annulus optics mentioned

previously instead of a pump-probe method, and uses laser pulses of 10fs duration rather than 12fs. Lee *et al* record their signal using a time step of 20fs, whereas the present results have a greater temporal resolution as 1fs time steps are used. Pump pulses have a peak intensity of 2×10^{14} Wcm^{-2} to reduce ionisation resulting from this pulse and the probe pulse peak intensity is 10^{15} Wcm^{-2}. This is comparable to the peak intensities of $\approx 7\times10^{14}$ Wcm^{-2} in the present study. The polarisation angle of the pump pulse is at $\theta = 0°$ with respect to the probe pulse, so both pulses are aligned along the detector axis. As both pulses have the same polarisation direction, the ensemble is initially aligned at $t = 0$fs, and a peak is observed in the results. As the present results rotate the pump pulse polarisation by $\theta = 90°$ with respect to the probe pulse, the results are inverted with respect to Lee *et al*'s results; where our half revival (at 280fs) consists of a trough followed by a peak, theirs consists of a peak followed by a trough.

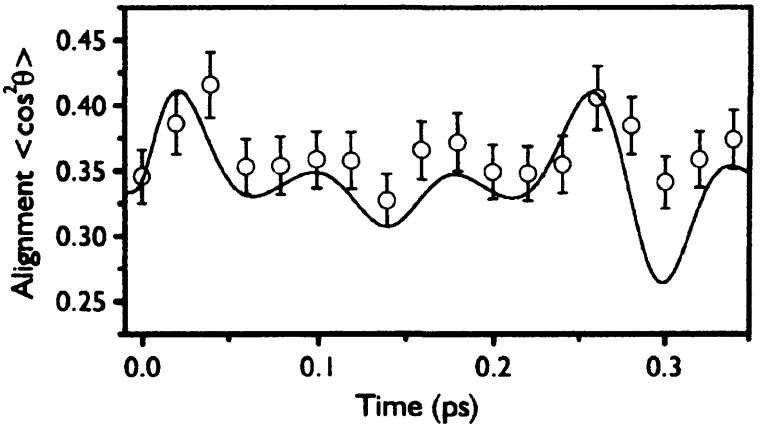

Figure 8.5: Points show the measured alignment of deuterium as a function of time since the peak of the 10fs aligning pulse centred at 0ps. Points higher than 1/3 indicate alignment. The smooth curve is from a numerical simulation of alignment using the experimental parameters. Taken from [Lee et al., 2006] for a comparison with the present results in Figure 8.4(b).

The revival structure is clearly observed in Figure 8.5 up to the first half-revival, however there is a significant discrepancy between the experimental points and the simulation at the longer delay times of $\geq$ 280fs. This could be due to the experimental apparatus, specifically the rotated glass annulus; at long delay times, there may be a considerable thickness of glass in the beam, which could have the effect of lengthening the pulse duration. Hence,

the rotational dynamics are less well resolved at long delay times. In comparison, the present study has an increased temporal resolution and temporal range, allowing Fourier transformation of the results.

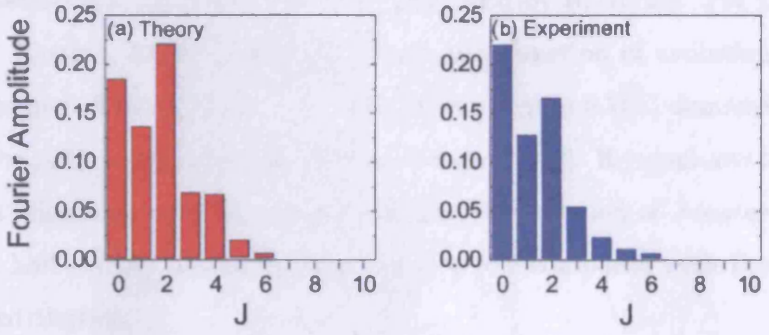

Figure 8.6: Fourier Transform of the (a) theoretical simulation compared with the (b) integrated experimental D^+ ion yield. The frequency components present in the rotational wave packet are beats between rotational states ΔJ and $\Delta J + 2$, i.e. the $J = 0$ amplitude shows the beats for $J = 0$ and $J = 2$. Therefore a measure of the rotational population at 300K is obtained. Adapted from [Bryan et al., 2007].

The integrated ion yield in Figure 8.4(b) is Fourier transformed to recover the frequency components that make up the rotational D_2 wave packet. Figure 8.6 shows histograms of this Fourier transform of the experiment (b), compared with the Fourier transform of the theoretical simulation (red curve in Figure 8.4). As described previously, the D_2 molecule has $\Delta J = 0, \pm 2$ so the beat frequencies shown for each J are beats between rotational levels J and $J+2$. The peak heights are proportional to the product of the quantum amplitudes, and therefore return a measurement of the population of the rotational levels involved. There is a very good agreement between the theoretically predicted beat amplitudes and the experimental results.

8.4.1 Molecular Alignment in D_2

In order to study the rotational dynamics of molecules at different alignment angles, a series of experiments were performed, each with a different pump pulse polarisation angle from 0 to π with respect to the probe pulse. As a result, the axis of revival of the rotational wave packet is rotated with respect to the detector axis. This angular distribution of the

ensemble has been investigated around the first half revival at 280fs and the results have been reflected twice to produce an angular range of $-\pi$ to π. Experimental results are plotted in Figure 8.7(b) as a false colour map or quantum carpet, and are compared with a theoretical simulation (a) which has been performed by R. Torres. For the simulation, the calculated $\langle \cos^2 \theta \rangle$ distribution is displayed as a function of evolution time Δt and polarisation angle θ. The integrated D^+ ion yield in Figure 8.7(b) demonstrates how the ions align to the polarisation direction of the pump pulse (θ). It represents the probability of wave packet alignment averaged over the thermal distribution of J-states that make up the rotational half-revival. As such, it can be directly compared with the simulation of the $\langle \cos^2 \theta \rangle$ distribution.

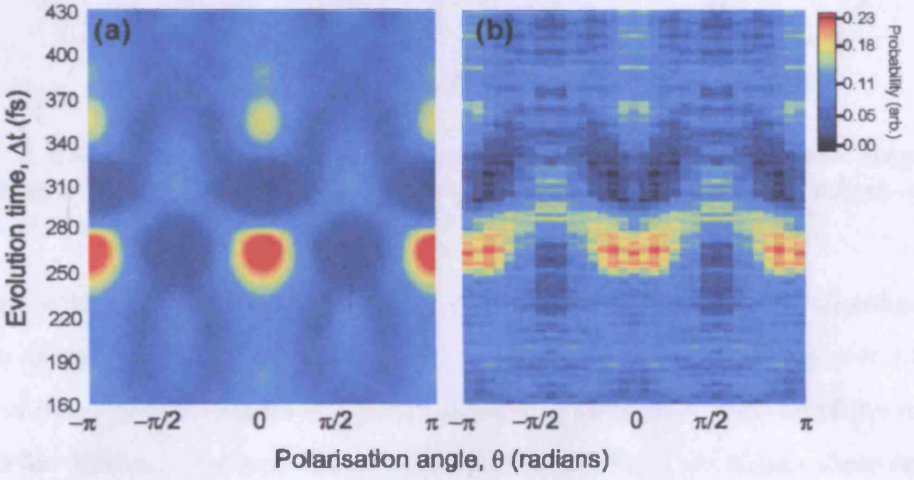

Figure 8.7: (a) Simulated rotation map for an initially random ensemble of room temperature D_2 molecules. For a particular Δt and θ, the false colour scale indicates the wave packet probability with a thermal average. Maximum alignment to the pump polarisation direction is predicted to occur within the range 250fs $\leq \Delta t \leq$ 280fs. (b) Integrated Coulomb explosion D^+ yield (normalised to the theory) obtained for angles 0 to $\pi/2$ over the same range of Δt, and reflected. There is a good agreement between theory and experiment as all the major features are reproduced. Adapted from [Bryan et al., 2007].

Up to an evolution time of ≈200fs, the ensemble in (b) is almost isotropic. At half-revival time (280fs) the characteristic peak and trough modulation structure is visible in the signal. At the start of the revival, the ensemble exhibits a maximum of either alignment (red) or antialignment (dark blue) with the imaging probe pulse, dependent on whether the angle θ is parallel or perpendicular to the detection axis. This is followed

by a strong degree of antialignment or alignment, completing the half-revival. Another small peak/trough is predicted in (a) just after the half-revival, at ≈360fs where a degree of alignment is retained in the ensemble, but some dephasing has occurred. This is also observed in the experimental results, before the ensemble returns to an essentially isotropic distribution again at ≈400fs. Although there is some statistical fluctuation, it is clear that the experimental data in Figure 8.7(b) is in extremely good agreement with theory (a).

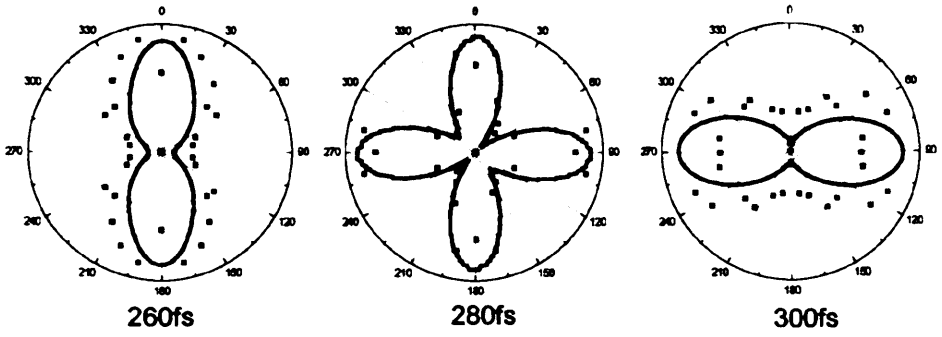

Figure 8.8: The polar plots show the D^+ angular distribution at evolution times within the rotational half-revival. Experimental data is shown as points, and theory as a line. The axis of detection lies along θ=0. The radii are not at the same scale.

A gradual shift in alignment angle is observed, demonstrating that the alignment of the ensemble changes as the angle θ is changed. This change in alignment has been illustrated on a set of polar plots in Figure 8.8, which show the angular distribution of the rotational ensemble for different evolution times within the half-revival. To obtain these snapshots, similar to those shown previously in Figure 8.2, a slice through the quantum carpet data in Figure 8.7 (a) at particular evolution times has been plotted. Slices through the experimental data in (b) have also been used, but an average of slices ±2fs is plotted to minimise the statistical fluctuation occurring in the results.

It can be seen that at 260fs where strong alignment/antialignment occurs within the half-revival, the ensemble forms a double lobed distribution along θ=0°. As the half-revival evolves, this becomes a clover shaped distribution with peaks along θ=0° and θ=90° at 280fs. Although the data appears to pass through an isotropic distribution at this point in Figure 8.7, it can be seen from the angular distribution that a degree of order is maintained by the ensemble. This is also observed in the experimental data points. When the ensemble is antialigned/aligned, the distribution is double lobed again, this time along

θ=90°. There is a good general agreement between the experimental results and predicted theory for these angular distributions.

8.5 Conclusion

This experiment has demonstrated how a rotational wave packet can be created in a neutral D_2 molecular ensemble and mapped using a pump-probe technique. This data shows an improved resolution of the full wave packet revival over a previous study. The J-states involved in the rotational revival have been determined from a Fourier transform of the results. In all results, a good agreement between experiment and theory has been observed. It has also been demonstrated that the direction of alignment of the wave packet can be controlled through the laser polarisation angle of the pump pulse. This ability to control alignment in a field free environment has important implications for high harmonic generation, as the harmonic yield is sensitive to the angle between the molecule and the polarisation direction. Other applications exist in studies of chemical dynamics and surface scattering research [Friedrich and Herschbach, 1995].

Chapter 9

Controlling Recollision in an Elliptically Polarised Laser Field

Presented here is a study of recollision ionisation in Kr^{2+} ions, created from a neutral gas target by a high intensity laser field. A non-Gaussian deconvolution method has been used to remove the inherent focal volume averaging over the laser intensity distribution in the experiment. The ellipticity of the ultrafast (40fs) laser pulses has been varied from linear polarisation to circular, via a series of elliptical polarisations. Accurate removal of the focal volume averaging has allowed the probability of recollision ionisation as a function of intensity and ellipticity to be resolved for the first time. A theoretical simulation has been performed to model the change in the amount of recollision occurring with each ellipticity over a range of intensities. A good agreement has been observed between theory and experiment.

9.1 Introduction

Ultrafast laser interactions with noble gases in the high intensity regime have been the subject of many theoretical and experimental investigations, which have lead to the discovery of highly non-linear phenomena one of which is recollision ionisation. In the recollision

model, an electron is initially tunnel ionised but then returns to the core and causes further ionisation ($e + Kr^{+} \rightarrow Kr^{2+} + 2e$). Recollision produces a signature enhancement of double and multiple ionisation rates compared with the single ionisation rate for gas targets, and is discussed in more detail in Chapter 1.

The trajectory of the recolliding electron is determined by its initial momentum and phase release, and the polarisation of the laser pulse. Control of the electron trajectory is important for high harmonic generation (HHG) whereby an attosecond X-ray pulse is emitted following recombination of the returning electron. Although experiments have been performed using elliptically polarised laser fields e.g. [Dietrich et al., 1994], so far none have performed intensity resolved measurements. This will allow recollision effects to be studied in isolation. In this experimental study, the electron trajectory has been controlled by the polarisation of the laser field while maintaining a constant distribution of sequential ionisation as a function of effective intensity.

9.1.1 Recollision in Elliptically Polarised Light

It is well documented that recollision can occur when the laser field is linearly polarised, but is essentially zero when it is circularly polarised. When the field is linearly polarised, the ionised electron is accelerated away from the core by the electric field, but as the field changes sign for the next half cycle, it can be driven back along its path to the core. However, if the field is circularly polarised, the electron will be deflected from its path by the perpendicular component of the laser field, and be unable to return to the core. Elliptically polarised light is used in this experiment to control the motion of the electron wave packet in the laser field.

As the laser field controls the recolliding electron, the point at which the electron first enters the continuum (the phase of electron release) is also of great importance as this determines the amount of energy gained from the laser field. At the point of recollision, the initial electron must have enough energy to cause secondary ionization. The maximum kinetic energy of an electron recolliding with the core is 3.17 times the Ponderomotive potential ($3.17U_P$) which exists for an electron released at a phase of 17° (Chapter 1).

9.2 Experimental Method

The laser used was the Ti:Sapphire (40fs, 790nm, 10Hz) at the ASTRA Laser Facility (RAL) described in detail in Chapter 3. The 22mm diameter beam is f/11 transmission focused producing a peak intensity of 8×10^{16} Wcm^{-2} in the interaction region of a time-of-flight mass spectrometer (TOFMS) operated in Spatial mode, details of which are given in Chapter 4. The laser field is initially linearly polarised, and is altered by rotation of a quarter-wave plate just before the TOFMS entrance window to produce all elliptical and circular polarisations. Pulse energy was measured using a power meter, and an effective intensity matching technique (section 9.2.1) was employed.

A diffuse target of neutral Kr atoms was ionized in the interaction region of the TOFMS. Gas pressure inside the TOFMS was 3×10^{-8} mbar, low enough to avoid space-charge effects on a background pressure of 4×10^{-10} mbar measured using an ionisation gauge. Ion fragments were extracted from the interaction region by an applied voltage of 300Vcm^{-1}. The ions which passed through the 250μm limiting aperture entered a 110mm field free drift tube, and were detected by a pair of micro-channel plates from which the ion signal was retrieved (Chapter 4).

9.2.1 Intensity Control through Effective Intensity Matching

A combination of two techniques was used to control the intensity in this experiment; Intensity Selective Scanning (ISS) was used to produce results that were highly resolved in intensity (Chapter 5), and an effective intensity matching (EIM) technique maintained a constant sequential ionisation rate throughout the experiment as the polarisation was altered.

For ISS, the 250μm aperture before the TOFMS drift tube limits the spatial acceptance of the spectrometer, so that only a small slice of the laser focus is exposed to the detector. The focusing lens is then moved along the z-axis of the laser beam in sub-mm steps, translating the confocal volume with respect to the aperture. An average over 500 laser shots is taken at each lens position z_f to record the ion signal.

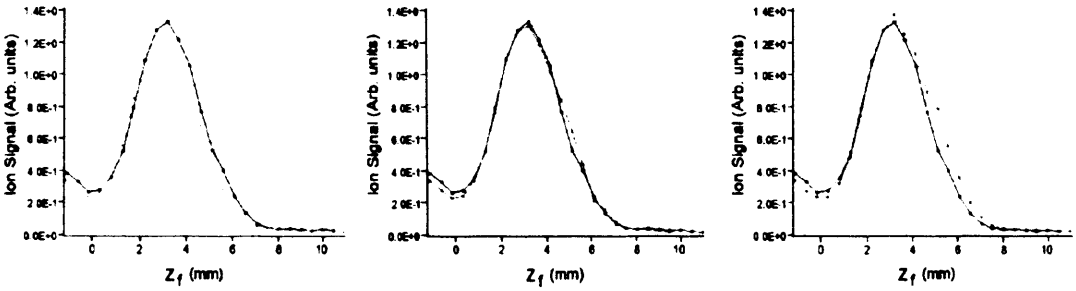

Figure 9.1: In each graph, the ion signal produced with circular polarisation (blue) is matched to that produced by linear polarisation with an intensity reduced by the factor R_{EIM} = 0.6 (red), 0.65 (green), 0.7 (purple).

This method has been combined with the novel experimental technique of effective intensity matching (EIM). The theory of EIM defines a constant ratio (I_{lin}/I_{circ}) as R_{EIM} between the laser intensities of the linearly (I_{lin}) and circularly (I_{circ}) polarised laser beams such that the spatial distribution of the ions detected for each polarisation are the same for all z_f values, assuming that all nonsequential ionisation processes are negligible. Results taken using Neon gas were used to define the ratio R_{EIM}, as it is the least susceptible of the noble gases to nonsequential ionisation.

Ion signal for Ne^+ is shown in Figure 9.1. For each graph, the results taken using a circularly polarised beam at full intensity (I) are compared with those taken with a linearly polarised beam at an intensity reduced by the factor R_{EIM} (0.6I, 0.65I, 0.7I). Negligible recollision effects are observed. The intensity factor which matches the linear ion signal to the circular ion signal is the R_{EIM}, which is observed to be 0.65 (centre graph in Figure 9.1). The linear and circular ion signals were measured consecutively at each lens position z_f for consistency. Intensity was reduced by rotating a half-wave plate in the linearly polarised beam followed by a linear polariser.

A linearly polarised laser field can be thought of as a single plane wave oscillation, so the electric field vector is changing constantly as a function of time, oscillating between a magnitude of 0 and 1 (Figure 9.2). If a quarter-wave plate is inserted at 45°, the laser field will become circularly polarised as it is split into two perpendicular co-linearly propagating plane waves of equal amplitude with a 90° phase difference. As a result, the electric field vector rotates as a function of time, but is constantly present with a magnitude of 0.5.

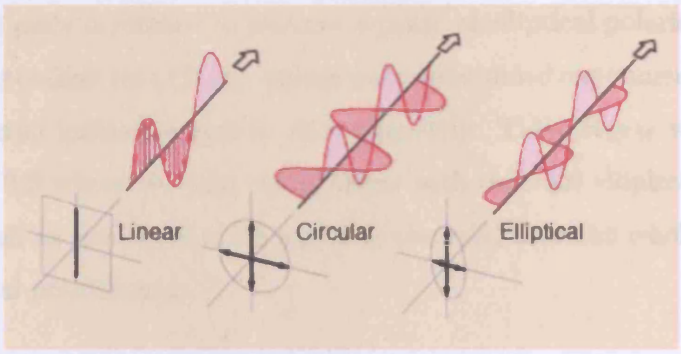

Figure 9.2: Diagram showing linear, elliptical and circular polarisation. Taken from [hyperphysics.phy-astr.gsu.edu] online.

It is generally assumed that the intensity required to generate the circular electric field is twice that required to generate the linear electric field, i.e. $R_{EIM} = 0.5$. However, this does not take into account the fact that the sequential ionisation rate also changes with ellipticity, which must be included in the present experiment. These experiments show that using a factor of $R_{EIM} = 0.65$ for a linearly polarised laser field maintained the same sequential ionisation rate as for circular polarisation. This value has been experimentally tested on a range of other atomic gas targets and was found to be consistent.

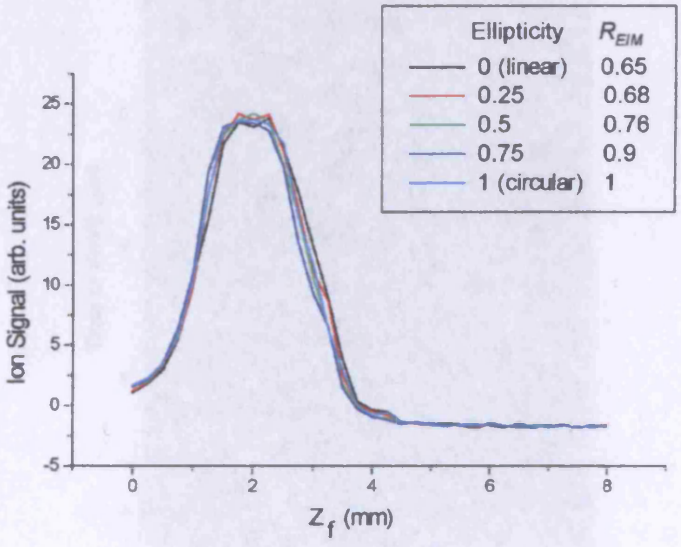

Figure 9.3: Graph showing effective intensity matched intensity selective scans (EIM-ISS) for Ne^+ using different laser ellipticities. A corresponding intensity factor R_{EIM} was used to obtain each experimental curve so that the ion signal produced for each ellipticity is constant.

As a quarter-wave plate is rotated to produce a range of elliptical polarisations in this experiment, a corresponding set of R_{EIM} values were determined experimentally to maintain a constant sequential ionisation rate at each ellipticity. These R_{EIM} values are demonstrated in Figure 9.3 where Ne^+ ion signal taken with different ellipticities is presented. An excellent match to the circular ion signal is observed over the whole range of z_f for linear and elliptical polarisations.

9.3 Results

The raw time-of-flight spectra produced from the Kr neutral gas using linear polarisation with R_{EIM}=0.644 are shown as a function of z_f in Figure 9.4. Up to Kr^{8+} has been detected. All charged states are well resolved due to the ISS technique employed, and the different isotopes of Kr are observable for each state. Such spectra have been obtained for different ellipticities between linear and circular for this experiment, and in each case, a corresponding R_{EIM} factor has been employed.

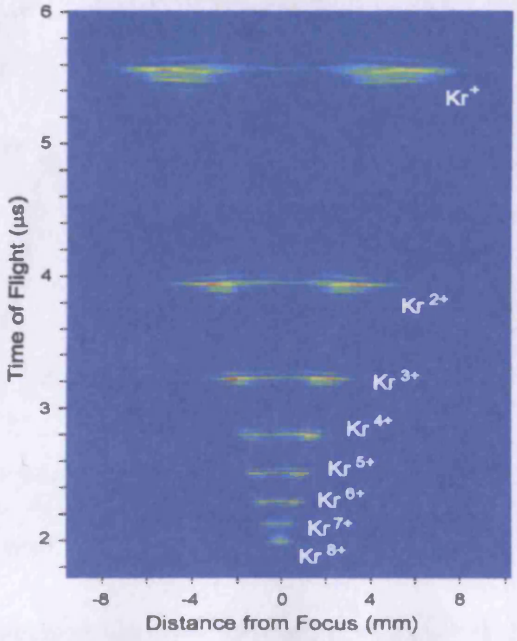

Figure 9.4: Time-of-Flight spectra for Krypton, taken using a linearly polarised laser field. Charged states up to Kr^{8+} are detected.

9.3.1 Recollision in Kr^{2+}

In order to show recollision effects, an integration is performed over the time-of-flight for a particular charged state, producing the graphs shown in Figure 9.5. The ion signal from Kr^{2+} produced from linear, elliptical and circular laser fields can be compared directly as the EIM-ISS technique has been utilized.

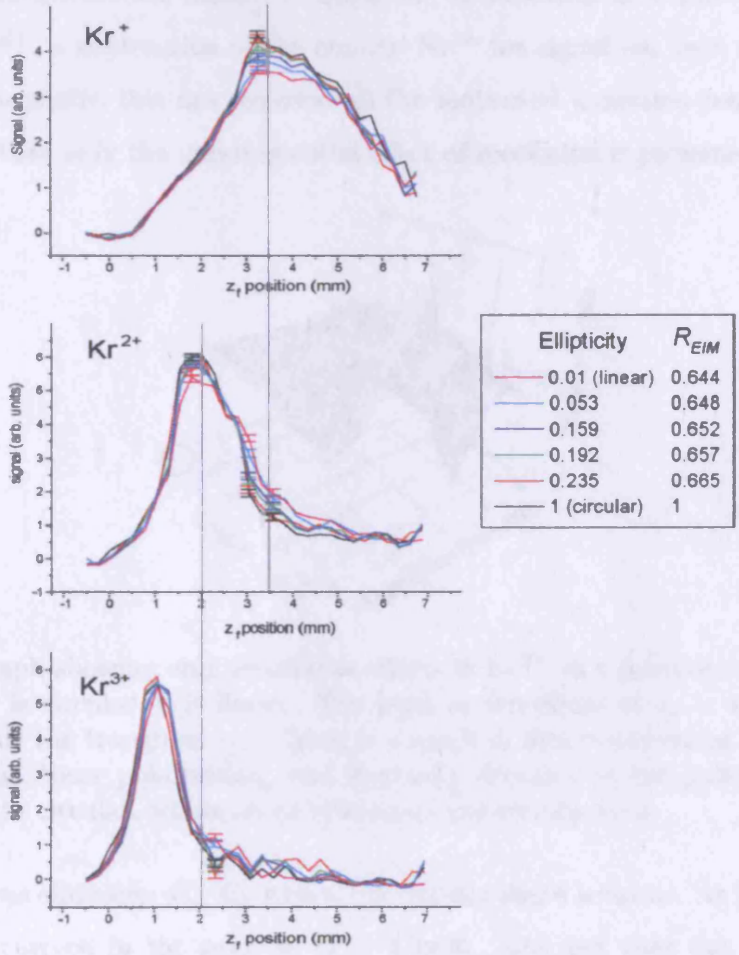

Figure 9.5: Graphs showing integrations of the first three charged states of Krypton produced using different laser polarisation ellipticities. Error bars show the standard deviation of the background noise. See text for discussion.

In Figure 9.5, integrations over the first three charged states of Krypton are shown, each taken using a range of ellipticities with a corresponding R_{EIM}. Recollision effects can be seen in Kr^{2+} as an enhancement in the signal at $3 \leq z_f \leq 6$ mm for the most linear

ellipticities. The vertical line illustrates the flux conservation between charged states; as the detected signal in Kr^{2+} increases due to recollision at a particular z_f, a corresponding decrease is detected in the sequential Kr^{+} signal. Recollision is detected to a lesser degree in the Kr^{3+} charge state at $z_f \approx 2$mm. The vertical line again indicates the decrease in ion signal for Kr^{2+} for flux conservation.

In order to demonstrate the change in signal due to recollision as a function of ellipticity observed in Kr^{2+}, a subtraction of the circular Kr^{2+} ion signal has been performed from all results. Essentially, this has removed all the sequential ionisation contributions from the results, so that only the non-sequential effect of recollision is presented in Figure 9.6.

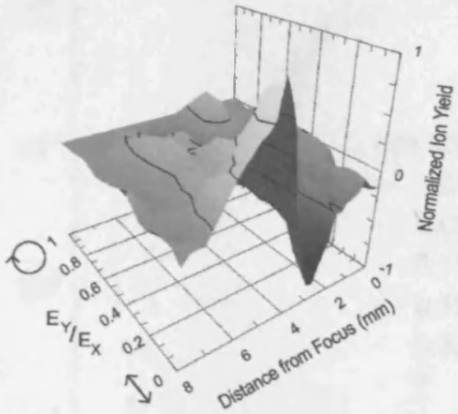

Figure 9.6: Graph showing only recollision effects in Kr^{2+} as a function of ellipticity and z_f position. 1 is circular, 0 is linear. The peak in the signal at $z_f = 4.5$mm is due to recollision, while the trough at $z_f = 3$mm is a result of flux conservation. These features are enhanced at linear polarisation, and gradually decrease as the polarisation changes from elliptical to circular, where no recollision effects are observed.

The y-axis shows ellipticity E_y/E_x where 1 is circular and 0 is linear. At $y = 0$ maximum recollision is observed in the peak at $z_f = 4.5$mm. The fact that this peak occurs at relatively high z_f also indicates that the nonsequential production of Kr^{2+} reaches a maximum at an intensity lower than saturation, as ionisation of Kr^{2+} is saturated ($\geq 2 \times 10^{15}$ Wcm^{-2}) in the region $0 \leq z_f \leq 3$mm. The trough at 3mm is due to an increase in Kr^{3+} produced by recollision ($e + Kr^{2+} \rightarrow Kr^{3+} + 3e$), where a corresponding reduction in sequential production of Kr^{2+} is detected.

For a quantitative analysis of these results, the geometry dependence of the ionisation

yields must be removed. The traditional method to perform this deconvolution is described in [Walker et al., 1998], however this method removes only the volume effects due to a focused Gaussian pulse. Although the Ti:Sapphire laser generates pulses with a Gaussian profile in the far field, optics transporting the beam into the TOFMS interaction region will cause truncation of the beam, resulting in a non-Gaussian intensity distribution at the focus. An alternative model has been used [Bryan et al., 2006b], which accounts for these apertures, described in detail in Chapter 5. Figure 9.7 shows the Kr^{2+} ion signal deconvoluted using this model, resulting in the probability of ionisation as a function of laser intensity.

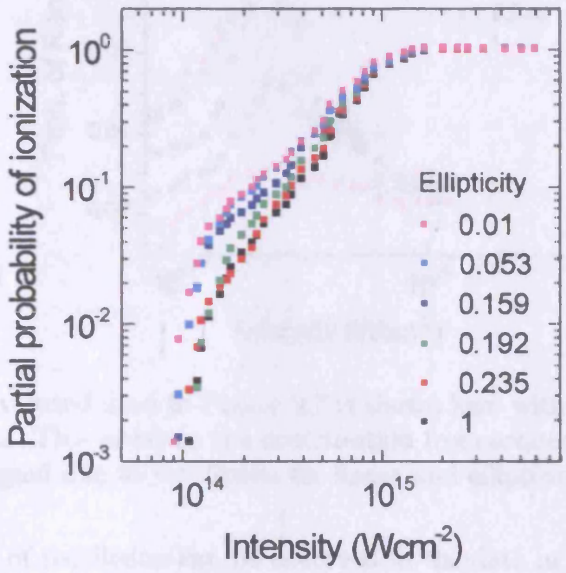

Figure 9.7: Deconvoluted Kr^{2+} ion signal as a function of laser intensity. The deconvolution includes calculations for a laser focal volume with a non-Gaussian distribution (Chapter 5). The signature increase in ionisation due to recollision is evident in the region of 10^{14} to 10^{15} Wcm^{-2}.

In Figure 9.7, the classic signature of recollision is seen in the shoulder-like feature in the region of 10^{14} to 10^{15} Wcm^{-2}. The shoulder is most pronounced for the linear curve (pink line). It can be seen that recollision occurs only for ellipticities very close to linear polarization, and has decreased to a negligible amount once the ellipticity reaches 0.235. This suggests that only a small perpendicular electric field is required to deflect the returning electron wave packet form the core, preventing recollision.

In order to isolate the amount of signal produced by recollision (as shown previously in Figure 9.6), the ionisation probability for circular polarisation which is purely due to sequential ionisation is subtracted from all the results in Figure 9.7. However, now all focal volume effects have been removed so this data is a direct indication of ionisation due to the recollision process ($e + Kr^{+} \rightarrow Kr^{2+} + 2e$). This is shown in Figure 9.8 for the range of ellipticities.

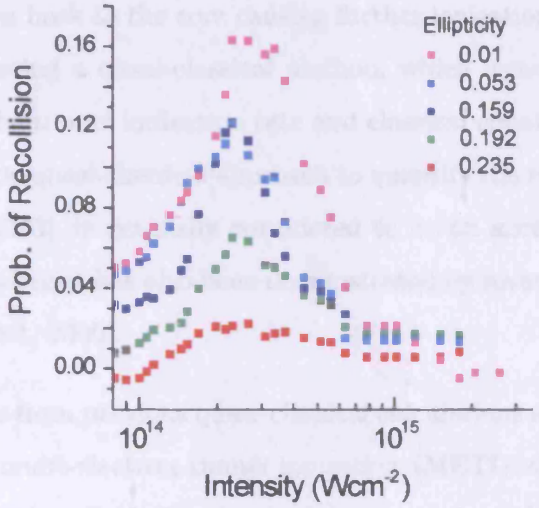

Figure 9.8: The deconvoluted data in Figure 9.7 is shown here with the circular data subtracted from all results. This removes the contribution from sequential tunnel ionisation, leaving only the ion signal due to recollision for linear and elliptical polarisations.

A peak in the amount of recollision can be observed in the data in Figure 9.8 around the intensity region of 2.5 $\times 10^{14}$ Wcm^{-2} for all ellipticities. As the intensity is increased the amount of recollision observed drops, until recollision dies off completely at the saturation intensity of 2 $\times 10^{15}$. At intensities below 2.5 $\times 10^{14}$ Wcm^{-2} the amount of recollision decreases but does not die off completely as in the high intensity case. The experimental intensity range does not extend below 8 $\times 10^{13}$ Wcm^{-2} as the ion signal becomes lost in the background signal at these intensities, as can be seen from the Kr^{2+} ion signal at $z_f \geq 6$ in Figure 9.5.

9.4 Simulation of Recollision in Kr^{2+}

A simulation of recollision effects in Kr^{2+} has been performed to clarify the results obtained in section 9.3.1. Recollision is usually described in terms of the three-step model (Chapter 1), where the electron is initially ionised by the laser field in the first step, the free electron propagation is controlled by the laser field in the second step, and in the third step the electron is driven back to the core causing further ionisation. This process can be theoretically simulated using a quasi-classical method, which incorporates quantum mechanical calculation of the tunnel ionisation rate and classical equations of motion for the electron propagation. The quasi-classical approach to quantify the recollision process, first proposed by [Corkum, 1993], is generally considered to be an accurate method. A fully quantum mechanical treatment has also been demonstrated by several research groups e.g. [van der Hart and Burnett, 2000].

The present model differs from previous quasi-classical calculations as the tunnel ionisation rate used here includes multi-electron tunnel ionisation (METI) effects (Chapter 6), i.e. this model also considers the effect of excitation of the remaining bound electrons during the tunnel ionisation stage to Kr^{+}. This study is the first direct measurement of the change in recollision effects with ellipticity.

9.4.1 Calculating the Electron Trajectories

The starting point for the calculation was a 40fs 800nm laser pulse with a Gaussian intensity profile. Atomic units are used throughout unless otherwise stated. As linear, elliptical and circular laser polarisations must be included, the E_x and E_y components of the laser electric field ε were calculated:

$$E_x(t) = \varepsilon_0 \cos \omega t \tag{9.1}$$

and

$$E_y(t) = \xi \varepsilon_0 \sin \omega t \tag{9.2}$$

where ω is the laser frequency, ε_0 is the peak electric field and ξ is the polarisation ellipticity, which takes values between 0 (linear) and 1 (circular). E_x and E_y are then multiplied by a Gaussian temporal profile $\varepsilon(t)$, calculated for a laser pulse of FWHM (t_p) 40fs:

$$\varepsilon(t) = \frac{1}{2}\varepsilon_0 e^{-(t/t_p)^2} \tag{9.3}$$

The E_x and E_y components of the laser field are then resolved to produce a laser pulse of the required ellipticity ξ, and multiplied by R_{EIM}. There are 3200 points creating the electric field oscillation of this pulse.

To calculate the tunnel ionisation rate of Kr^+, the calculations by Kornev [Kornev et al., 2003] described in Chapter 6 are used. The ionisation rate is determined at every point of the electric field oscillation. As the factor R_{EIM} has been included, the ionisation rate calculated here is the same for linear, elliptical or circular polarisation. Probability of ionisation as a function of laser intensity is shown in Figure 9.9. From this, the number of electrons produced at each point along the laser pulse can be determined.

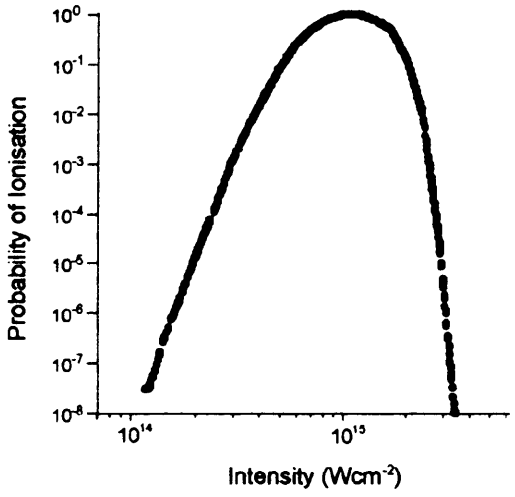

Figure 9.9: Ionisation rate calculated over the intensity range of one laser pulse. For details of the METI rate calculation see Chapter 6.

The trajectory of a single ionised electron in the laser field was calculated using Newton's equations of motion. The initial energy of the electron was assumed to be zero (Chapter 1) immediately after tunnel ionisation. Recollision was assumed to take place on the first pass of the nucleus, and therefore the time window for the electron propagation in the field

was 2fs. This is justified as one half cycle of the laser pulse takes ≈1.3fs. The velocity of the electron was determined from:

$$v_f = v_i + at \tag{9.4}$$

where v_i is the initial velocity and v_f is the final velocity of the electron. The acceleration a is provided solely from the laser field as $F = ma$ where $F = qE$, and is therefore equivalent to the magnitude of the electric field in each direction E_x, E_y (as m and q are the mass and charge of the electron respectively). Equation 9.4 is iterated 200 times, where each time step t=0.01fs.

From the velocity, the distance s travelled by the electron in this time can be calculated from:

$$s = \frac{1}{2}(v_i + v_f)t \tag{9.5}$$

which is also iterated for 2fs to produce an electron trajectory during this time. As the phase of electron release plays a key role in its subsequent trajectory, this 2fs trajectory calculation is repeated for an electron released at any of the 3200 points which make up the oscillating electric field of the laser pulse. An example of a calculated trajectory for an electron released near the peak of a linearly polarised laser field at a phase of 17° is shown in Figure 9.10(a). The point of recollision occurs where the trajectory crosses the y=0 axis. The x and y components of the trajectory have been separately calculated and then resolved.

The kinetic energy E of the electron is calculated for every point along the trajectory from the electron velocity v:

$$E = \frac{1}{2}mv^2 \tag{9.6}$$

A graph of the electron energy during its trajectory in the linearly polarised laser field is shown in 9.10(b). The energy gained from the field first peaks at 0.5fs, as the electron is being driven away from the core. At the point where the laser field reverses, the electron trajectory is reversed (0.9fs) and subsequently the electron energy is zero. The field then drives the electron trajectory back towards the core, and the electron energy increases.

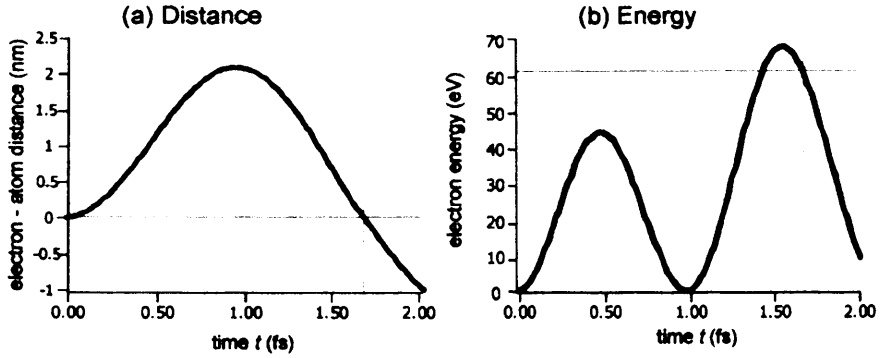

Figure 9.10: (a) Calculated electron trajectory for an electron released at a phase of 17° of a linearly polarised laser field oscillation. Recollision occurs when the graph crosses the y=0 axis (b) Corresponding electron energy gained by the electron during its trajectory.

It can be seen that at the point of recollision (1.7fs) the electron has gained a significant amount of energy from the field. This Ponderomotive energy of $3.17U_P$ is 62 eV, gained from a laser field intensity of 3.35×10^{14} Wcm^{-2}. As the ionisation potential I_P of the Kr^2+ ion is 24.359 eV, this particular returning electron is able to cause recollision.

Two conditions are defined for recollision; (i) the electron must return to a distance $\leq$ 2.8 a.u. of the ion and (ii) the electron must have sufficient energy to cause further ionisation, i.e. $E \geq$ 24.359 eV. The first condition is derived from the Hartree radial function for a $4p$ electron orbital, shown in Figure 9.11. The FWHM of the main peak of this distribution is in the region of 1 to 2.8 a.u. so there is a significant probability of Kr^{2+} ionisation if the returning electron trajectory passes within 2.8 a.u. of the core. The second condition results from the I_P of the Kr^{2+} ion. If these conditions are satisfied then recollision ionisation will occur.

It is clear that satisfying the first condition will become increasingly difficult as the ellipticity of the laser field increases from $\xi = 0$ (linear) to $\xi = 1$ (circular). This is because the E_y component of the field increases with ξ, and acts to deflect the returning electron from the core. As a result, recollision is highly dependent on the laser field ellipticity.

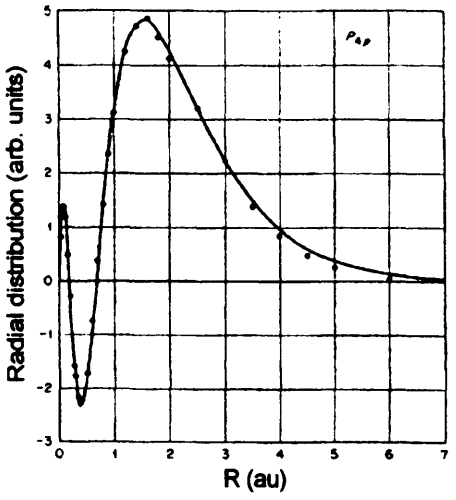

Figure 9.11: Hartree radial function (curve) with analytical calculation (points) for a $4p$ electron orbital. Taken from [Green, 1957].

9.4.2 Quantifying Recollision

Now that it has been established if the returning electron will recollide or not, the amount of Kr^{2+} ionisation produced through recollision must be determined. An electron-impact single-ionisation cross section of the Kr^{+} ion, which has been experimentally obtained by [Man et al., 1987] is employed to quantify the amount of recollision. This cross section as a function of electron energy is shown in Figure 9.12. Each of the recolliding electrons calculated in section 9.4.1 of a particular energy are multiplied by the cross section at that energy, producing a measure of the recollision ionisation produced.

Multiplying the cross section in Figure 9.12 by the number of recolliding electrons yields the amount of recollision produced as a function of electron energy for a particular laser intensity. This is shown in Figure 9.13 for each different ellipticity. for an intensity of 2×10^{15} Wcm^{-2}. The ellipticities used in the model are the same as those used in the experiment.

This result shows how the amount of recollision decreases as the polarisation becomes more elliptical. It can be seen from Figure 9.13 that the highest energy electrons ($\geq$400 eV) only contribute towards recollision if the polarisation is linear. There is also a general decrease in the amount of recollision at lower energies (25 eV to 100 eV) as ellipticity

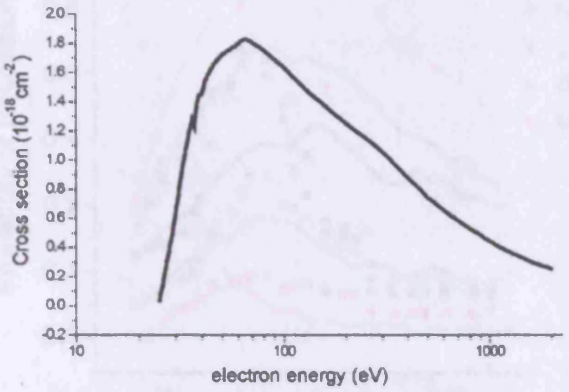

Figure 9.12: Experimental electron-impact single-ionisation cross section for Kr^+. The values here have been shown to agree with other experimental studies as well as configuration-average distorted-wave calculations in [Loch et al., 2002]. Taken from [Man et al., 1987].

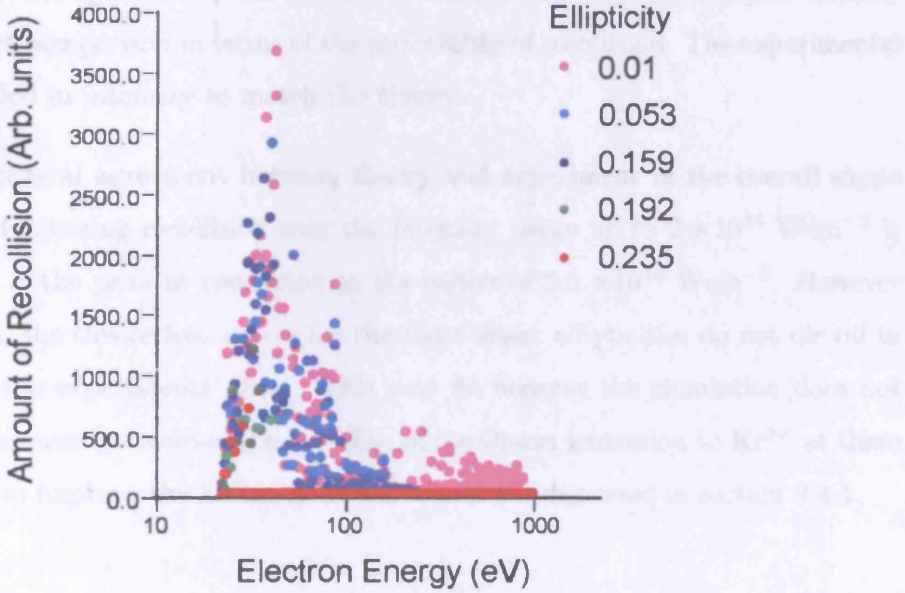

Figure 9.13: The number of recolliding electrons has been multiplied by the cross section in Figure 9.12(b) to find the amount of recollision produced as a function of electron energy for each ellipticity. Laser intensity is 2×10^{15} Wcm^{-2}.

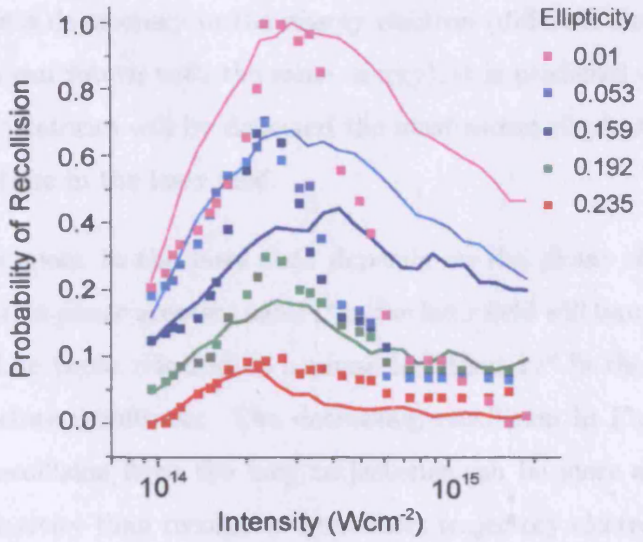

Figure 9.14: Comparison between theoretical (curves) and experimental (points) results. Recollision for a range of ellipticities is shown as a function of intensity. The experimental data is the same as Figure 9.8, which has been scaled in intensity to match the theory.

a curve, and is compared with the experimental points for each ellipticity over the full intensity range. Both experimental and theoretical results have been normailised to unity to allow for a direct comparison in terms of the probability of recollision. The experimental data has been scaled in intensity to match the theory.

There is a good general agreement between theory and experiment in the overall shape of the data. The increasing recollision over the intensity range up to 2 $\times 10^{14}$ Wcm^{-2} is well predicted, as is the peak in recollision in the region of 2.5 $\times 10^{14}$ Wcm^{-2}. However at high intensities, the theoretical curves for the most linear ellipticities do not die off in the same way as the experimental data. This may be because the simulation does not calculate and subsequently remove all possibility of recollision ionisation to Kr^{3+} at these intensities. Ways to improve the accuracy of this model are discussed in section 9.4.4.

9.4.4 Future Improvements to the Simulation

There are evidently areas in this model which could be improved, leading to a better agreement with the experimental data. A significant omission is the spread of the electron

increases. As there is a degeneracy in the energy electron (different electrons with short and long trajectories can return with the same energy), it is predicted that the electrons which have longer trajectories will be deflected the most as the ellipticity is increased, as they spend a longer time in the laser field.

The amount of time spent in the laser field depends on the phase of electron release. Electrons released with a phase greater than 17° in the laser field will have a long trajectory in the laser field, while those released at a phase less than 17° in the field will have a shorter trajectory before recollision. The decreasing recollision in Figure 9.13 may be an indication that recollision from the long trajectories can be more easily switched off by increasing the ellipticity than recollision from short trajectory electrons, although this must first be experimentally verified. This is potentially an important result, which could be implemented for the control of HHG in the future; the harmonics resulting from the long trajectories could be switched off leaving only the harmonics from the short trajectories, by changing the ellipticity. This would remove the degeneracy in energy resulting from long and short trajectories, and may permit the selection of harmonics of a particular energy.

9.4.3 Comparison with Experimental Results

The theoretical results obtained so far have been interesting, but have not yet been directly compared with the experimentally obtained data. To perform the simulation it was necessary to calculate the amount of recollision as a function of electron energy. It is not possible to determine the energies of the electrons produced in the TOFMS as it does not contain an electron spectrometer; only the ion signal is measured. The ion signal due to recollision was shown in Figure 9.8 with all sequential contributions removed, and this data will now be compared with the simulation.

In order to compare the results from the simulation with the experimental results, the calculated amount of recollision must be summed over the range of electron energies to produce a single value for recollision at a particular intensity. This summation of recollision over all electron energies associated with a particular intensity is shown in Figure 9.14 as

wave packet once it has been ionised. This can be calculated as a Gaussian spread of the initial electron wave packet width. The inclusion of this spread may lead to an increase in the amount of recollision, as it will increase the area of the orbital in Figure 9.11 over which recollision is possible.

The range over which recollision can occur could also be extended over the whole of the orbital, rather than be confined within the FWHM as in the present calculations. Incorporating the $4s$ and $3d$ orbital distributions in addition to the $4p$ would fill in the region between $0 \leq R \leq 1$ in Figure 9.11, which may improve the model for the most linear polarisations.

An improved calculation of Kr^{2+} recollision occurring at high intensity may require a full calculation of recollision in Kr^{3+}, which can then be subtracted from the Kr^{2+} results. The Kr^{3+} production, which could be generated by high energy electrons, may be responsible for the recollision occurring in the region of saturation (2×10^{15} Wcm^{-2}), as the experimental results show recollision dying off at this point.

Also, the fact that experimental cross sections have been used may account for some inaccuracy in the results. The nature of the experiment in [Man et al., 1987], where a 4keV beam of Kr^{+} ions was crossed with an electron beam, means that an infinite number of impact parameters have been averaged over in these results. In the present experiment, the impact parameter is defined by the ellipticity, and will therefore have only a small range. As a result of this difference in impact parameters, the amount of recollision predicted by the model may be higher than that observed in the experiment. Theoretical calculations of the Kr^{+} cross section for a smaller range of impact parameters may exist, which could replace the experimentally obtained cross sections for more accurate results.

9.5 Conclusion

Experimental and theoretical results for recollision ionisation in Kr^{2+} using an elliptically polarised laser field have been presented. A good agreement has been observed, and some future changes have been proposed to improve the theoretical simulation. This is the first

direct measurement of recollision ionisation as a function of the ellipticity of the laser. All focal volume and diffraction effects have been removed from the experimental data. Experimental results have been quantified by a quasi-classical simulation which has also generated the amount of recollision produced as a function of electron energy. As well as providing a deeper insight into the recollision process, this work is of importance to the field of attosecond physics, where a complete knowledge of the ellipticity at which recollision is suppressed is useful when switching on and off the harmonic generation using a polarisation gating technique [Sola et al., 2006].

Chapter 10

Future Outlook

The research presented in this thesis has spanned a variety of topics within the fields of femtosecond laser physics and the dynamics of atoms and small molecules, and paving the way for exciting new research in the future. The most obvious way forward for short laser pulse interactions lies towards the attosecond regime, where xuv pulses down to 100as have already been produced through high harmonic generation. This requires the generation of phase stabilised laser pulses of 5fs duration. Attosecond pulses will permit extremely high resolution measurement of the dynamics of hydrogenic molecules, and even allow dynamical electron processes such as tunnelling to be resolved.

In order to detect such mechanisms. the time-of-flight spectrometers used for the present experiments will require the addition of position sensitive detectors. A kinematically complete detection system including an electron spectrometer to detect the electrons in coincidence with the ions (such as COLTRIMS) would be a long term prospect.

With respect to the vibrational pump-probe experiments, cooling the molecules will enable selective population of the lowest vibrational states, which is key for applications such as quantum computing. For future experiments examining the rotation of molecules, the application of a third control pulse will extend the degree of control over molecular dynamics demonstrated here.

The new deconvolution technique to remove all diffraction effects as well as the focal volume from ISS results can be applied to future experiments as a standard technique. This will yield more accurate intensity dependent ionisation rates, especially in experiments performed with few cycle pulses.

A number of future improvements have already been proposed for the simulation of recollision in Chapter 9. An increase in the precision of this model will lead to a greater understanding of the recollision process and subsequently benefit research into the generation of high harmonics. This also has significant implications for the field of attosecond physics.

Appendix A

Research Publications

A.1 Refereed Publications

- E M L English, W A Bryan, J Wood, J McKenna, W R Newell, I D Williams and I C E Turcu. Precise trajectory control of electron recollision with elliptical polarization. In preparation.

- W A Bryan, J McKenna, E M L English, J Wood, C R Calvert, R Torres, I C E Turcu, J L Collier, I D Williams and W R Newell. Ultrafast vibrational wavepackets in D_2^+: Defining superposition conditions and wavepacket distinguishability. Submitted to Phys. Rev. Lett.

- I D Williams, J McKenna, J Wood, M Suresh, W A Bryan, S L Stebbings, E M L English, C R Calvert, B Srigengan, I C E Turcu, J L Collier, and W R Newell, Excited ions in intense ultrafast laser pulses: laser induced recombination. Submitted to Phys. Rev. Lett.

- J McKenna, W A Bryan, C R Calvert, E M L English, J Wood, D S Murphy, I C E Turcu, J M Smith, K G Ertel , O Chekhlov, E J Divall, J F McCann, W R Newell and I D Williams. Observing time-dependent vibrational quantum dynamics in deuterium hydride molecular ions. *J. Mod. Opt.* 54 7 1127 (2007).

- D S Murphy, J McKenna, C R Calvert, W A Bryan, E M L English, J Wood, I C E Turcu, W R Newell, I D Williams and J F McCann. Controlling dissociation processes in the D2+ molecular ion using high-intensity, ultrashort laser pulses. *J. Phys. B: At. Mol. Opt. Phys.* 40 S359-S372 (2007).

- W A Bryan, E M L English, J McKenna, J Wood, C R Calvert, R Torres, I C E Turcu, J L Collier, I D Williams and W R Newell, Mapping the evolution of optically-generated rotational wavepackets in a room temperature ensemble of D_2. *Phys. Rev. A*, 76 023414 (2007).

- W A Bryan, S L Stebbings, E M L English, T R J Goodworth, WR Newell, J McKenna, M Suresh, B Srigengan, I D Williams, I C E Turcu, J M Smith, E J Divall, C J Hooker, and A J Langley. Geometry- and diffraction-independent ionization probabilities in intense laser fields: Probing atomic ionization mechanisms with effective intensity matching. *Phys. Rev. A*, 73 013407 (2006).

- W A Bryan, S L Stebbings, J McKenna, E M L English, M Suresh, J Wood, B Srigengan, I C E Turcu, J M Smith, E J Divall, C J Hooker, A J Langley, J L Collier, I D Williams and W R Newell. Atomic excitation during recollision-free ultrafast multi-electron tunnel ionization *Nature Physics* 2 379 (2006).

- W A Bryan, S L Stebbings, J McKenna, E M L English, M Suresh, J Wood, B Srigengan, I C E Turcu, I D Williams and W R Newell. On the recollision-free excitation of krypton during ultrafast multi-electron tunnel ionization, *J Phys B: At. Mol. Opt. Phys.* 39 S349 (2006).

- J McKenna, M Suresh, B Srigengan, I D Williams, W A Bryan, E M L English, S L Stebbings, W R Newell, I C E Turcu, J M Smith, E J Divall, C J Hooker, A J Langley and J L Collier. Rescattering enhanced dissociation of a molecular ion. *Phys. Rev. A* 74 043409 (2006).

- J McKenna, M Suresh, B Srigengan, I D Williams, W A Bryan, E M L English, S L Stebbings, W R Newell, I C E Turcu, J M Smith, E J Divall, C J Hooker, A J Langley and J L Collier. Ultrafast ionization study of N2 in intense linearly and circularly polarized laser fields. *Phys. Rev. A* 73 043401 (2006).

- M Suresh, J McKenna, B Srigengan, I D Williams, E M L English, S L Stebbings, W A Bryan, W R Newell, E J Divall, C J Hooker and A J Langley. Multiple ionization of ions and atoms by intense ultrafast laser pulses. *Nucl. Inst. and Meth. B*, 235 216 (2005)

A.2 Conference Poster Presentations

- Imaging the vibrational motion of D_2^+ molecular ions with ultrashort laser pulses International Conference on Quantum, Atomic and Molecular Physics, University College London, UK (2007).
- *Precise trajectory control of electron recollision with elliptical polarization.* International Conference on Attosecond Physics, Dresden, Germany (2007).
- *Precise trajectory control of electron recollision with elliptical polarization.* 25th International Conference on Photonic, Electronic and Atomic Collisions, Freiburg, Germany (2007).
- *Direct observation of sub-vibrational-period nuclear dynamics in H_2, D_2 and HD.* Attosecond Meeting, Imperial College London, UK (2006).
- *Controlling non-sequential double ionisation using elliptically polarised ultrafast laser pulses.* 10th International Conference on Multiphoton Processes, Quebec, Canada (2005).

Bibliography

[Agostini et al., 1979] Agostini, P., Fabre, F., Mainfray, G., Petite, G., and Rahman, N. K. (1979). Free-free transitions following six-photon ionization of xenon atoms. *Phys. Rev. Lett.*, 42(17):1127–1130.

[Agrawal, 2001] Agrawal, G. P. (2001). *Nonlinear Fiber Optics.* Academic Press, San Diego, USA.

[Alnaser et al., 2005] Alnaser, A. S., Maharjan, C. M., Tong, X. M., Ulrich, B., Ranitovic, P., Shan, B., Chang, Z., Lin, C. D., Cocke, C. L., and Litvinyuk, I. V. (2005). Effects of orbital symmetries in dissociative ionization of molecules by few-cycle laser pulses. *Physical Review A (Atomic, Molecular, and Optical Physics)*, 71(3):031403.

[Alnaser et al., 2004] Alnaser, A. S., Tong, X. M., Osipov, T., Voss, S., Maharjan, C. M., Ranitovic, P., Ulrich, B., Shan, B., Chang, Z., Lin, C. D., and Cocke, C. L. (2004). Routes to control of h_2 coulomb explosion in few-cycle laser pulses. *Physical Review Letters*, 93(18):183202.

[Ammosov et al., 1986] Ammosov, M. V., Delone, N. B., and Krainov, V. P. (1986). Tunnel ionization of complex atoms and of atomic ions in an alternating electromagnetic field. *Sov. Phys. JETP*, 1(64):1191.

[Auguste et al., 1992] Auguste, T., Monot, P., Lompre, L. A., Mainfray, G., and Manus, C. (1992). Multiply charged ions produced in noble gases by a 1 ps laser pulse at lambda =1053 nm. *Journal of Physics B: Atomic, Molecular and Optical Physics*, 25(20):4181–4194.

[Backus et al., 1997] Backus, S., Durfee, C. G., Murnane, M. M., and Kapteyn, H. C. (1997). High power ultrafast lasers. *Review of Scientific Instruments*, 69(3):1207.

[Baker et al., 2006] Baker, S., Robinson, J. S., Haworth, C. A., Teng, H., Smith, R. A., Chirila, C. C., Lein, M., Tisch, J. W. G., and Marangos, J. P. (2006). Probing proton dynamics in molecules on an attosecond time scale. *Science*, 312(5772):424–427.

[Becker and Faisal, 2002] Becker, A. and Faisal, F. H. M. (2002). *s*-matrix analysis of coincident measurement of two-electron energy distribution for double ionization of he in an intense laser field. *Phys. Rev. Lett.*, 89(19):193003.

[Becker and Faisal, 2005] Becker, A. and Faisal, F. H. M. (2005). Intense-field many-body s-matrix theory. *Journal of Physics B: Atomic, Molecular and Optical Physics*, 38(3):R1–R56.

[Brabec and Krausz, 2000] Brabec, T. and Krausz, F. (2000). Intense few-cycle laser fields: Frontiers of nonlinear optics. *Rev. Mod. Phys.*, 72(2):545–591.

[Bryan, 2001] Bryan, W. A. (2001). *Ultrafast processes in small molecules.* PhD thesis, University College London, Department of Physics and Astronomy, University College London, England.

[Bryan et al., 2007] Bryan, W. A., English, E. M. L., McKenna, J., Wood, J., Calvert, C. R., Turcu, I. C. E., Torres, R., Collier, J. L., Williams, I. D., and Newell, W. R. (2007). Mapping the evolution of optically generated rotational wave packets in a room-temperature ensemble of d_2. *Physical Review A (Atomic, Molecular, and Optical Physics)*, 76(2):023414.

[Bryan et al., 2006a] Bryan, W. A., Newell, W. R., Sanderson, J. H., and Langley, A. J. (2006a). Observation of multiple ionization pathways for ocs in an intense laser field resolved by three-dimensional covariance mapping and visualized by hierarchical ionization topology. *Physical Review A (Atomic, Molecular, and Optical Physics)*, 74(5):053409.

[Bryan et al., 2006b] Bryan, W. A., Stebbings, S. L., English, E. M. L., Goodworth, T. R. J., Newell, W. R., McKenna, J., Suresh, M., Srigengan, B., Williams, I. D.,

Turcu, I. C. E., Smith, J. M., Divall, E. J., Hooker, C. J., and Langley, A. J. (2006b). Geometry- and diffraction-independent ionization probabilities in intense laser fields: Probing atomic ionization mechanisms with effective intensity matching. *Physical Review A (Atomic, Molecular, and Optical Physics)*, 73(1):013407.

[Bryan et al., 2006c] Bryan, W. A., Stebbings, S. L., McKenna, J., English, E. M. L., Suresh, M., Wood, J., Srigengan, B., Turcu, I. C. E., Smith, J. M., Divall, E. J., Hooker, C. J., Langley, A. J., Williams, J. L. C. I. D., and Newell, W. R. (2006c). Atomic excitation during recollision-free ultrafast multi-electron tunnel ionization. *Nature Physics*, 2(6):379–383.

[Bryan et al., 2006d] Bryan, W. A., Stebbings, S. L., McKenna, J., English, E. M. L., Suresh, M., Wood, J., Srigengan, B., Turcu, I. C. E., Williams, I. D., and Newell, W. R. (2006d). On the recollision-free excitation of krypton during ultrafast multi-electron tunnel ionization. *Journal of Physics B: Atomic, Molecular and Optical Physics*, 39(13):S349–S356.

[Bucksbaum et al., 1990] Bucksbaum, P. H., Zavriyev, A., Muller, H. G., and Schumacher, D. W. (1990). Softening of the h_2^+ molecular bond in intense laser fields. *Phys. Rev. Lett.*, 64(16):1883–1886.

[Carlson et al., 1968] Carlson, T. A., Nestor, C. W., Tucker, T. C., and Malik, F. B. (1968). Calculation of electron shake-off for elements from $z = 2$ to 92 with the use of self-consistent-field wave functions. *Phys. Rev.*, 169(1):27–36.

[Chaloupka et al., 2003] Chaloupka, J. L., Rudati, J., Lafon, R., Agostini, P., Kulander, K. C., and DiMauro, L. F. (2003). Observation of a transition in the dynamics of strong-field double ionization. *Phys. Rev. Lett.*, 90(3):033002.

[Charalambidis et al., 1997] Charalambidis, D., Xenakis, D., Uiterwaal, C. J. G. J., Maragakis, P., Zhang, J., Schroder, H., Faucher, O., and Lambropoulos, P. (1997). Multiphoton ionization saturation intensities and generalized cross sections from ati spectra. *Journal of Physics B: Atomic, Molecular and Optical Physics*, 30(6):1467–1479.

[Chu, 1981] Chu, S.-I. (1981). Floquet theory and complex quasivibrational energy formalism for intense field molecular photodissociation. *The Journal of Chemical Physics*, 75(5):2215–2221.

[Corkum, 1993] Corkum, P. B. (1993). Plasma perspective on strong field multiphoton ionization. *Phys. Rev. Lett.*, 71(13):1994–1997.

[Corkum et al., 1989] Corkum, P. B., Burnett, N. H., and Brunel, F. (1989). Above-threshold ionization in the long-wavelength limit. *Phys. Rev. Lett.*, 62(11):1259–1262.

[Cornaggia et al., 1990] Cornaggia, C., Lavancier, J., Normand, D., Morellec, J., and Liu, H. X. (1990). Intensity dependence of the multielectron dissociative ionization of n_2 at 305 and 610 nm. *Phys. Rev. A*, 42(9):5464–5472.

[Dantus et al., 1987] Dantus, M., Rosker, M. J., and Zewail, A. H. (1987). Real-time femtosecond probing of "transition states" in chemical reactions. *The Journal of Chemical Physics*, 87(4):2395–2397.

[Davies et al., 1999] Davies, J. A., LeClaire, J. E., Continetti, R. E., and Hayden, C. C. (1999). Femtosecond time-resolved photoelectronphotoion coincidence imaging studies of dissociation dynamics. *Journal of Chemical Physics*, 111(1):1–4.

[Dietrich et al., 1994] Dietrich, P., Burnett, N. H., Ivanov, M., and Corkum, P. B. (1994). High-harmonic generation and correlated two-electron multiphoton ionization with elliptically polarized light. *Phys. Rev. A*, 50(5):R3585–R3588.

[Dooley et al., 2003] Dooley, P. W., Litvinyuk, I. V., Lee, K. F., Rayner, D. M., Spanner, M., Villeneuve, D. M., and Corkum, P. B. (2003). Direct imaging of rotational wavepacket dynamics of diatomic molecules. *Phys. Rev. A*, 68(2):023406.

[Dorner et al., 2002] Dorner, R., Weber, T., Weckenbrock, M., Staudte, A., Hattass, M., Moshammer, R., Ullrich, J., and Schmidt-Bocking, H. (2002). Multiple ionization in strong laser fields. *Adv. Atom. Mol. Phys.*, 48(1):1.

[Dubietis et al., 1992] Dubietis, A., Jonuauskas, G., and Piskarskas, A. (1992). Powerful femtosecond pulse generation by chirped and stretched pulse parametric amplification in bbo crystal. *Optics Communications*, 88(4-6):437–440.

[Eberly and Sleeper, 1968] Eberly, J. H. and Sleeper, A. (1968). Trajectory and mass shift of a classical electron in a radiation pulse. *Phys. Rev.*, 176(5):1570–1573.

[Eichmann et al., 2000] Eichmann, U., Dorr, M., Maeda, H., Becker, W., and Sandner, W. (2000). Collective multielectron tunneling ionization in strong fields. *Phys. Rev. Lett.*, 84(16):3550–3553.

[Ergler et al., 2006a] Ergler, T., Feuerstein, B., Rudenko, A., Zrost, K., Schroter, C. D., Moshammer, R., and Ullrich, J. (2006a). Quantum-phase resolved mapping of ground-state vibrational d_2 wave packets via selective depletion in intense laser pulses. *Physical Review Letters*, 97(10):103004.

[Ergler et al., 2006b] Ergler, T., Rudenko, A., Feuerstein, B., Zrost, K., Schroter, C. D., Moshammer, R., and Ullrich, J. (2006b). Spatiotemporal imaging of ultrafast molecular motion: Collapse and revival of the d_2^+ nuclear wave packet. *Physical Review Letters*, 97(19):193001.

[Ergler et al., 2006c] Ergler, T., Rudenko, A., Feuerstein, B., Zrost, K., Schroter, C. D., Moshammer, R., and Ullrich, J. (2006c). Ultrafast mapping of h_2^+ (d_2^+) nuclear wave packets using time-resolved coulomb explosion imaging. *Journal of Physics B Atomic Molecular Physics*, 39:493.

[Fabian et al., 2003] Fabian, C., Kitzler, M., Milosevic, N., and Brabec, T. (2003). Multi-electron strong field theory. *Journal of Modern Optics*, 50(3/4):589–595.

[Fabre et al., 1982] Fabre, F., Petite, G., Agostini, P., and Clement, M. (1982). Multi-photon above-threshold ionisation of xenon at 0.53 and 1.06μm. *Journal of Physics B: Atomic and Molecular Physics*, 15(9):1353–1369.

[Fittinghoff et al., 1992] Fittinghoff, D. N., Bolton, P. R., Chang, B., and Kulander, K. C. (1992). Observation of nonsequential double ionization of helium with optical tunneling. *Phys. Rev. Lett.*, 69(18):2642–2645.

[Frasinski et al., 1987] Frasinski, L. J., Codling, K., Hatherly, P., Barr, J., Ross, I. N., and Toner, W. T. (1987). Femtosecond dynamics of multielectron dissociative ionization by use of a picosecond laser. *Phys. Rev. Lett.*, 58(23):2424–2427.

[Frasinski et al., 1989] Frasinski, L. J., Codling, K., and Hatherly, P. A. (1989). Covariance Mapping: A Correlation Method Applied to Multiphoton Multiple Ionization. *Science*, 246(4933):1029–1031.

[Frasinski et al., 1999] Frasinski, L. J., Posthumus, J. H., Plumridge, J., Codling, K., Taday, P. F., and Langley, A. J. (1999). Manipulation of bond hardening in h_2^+ by chirping of intense femtosecond laser pulses. *Phys. Rev. Lett.*, 83(18):3625–3628.

[Frasinski et al., 1992] Frasinski, L. J., Stankiewicz, M., Hatherly, P. A., Cross, G. M., Codling, K., Langley, A. J., and Shaikh, W. (1992). Molecular h_2 in intense laser fields probed by electron-electron, electron-ion, and ion-ion covariance techniques. *Phys. Rev. A*, 46(11):R6789–R6792.

[Friedrich and Herschbach, 1995] Friedrich, B. and Herschbach, D. (1995). Alignment and trapping of molecules in intense laser fields. *Phys. Rev. Lett.*, 74(23):4623–4626.

[Galvanauskas et al., 1998] Galvanauskas, A., Hariharan, A., Harter, D., Arbore, M. A., and Fejer, M. M. (1998). High-energy femtosecond pulse amlification in a quasi-phase-matched parametric amplifier. *Optics Letters*, 23(3):210–212.

[Giusti-Suzor et al., 1990] Giusti-Suzor, A., He, X., Atabek, O., and Mies, F. H. (1990). Above-threshold dissociation of h_2^+ in intense laser fields. *Phys. Rev. Lett.*, 64(5):515–518.

[Giusti-Suzor and Mies, 1992] Giusti-Suzor, A. and Mies, F. H. (1992). Vibrational trapping and suppression of dissociation in intense laser fields. *Phys. Rev. Lett.*, 68(26):3869–3872.

[Goeppert-Mayer, 1931] Goeppert-Mayer, M. (1931). Elementary processes with two quantum jumps. *Ann. der Phys. (Leipzig)*, 1(9):273.

[Goodworth, 2002] Goodworth, T. R. J. (2002). *Dynamics of atoms, molecules and ions in intense laser fields.* PhD thesis, University College London, Department of Physics and Astronomy, University College London, England.

[Green, 1957] Green. A. E. S. (1957). Single electron shakeoff probability following the beta decay of krypton. *Phys. Rev.*, 107(6):1646–1650.

[Gubbini et al., 2006] Gubbini, E., Eichmann, U., Kalashnikov, M., and Sandner, W. (2006). Multiple ionization of kr in an intense circularly polarized laser field. *Journal of Physics B: Atomic, Molecular and Optical Physics*, 39(13):S381–S387.

[Guo et al., 1998] Guo, C., Li, M., Nibarger, J. P., and Gibson, G. N. (1998). Single and double ionization of diatomic molecules in strong laser fields. *Phys. Rev. A*, 58(6):R4271–R4274.

[Hankin et al., 2000] Hankin, S. M., Villeneuve, D. M., Corkum, P. B., and Rayner, D. M. (2000). Nonlinear ionization of organic molecules in high intensity laser fields. *Phys. Rev. Lett.*, 84(22):5082–5085.

[Hansch et al., 1996] Hansch, P., Walker, M. A., and Woerkom, L. D. V. (1996). Spatially dependent multiphoton multiple ionization. *Phys. Rev. A*, 54(4):R2559–R2562.

[Hishikawa et al., 1988] Hishikawa, A., Iwamae, A., Hoshina, K., Kono, M., and Yamanouchi, K. (1988). Coulomb explosion dynamics of n_2 in intense laser field by mass-resolved momentum imaging. *Chemical Physics*, 231(2-3):315–329.

[Iaconis and Walmsley, 1998] Iaconis, C. and Walmsley, I. A. (1998). Spectral phase interferometry for direct electric-field reconstruction of ultrashort optical pulses. *Optics Letters*, 23(10):792.

[Keitel and Knight, 1995] Keitel, C. H. and Knight, P. L. (1995). Monte carlo classical simulations of ionization and harmonic generation in the relativistic domain. *Phys. Rev. A*, 51(2):1420–1430.

[Keldysh. 1965] Keldysh, L. V. (1965). Ionization in the field of a strong electromagnetic wave. *Soviet Physics JETP*, 20(1):1307.

[Kornev et al., 2003] Kornev, A. S., Tulenko, E. B., and Zon, B. A. (2003). Kinetics of multiple ionization of rare-gas atoms in a circularly polarized laser field. *Phys. Rev. A*, 68(4):043414.

[Krause et al., 1992] Krause, J. L., Schafer, K. J., and Kulander, K. C. (1992). High-order harmonic generation from atoms and ions in the high intensity regime. *Phys. Rev. Lett.*, 68(24):3535–3538.

[Kulander et al., 1995] Kulander, K. C., Cooper, J., and Schafer, K. J. (1995). Laser-assisted inelastic rescattering during above-threshold ionization. *Phys. Rev. A*, 51(1):561–568.

[Kulander et al., 1991] Kulander, K. C., Schafer, K. J., and Krause, J. L. (1991). Single-active electron calculation of multiphoton process in krypton. *International Journal of Quantum Chemistry*, 40(S25):415–429.

[Lafon et al., 2001] Lafon, R., Chaloupka, J. L., Sheehy, B., Paul, P. M., Agostini, P., Kulander, K. C., and DiMauro, L. F. (2001). Electron energy spectra from intense laser double ionization of helium. *Phys. Rev. Lett.*, 86(13):2762–2765.

[Lee et al., 2006] Lee, K. F., Legare, F., Villeneuve, D. M., and Corkum, P. B. (2006). Measured field-free alignment of deuterium by few-cycle pulses. *Journal of Physics B: Atomic, Molecular and Optical Physics*, 39(20):4081–4086.

[Lee et al., 2004] Lee, K. F., Villeneuve, D. M., Corkum, P. B., and Shapiro, E. A. (2004). Phase control of rotational wave packets and quantum information. *Physical Review Letters*, 93(23):233601.

[Lewenstein et al., 1994] Lewenstein, M., Balcou, P., Ivanov, M. Y., L'Huillier, A., and Corkum, P. B. (1994). Theory of high-harmonic generation by low-frequency laser fields. *Phys. Rev. A*, 49(3):2117–2132.

[l'Huillier et al., 1983] l'Huillier, A., Lompre, L. A., Mainfray, G., and Manus, C. (1983). Multiply charged ions induced by multiphoton absorption in rare gases at 0.53 μm. *Phys. Rev. A*, 27(5):2503–2512.

[Litvinyuk et al., 2005] Litvinyuk, I. V., Legare, F., Dooley, P. W., Villeneuve, D. M., Corkum, P. B., Zanghellini, J., Pegarkov, A., Fabian, C., and Brabec, T. (2005). Shakeup excitation during optical tunnel ionization. *Physical Review Letters*, 94(3):033003.

[Loch et al., 2002] Loch, S. D., Pindzola, M. S., Ballance, C. P., Griffin, D. C., Mitnik, D. M., Badnell, N. R., O'Mullane, M. G., Summers, H. P., and Whiteford, A. D.

(2002). Electron-impact ionization of all ionization stages of krypton. *Phys. Rev. A*, 66(5):052708.

[Lompre et al., 1985] Lompre, L. A., L'Huillier, A., Mainfray, G., and Manus, C. (1985). Laser-intensity effects in the energy distributions of electrons produced in multiphoton ionization of rare gases. *J. Opt. Soc. Am. B*, 1(2):1906.

[Lompre et al., 1977] Lompre, L. A., Mainfray, G., Manus, C., and Thebault, J. (1977). Multiphoton ionization of rare gases by a tunable-wavelength 30-psec laser pulse at 1.06μm. *Phys. Rev. A*, 15(4):1604–1612.

[Mairesse et al., 2003] Mairesse, Y., de A Bohan, Frasinski, L. J., Merdji, H., Dinu, L. C., Monchicourt, P., Breger, P., Kovacev, M., Taieb, R., Carre, B., Muller, H. G., Agostini, P., and Salieres, P. (2003). Attosecond synchronization of high-harmonic soft x-rays. *Science*, 302(5650):1540–1543.

[Man et al., 1987] Man, K. F., Smith, A. C. H., and Harrison, M. F. A. (1987). A measurement of the cross section for electron impact ionisation of ne+, ar+, kr+ and xe+. *Journal of Physics B: Atomic and Molecular Physics*, 20(21):5865–5880.

[McPherson et al., 1987] McPherson, A., Gibson, G., Jara, H., Johann, U., Luk, T. S., McIntyre, I. A., Boyer, K., and Rhodes, C. K. (1987). Studies of multiphoton production of vacuum-ultraviolet radiation in the rare gases. *J. Opt. Soc. Am. B*, 1(4):595–601.

[Moshammer et al., 2000] Moshammer, R., Feuerstein, B., Schmitt, W., Dorn, A., Schroter, C. D., Ullrich, J., Rottke, H., Trump, C., Wittmann, M.. Korn, G., Hoffmann, K., and Sandner, W. (2000). Momentum distributions of ne^{n+} ions created by an intense ultrashort laser pulse. *Phys. Rev. Lett.*, 84(3):447–450.

[Niikura et al., 2003] Niikura, H., Corkum, P. B., and Villeneuve, D. M. (2003). Controlling vibrational wave packet motion with intense modulated laser fields. *Phys. Rev. Lett.*, 90(20):203601.

[Niikura et al., 2006] Niikura, H., Villeneuve, D. M., and Corkum, P. B. (2006). Controlling vibrational wave packets with intense, few-cycle laser pulses. *Physical Review A (Atomic, Molecular, and Optical Physics)*, 73(2):021402.

[O'Shea et al., 2001] O'Shea, P., Kimmel, M., Gu, X., and Trebino, R. (2001). Highly simplified device for ultrashort-pulse measurement. *Optics Letters*, 26(12):932.

[Pavicic et al., 2005] Pavicic, D., Kiess, A., Hansch, T. W., and Figger, H. (2005). Intense-laser-field ionization of the hydrogen molecular ions h_2^+ and d_2^+ at critical internuclear distances. *Physical Review Letters*, 94(16):163002.

[Peng et al., 2003] Peng, L.-Y., Dundas, D., McCann, J. F., Taylor, K. T., and Williams, I. D. (2003). Dynamic tunnelling ionization of h_2^+ in intense fields. *At. Mol. Opt. Phys.*, 36:L295.

[Perelomov et al., 1966] Perelomov, A. M., Popov, V. S., and Terentev, M. V. (1966). Ionization of atoms in an alternating electric field. *Soviet Physics JETP*, 23(5):924.

[Pfeifer et al., 2006] Pfeifer, T., Spielmann, C., and Gerber, G. (2006). Femtosecond x-ray science. *Reports on Progress in Physics*, 69(2):443–505.

[Plummer and McCann, 1997] Plummer, M. and McCann, J. F. (1997). Field-ionization rates of the hydrogen molecular ion. *Journal of Physics B Atomic Molecular Physics*, 30:L401.

[Posthumus, 2001] Posthumus, J. (2001). *Molecules and clusters in intense laser fields*. Cambridge University Press, Cambridge, UK.

[Posthumus et al., 1996] Posthumus, J. H., Giles, A. J., Thompson, M. R., and Codling, K. (1996). Field-ionization, coulomb explosion of diatomic molecules in intense laser fields. *Journal of Physics B Atomic Molecular Physics*, 29:5811–5829.

[Posthumus et al., 2000] Posthumus, J. H., Plumridge, J., Frasinski, L. J., Codling, K., Divall, E. J., Langley, A. J., and Taday, P. F. (2000). Slow protons as a signature of zero-photon dissociation of h_2^+ in intense laser fields. *Journal of Physics B: Atomic, Molecular and Optical Physics*, 33(16):L563–L569.

[Protopapas et al., 1996] Protopapas, M., Keitel, C. H., and Knight, P. L. (1996). Relativistic mass shift effects in adiabatic intense laser field stabilization of atoms. *Journal of Physics B: Atomic, Molecular and Optical Physics*, 29(16):L591–L598.

[Protopapas et al., 1997] Protopapas, M., Keitel, C. H., and Knight, P. L. (1997). Atomic physics with super-high intensity lasers. *Reports on Progress in Physics*, 60(4):389–486.

[Reader, 1969] Reader, J. (1969). Optimizing czerny-tnrner spectrographs: A comparison between analytic theory and ray tracing. *J. Opt. Soc. Am.*, 59(9):1189.

[Robinson et al., 2006] Robinson, J. S., Haworth, C. A., Teng, H., Smith, R. A., Marangos, J. P., and Tisch, J. W. G. (2006). The generation of intense, transform-limited laser pulses with tunable duration from 6 to 30 fs in a differentially pumped hollow fibre. *Appl. Phys. B*, 85(1):525529.

[Rosca-Pruna et al., 2001] Rosca-Pruna, F., Springate, E., Offerhaus, H. L., Krishnamurthy, M., Farid, N., Nicole, C., and Vrakking, M. J. J. (2001). Spatial alignment of diatomic molecules in intense laser fields: I. experiemntal results. *Journal of Physics B Atomic Molecular Physics*, 34:4919.

[Sanderson et al., 1997] Sanderson, J. H., Thomas, R. V., Bryan, W. A., Newell, W. R., Taday, P. F., and Langley, A. J. (1997). Multielectron-dissociative-ionization of by intense femtosecond laser pulses. *Journal of Physics B: Atomic, Molecular and Optical Physics*, 30(20):4499–4507.

[Schafer et al., 1993] Schafer, K. J., Yang, B., DiMauro, L. F., and Kulander, K. C. (1993). Above threshold ionization beyond the high harmonic cutoff. *Phys. Rev. Lett.*, 70(11):1599–1602.

[Schmidt et al., 1994] Schmidt, M., Normand, D., and Cornaggia, C. (1994). Laser-induced trapping of chlorine molecules with pico- and femtosecond pulses. *Phys. Rev. A*, 50(6):5037–5045.

[Scrinzi et al., 1999] Scrinzi, A., Geissler, M., and Brabec, T. (1999). Ionization above the coulomb barrier. *Phys. Rev. Lett.*, 83(4):706–709.

[Seideman, 1995] Seideman, T. (1995). Rotational excitation and molecular alignment in intense laser fields. *The Journal of Chemical Physics*, 103(18):7887–7896.

[Seideman, 1999] Seideman, T. (1999). Revival structure of aligned rotational wave packets. *Phys. Rev. Lett.*, 83(24):4971–4974.

[Sharp, 1970] Sharp, T. E. (1970). Potential-energy curves for molecular hydrogen and its ions. *Atomic Data and Nuclear Data Tables*, 2:119–169.

[Sheehy et al., 1998] Sheehy, B., Lafon, R., Widmer, M., Walker, B., DiMauro, L. F., Agostini, P. A., and Kulander, K. C. (1998). Single- and multiple-electron dynamics in the strong-field tunneling limit. *Phys. Rev. A*, 58(5):3942–3952.

[Siegman, 1986] Siegman, A. (1986). *Lasers*. Oxford University Press, Mill Valley, UK.

[Sola et al., 2006] Sola, I. J., Mevel, E., Elouga, L., Constant, E., Strelkov, V., Poletto, L., Villoresi, P., Benedetti, E., Caumes, J. P., Stagira, S., Vozzi, C., Sansone, G., and Nisoli, M. (2006). Controlling attosecond electron dynamics by phase-stabilized polarization gating. *Nature Physics*, 2(5):319–322.

[Spence et al., 1991] Spence, D. E., Kean, P. N., and Sibbett, W. (1991). 60-fsec pulse generation from a self-mode-locked ti:sapphire laser. *Optics Letters*, 16(1):42.

[Stolen and Lin, 1978] Stolen, R. H. and Lin, C. (1978). Self-phase-modulation in silica optical fibers. *Phys. Rev. A*, 17(4):1448–1453.

[Strickland and Mourou, 1985] Strickland, D. and Mourou, G. (1985). Compression of amplified chirped optical pulses. *Optics Communications*, 56:219.

[Takeda et al., 1982] Takeda, M., Ina, H., and Kobayashi, S. (1982). Fourier-transform method of fringe-pattern analysis for computer-based topography and interferometry. *J. Opt. Soc. Am.*, 72(1):156.

[Thompson et al., 1997] Thompson, M. R., Thomas, M. K., Taday, P. F., Posthumus, J. H., Langley, A. J., Frasinski, L. J., and Codling, K. (1997). One and two-colour studies of the dissociative ionization and coulomb explosion of h_2 with intense ti:sapphire laser pulses. *Journal of Physics B Atomic Molecular Physics*, 30:5755–5772.

[Tisch et al., 2005] Tisch, J., Robinson, J., Haworth, C., and Gregory, A. (2005). *Hollow Fibre Pulse Compression System: User's Guide*. Blackett Laboratory, Imperial College, London UK.

[Tong and Lin, 2004] Tong, X. M. and Lin, C. D. (2004). Time-resolved sequential double ionization of d[sub 2] molecules in an intense few-cycle laser pulse. *Physical Review A (Atomic, Molecular, and Optical Physics)*, 70(2):023406.

[Torres et al., 2005] Torres, R., de Nalda, R., and Marangos, J. P. (2005). Dynamics of laser-induced molecular alignment in the impulsive and adiabatic regimes: A direct comparison. *Physical Review A (Atomic, Molecular, and Optical Physics)*, 72(2):023420.

[Tournois, 1997] Tournois, P. (1997). Acousto-optic programmable dispersive filter for adaptive compensation of group delay time dispersion in laser systems. *Optics Communications*, 140(4-6):245–249.

[Trebino and Kane, 1993] Trebino, R. and Kane, D. J. (1993). Using phase retrieval to measure the intensity and phase of ultrashort pulses: frequency-resolved optical gating. *J. Opt. Soc. Am.*, 10(5):1101.

[Ullrich et al., 2003] Ullrich, J., Moshammer, R., Dorn, A., Dorner, R., Schmidt, L. P. H., and Schmidt-Bocking, H. (2003). Recoil-ion and electron momentum spectroscopy: reaction-microscopes. *Reports on Progress in Physics*, 66(9):1463–1545.

[van der Hart and Burnett, 2000] van der Hart, H. W. and Burnett, K. (2000). Recollision model for double ionization of atoms in strong laser fields. *Phys. Rev. A*, 62(1):013407.

[Verluise et al., 2000] Verluise, F., Laude, V., Cheng, Z., Spielmann, C., and Tournois, P. (2000). Amplitude and phase control of ultrashort pulses by use of an acousto-optic programmable dispersive filter: pulse compression and shaping. *Optics Letters*, 25(8):575.

[Volkov, 1935] Volkov, D. M. (1935). Uber eine klasse von losungen der diracschen gleichung. *Z. Phys.*, 1(94):250.

[Vrakking et al., 1996] Vrakking, M. J. J., Villeneuve, D. M., and Stolow, A. (1996). Observation of fractional revivals of a molecular wave packet. *Phys. Rev. A*, 54(1):R37–R40.

[Walker et al., 1994] Walker, B., Sheehy, B., DiMauro, L. F., Agostini, P., Schafer, K. J., and Kulander, K. C. (1994). Precision measurement of strong field double ionization of helium. *Phys. Rev. Lett.*, 73(9):1227–1230.

[Walker et al., 1998] Walker, M. A., Hansch, P., and Woerkom, L. D. V. (1998). Intensity-resolved multiphoton ionization: Circumventing spatial averaging. *Phys. Rev. A*, 57(2):R701–R704.

[Weber et al., 2000] Weber, T., Giessen, H., Weckenbrock, M., Staudte, A., Spielberger, L., Jagutzki, O., Mergel, V., Urbasch, G., Vollmer, M., and Doerner, R. (2000). Correlated electron emission in multiphoton double ionization. *Nature*, 1(404):608.

[Weckenbrock et al., 2004] Weckenbrock, M., Zeidler, D., Staudte, A., Weber, T., Schoffler, M., Meckel, M., Kammer, S., Smolarski, M., Jagutzki, O., Bhardwaj, V. R., Rayner, D. M., Villeneuve, D. M., Corkum, P. B., and Dorner, R. (2004). Fully differential rates for femtosecond multiphoton double ionization of neon. *Physical Review Letters*, 92(21):213002.

[Wiley and McLaren, 1955] Wiley, W. C. and McLaren, I. H. (1955). Time-of-flight mass spectrometer with improved resolution. *Review of Scientific Instruments*, 26(12):1150–1157.

[Yergeau et al., 1986] Yergeau, F., Petite, G., and Agostini, P. (1986). Above-threshold ionisation without space charge. *Journal of Physics B: Atomic and Molecular Physics*, 1(19):1699.

[Yudin and Ivanov, 2001] Yudin, G. L. and Ivanov, M. (2001). Physics of correlated double ionization of atoms in intense laser fields: Quasistatic tunneling limit. *Phys. Rev. A*, 63(3):033404.

[Zewail, 2000] Zewail, A. H. (2000). Femtochemistry: Atomic-scale dynamics of the chemical bond. *Journal of Physical Chemistry A*, 104(24):5660–5694.

[Zon, 1999] Zon, B. A. (1999). Many-electron tunneling in atoms. *Journal of Experimental and Theoretical Physics*, 89(2):219.

[Zuo and Bandrauk, 1995] Zuo, T. and Bandrauk, A. D. (1995). Charge-resonance-enhanced ionization of diatomic molecular ions by intense lasers. *Phys. Rev. A*, 52(4):R2511–R2514.